Utfärdare/Issued by
Andreas Persson

Telefon/Phone
+46705142998

Dokumentslag/Type of document
Report

Reg-nr/Reg. No.
Creo-R-12-003

Godkänd/Approved by

Datum/Date
2012-03-13

Infoklass/Info. class
Company unclassified

Utgåva/Issue
1

Sida/Page
1(84)

Projekt nr/Project no

Arkiveringsdata/File
Master_thesis_AP_FINAL

Fördelning/To

Ärende/Subject
Master Thesis

Detached-Eddy Simulations of Active Flow Control Systems on a Simplified Car Geometry

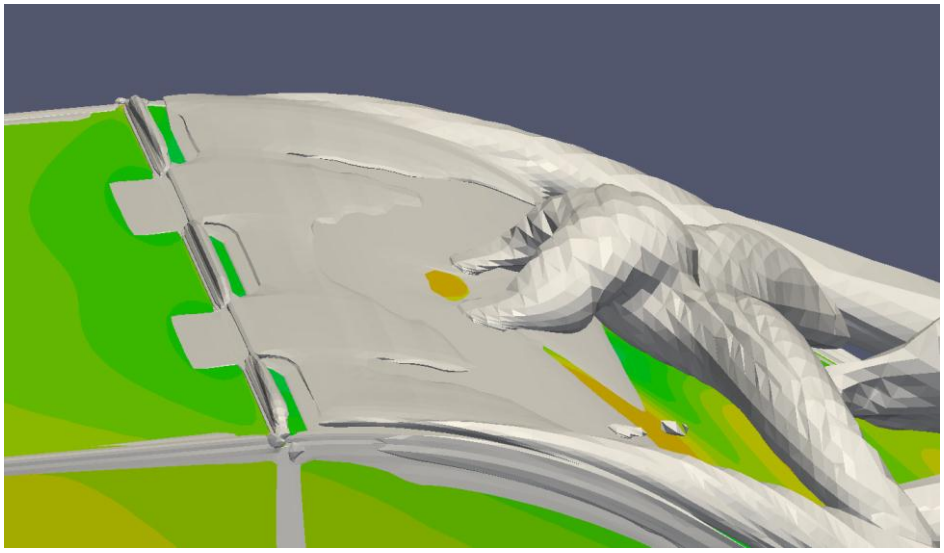

Issued by: Andreas Persson

Approved by:

Reviewed by:

Reviewed by:

Reviewed by:

ABSTRACT

The feasibility of implementing an active flow control system in ground vehicles is investigated through detached-eddy simulations of the Windsor model. This is done in the open-source CFD code OpenFOAM. Forcing is done with a zero-net-mass-flux actuator, which is modeled as a sinusoidal velocity boundary condition through slots located at the rear edge of the roof. Simulations are done in three steps: 2D, semi-3D and 3D, to give an understanding of different flow phenomena, and a parameter study is performed. Results show that drag can be reduced mainly by reducing the strength of the vortex shedding process, with a gradual decrease in effectiveness from 2D to 3D. A small drag reduction is achieved in semi-3D, and a lift reduction is achieved in 3D. DES methodology is shown to work well when simulating active flow control.

NOMENCLATURE

Symbols

μ	Dynamic viscosity	[kg/(ms)]
ν	Kinematic viscosity	[m^2/s]
ρ	Air density	[kg/m^3]
ω	Vorticity	[1/s]
A	Frontal area	[m^2]
C_μ	Momentum coefficient	[-]
C_D	Drag coefficient	[-]
C_L	Lift coefficient	[-]
g	Gravitational acceleration	[m/s^2]
L	Vehicle length	[m]
m	Mass	[kg]
P	Power	[W]
p	Pressure	[Pa]
t	Time	[s]
t^*	Non-dimensional time	[-]
U_∞	Freestream velocity	[m/s]
V	Velocity magnitude	[m/s]
$\boldsymbol{V}=(u,v,w)$	Velocity vector	[m/s]
q	Dynamic pressure	[Pa]

Abbreviations

AFC	Active Flow Control
CFD	Computational Fluid Dynamics
CFL	Courant-Friedrich-Levy number
CO_2	Carbon Dioxide
DES	Detached-Eddy Simulation
DDES	Delayed Detached-Eddy Simulation
DNS	Direct Numerical Simulation
ESD	Energy Spectral Density
FFT	Fast Fourier Transform
FLC	Fuzzy Logic Control
FOAM	Field Operation And Manipulation
GAMG	Geometric-Algebraic Multi-Grid
GIS	Grid-Induced Separation
LES	Large-Eddy Simulation
MSD	Modeled Stress Depletion
PCG	Preconditioned Conjugate Gradient
PISO	Pressure Implicit with Split Operators
RANS	Reynolds-Averaged Navier-Stokes
SIMPLE	Semi-Implicit Method for Pressure-Linked Equations
SGS	Sub-grid scale

TABLE OF CONTENTS

1 INTRODUCTION

1.1 Environmental impact from ground transport

The 23 April 2009, the European Commission passed regulation 443/2009 which limits average carbon dioxide (CO_2) emissions from passenger cars to a maximum of 130 g/km – phased in from 2012 through 2015. If car manufacturers do not comply with this level, they will face severe penalties. For each vehicle sold, the first gram over the limit will be fined €5, the second gram €15, the third €25, the fourth and above will be fined with €95 each (1).

This means that a manufacturer with average CO_2 emissions of 140 g/km will have to pay a fine of €710 for each sold car – a considerable amount. So car manufacturers are racing to reduce fuel consumption (and hence CO_2 emissions) of their vehicles ahead of 2012, when the penalties will start being imposed on them.

The goal of these rather harsh measures is to reverse the trend of road transports being one of few sectors in the EU where emissions are currently rising rapidly. Today they account for about 20 % of total CO_2 emissions in the union. Passenger cars account for the biggest part: about 12 % of total emissions. As part of a long-term strategy, the EU plans to expand upon current limits by reducing average CO_2 emissions among light-duty vehicles to 95 g/km by 2020 (2).

1.2 The quest for reduced fuel consumption

1.2.1 Technical solutions

In order to quickly reduce fuel consumption, a number of measures have had to be implemented in car designs. The first one is turbocharging along with downsizing of engines, which has resulted in significantly lower emissions but with maintained power. Another important measure is hybridization, where an electric powertrain is added to the existing one. The electric motor helps the internal combustion engine (ICE) during acceleration and at low speeds, so that the ICE can be made smaller and run more efficiently.

Naturally, other aspects of vehicle design continue to be further optimized. Engineers mainly focus on reducing weight, using tires with reduced rolling resistance and improving the aerodynamic design in order to reduce drag. In fact, electric powertrains have an attribute that places further importance on aerodynamics; namely the fact that they can capture (or harvest) kinetic energy during braking and recharge the batteries – a technique called regenerative braking. This energy would have otherwise been lost as heat in the brake discs.

As a significant amount of the energy required to overcome the weight of the vehicle can now be re-captured during braking, weight becomes relatively less important for the fuel consumption. Aerodynamic drag, along with rolling resistance, however constantly drains energy from the vehicle, energy that can never be re-captured. So the current automotive fashion of hybrid and electric cars demands increased focus on vehicle aerodynamics.

1.2.2 Importance of aerodynamics in road vehicles

Figure 1 shows the components of the total resistance in a typical driving scenario on the highway or in the city (3). It is apparent that drag is easily the biggest contributor to the total required energy when driving on the highway, but contributes less when driving in cities, due to the lower speeds.

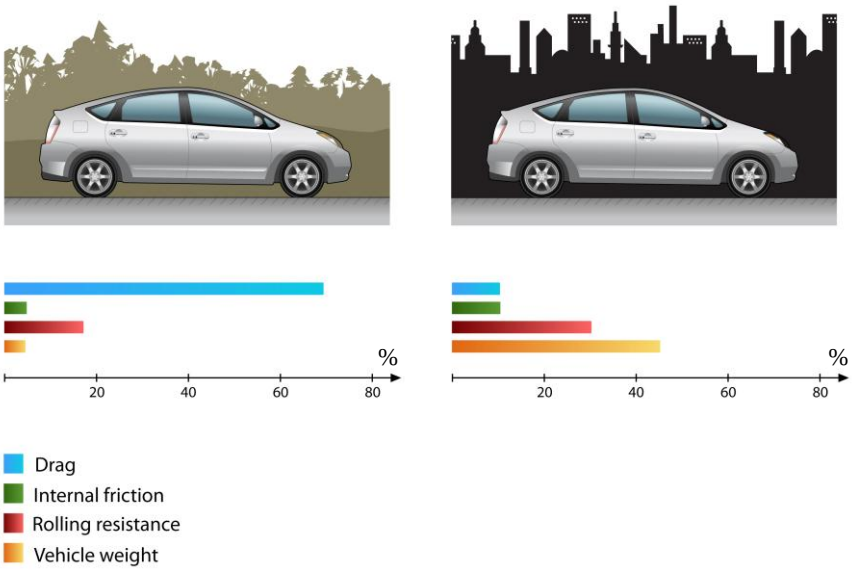

Figure 1. Relative importance of different parameters to total road resistance for highway and city driving, respectively.

To see the effects of the different resistive forces more accurately, the propulsive equation of motion is evaluated. Power required at the wheels to balance the resistive forces is given by:

$$P = (C_D q A + C_{rr} m g) V \tag{1.1}$$

$$q = \frac{1}{2} \rho V^2 \tag{1.2}$$

A typical car of the following properties is assumed:

Characteristic	Size
Mass	1500 kg
Width	1.70 m
Height	1.40 m
Frontal Area	2.02 m^2
Rolling resistance C_{rr}	0.010
Engine efficiency	0.18
Drivetrain efficiency	0.90
Energy content, petrol	35 MJ/L

Table 1. Assumed properties in aerodynamic calculations.

In **Figure 2**, it can be seen that drag is the dominating part of total vehicle resistance at speeds above approximately 70 km/h (depending on the drag coefficient). Already at a typical highway speed of 110 km/h, aerodynamic drag accounts for more than 70 % of total resistance.

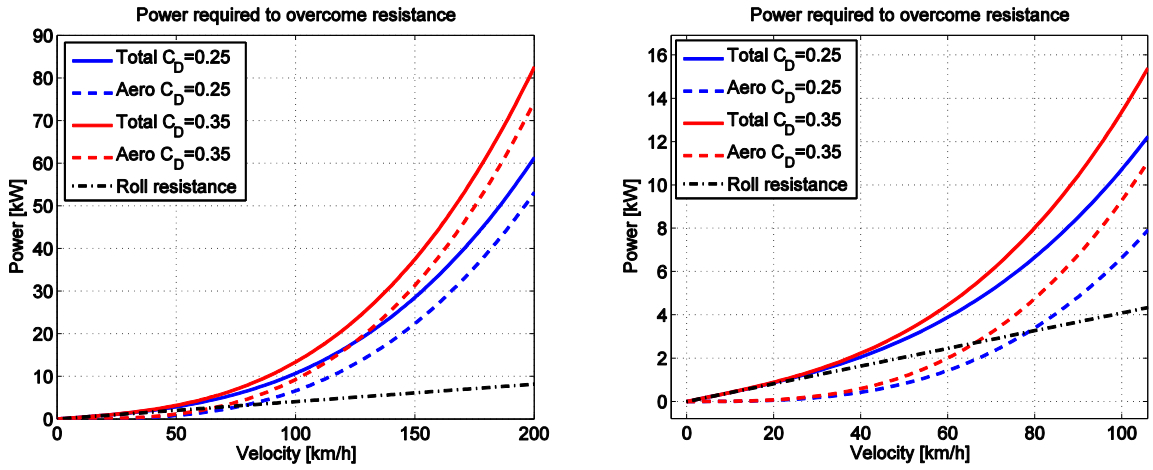

Figure 2. Power required by vehicle to overcome resistive forces, close-up on the right.

By solving equation (1.1) for different values of C_D, and integrating with respect to time, one gets the work required to travel a certain distance. By taking into account the powertrain efficiency of a typical car and the energy content of petrol, the fuel consumption can be estimated. **Figure 3** shows both the savings of driving more slowly and the gains possible if the drag coefficient is improved.

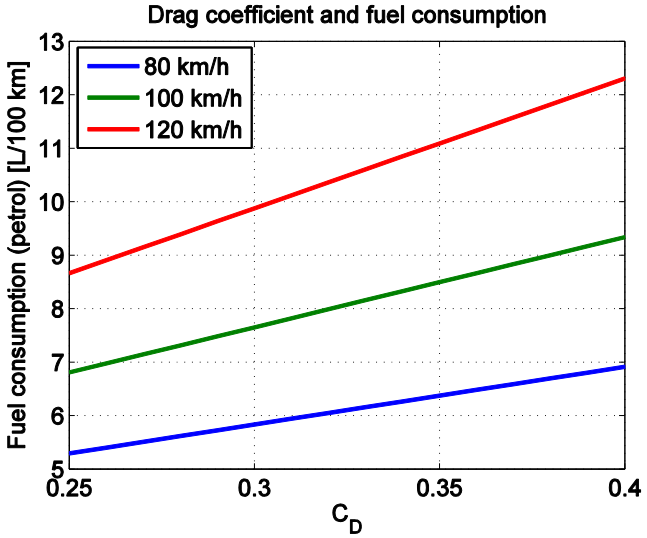

Figure 3. Influence of drag coefficient and speed on fuel consumption.

If C_D is reduced from 0.30 to 0.25, the driver will save more than 1 liter per 100 km at a steady speed of 120 km/h. This may not seem overwhelming, but considering that the average car travels around 20,000 km per year (albeit not always at highway speeds), the fuel saved will be felt both in the wallet and by the environment. Savings of 200 liters in a year results in 470 kg less CO_2 emitted – accomplished by a single car (4). A total of 13.1 million passenger cars were sold in the European Union in 2011 (5). Assuming a potential saving of 0.5 L/100 km (considering that cars do not travel around constantly at 120 km/h), a total of 3.1 million tons of CO_2 could be saved annually!

1.2.3 Active Flow Control (AFC)

Active flow control is the method of controlling airflow through some sort of active means. It can be done for example by blowing or sucking air through a slot or hole in order to achieve some desired effect, for instance to delay separation of the airflow or a breakdown of large vortices. The device used to control the airflow can vary, but the most common is either a pump or compressor used for sucking or blowing air, or an oscillating membrane to produce a periodic suction/blowing effect. The last type does not add or remove any mass from the external airflow as the net velocity through the slot is zero over a sinusoidal period. They are therefore called *zero-net-mass-flux (ZNMF) actuators* (explained more in detail in chapter 4.2).

The way AFC works is that it adds energy to the part of the boundary layer that is closest to the wall. As separation occurs when the velocity gradient normal to the wall reaches zero when faced with an adverse pressure gradient, AFC can delay the location at which this happens. Blowing systems inject air parallel to the wall so that the boundary layer closest to the wall is re-energized and can travel further before separating. Suction systems mainly work by improving the mixing of the outer parts of the boundary layer, which has more energy, with the inner parts with less energy. The effect of AFC on the boundary layer is illustrated in **Figure 4**.

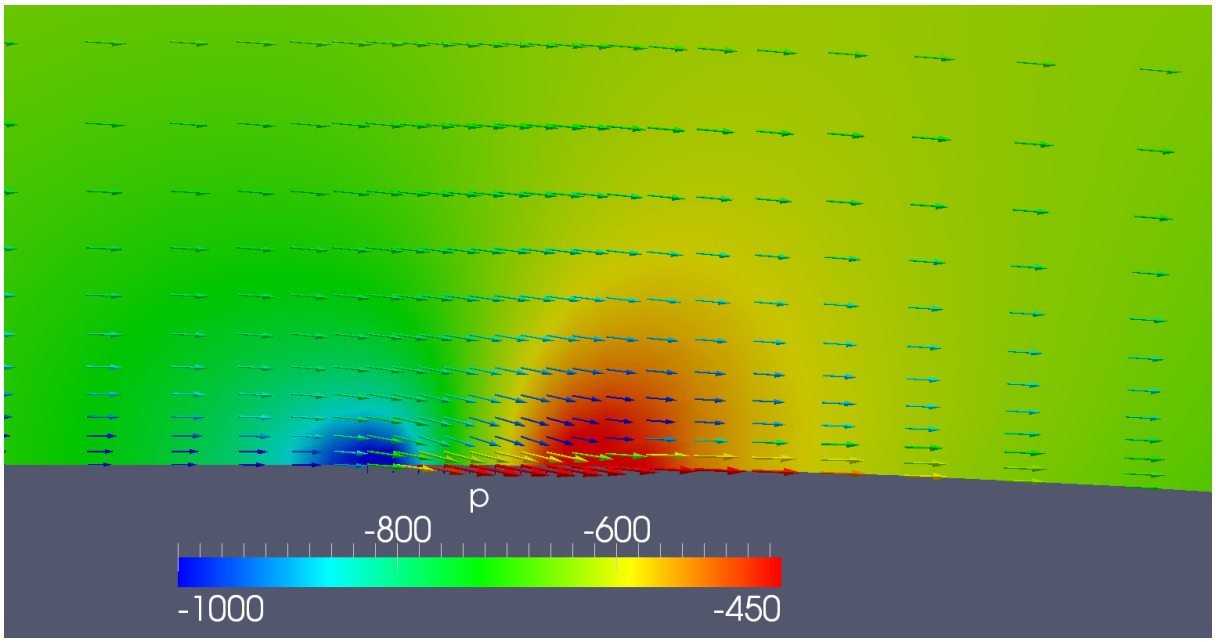

Figure 4. Boundary layer velocity vectors during suction phase of a zero-net-mass-flux actuator.

It is apparent that the actuator succeeds in increasing the energy in the boundary layer, as the velocity close to the wall is higher downstream of the actuator than upstream of it. This allows the air to travel further in the adverse pressure gradient before separating. Also, a low pressure area is produced upstream of the actuator slot, and a higher pressure area is produced just downstream of it.

1.3 Previous research on AFC

Research on active flow control has been ongoing since the 1990's. Initially, most of the research focused on its implementation within the field of aeronautics, for example Seifert and Pack (6) who demonstrated that oscillatory excitation (ZNMF actuators) could delay stall and increase maximum lift of an airfoil, as well as improve post-stall lift and drag. In transonic speeds, oscillatory excitation could reduce the strength of shock-induced buffeting. El-Alti et al. (7) showed significant improvements in lift and drag coefficients by simulating AFC in the wing of the XV-15 tilt-rotor aircraft.

Greenblatt and Wygnanski (8) identified two important variables for the performance of an active flow control system; the first being the reduced forcing frequency:

$$F^+ = \frac{fl}{U_\infty} \tag{1.3}$$

where f is the actuator frequency and l is a characteristic length. This is very similar to the Strouhal number except it is based on the forcing frequency instead of a natural shedding frequency. The other important variable is the momentum coefficient

$$C_\mu = \frac{u_{rms}^2}{U_\infty^2}\frac{h_{slot}}{h_{ref}} \tag{1.4}$$

where u_{rms}^2 is the root mean square of the slot velocity, h_{slot} is the slot width and h_{ref} is a characteristic length (such as the width, length or height of the vehicle). It describes the momentum added to the freestream by the actuators in relation to the reference momentum in the freestream. The effect of exciting the flow with the momentum coefficient C_μ is fairly constant when scaling the vehicle. In effect, to achieve a similar result when using AFC on a truck in comparison to a passenger car, more momentum must be added and subtracted by the actuators since the truck is larger. This can be done by increasing the size of the slots or by blowing/sucking with higher velocity amplitude.

Several studies, both experimental and numerical, have been performed using AFC for drag reduction of bluff bodies. Examples include simplified car geometries, such as the Ahmed body (9), and truck geometries as defined for example by El-Alti et al. (10) It was there demonstrated that by adding flaps at the trailing edge of the trailer and energizing the boundary layer with ZNMF actuators to avoid separation, drag could be reduced by up to 25 % compared to a standard truck-trailer configuration.

The actuators have in most cases been run in an open-loop ("dumb") configuration. The parameters are optimized for specific conditions, where the actuators perform well. However, disturbances and varying airflow conditions, as for example gusts and crosswinds, are not taken into account and may pose problems for open-loop control. Closed-loop feedback control has been performed successfully for simple geometries such as a cylinder or a 2D "bullet-shaped" body, for low Reynolds numbers (11), (12).

1.4 Purpose of this report

The purpose of this Master thesis is to investigate whether it is possible to model a zero-net-mass-flux actuator in the open-source CFD solver OpenFOAM, and if it is, to evaluate the possibility of reducing drag on a simplified car geometry using the technique. An effort will be made to understand the fundamental flow properties that affect the drag, and how they can be influenced in a desired manner. The magnitude and consistency of a possible drag reduction will be quantified to determine whether the savings in fuel consumption from reduced drag can offset the complexity and added cost of an active flow control system. If so, the possible commerciality of the system in the not too distant future could be shown.

Some effort will be made in trying to deduce ways of closed-loop or adaptive control of the airflow. This is the key for developing an AFC system that can cope with varying conditions, as in real life. A system that only works for a few specific conditions in a closed wind tunnel is not of much commercial use. As the control of an inherently non-linear flow field is expected to be very complex, an open-minded approach will be used – so that novel control strategies are not discarded without thought.

2 FLUID DYNAMICS MODELING

2.1 Governing equations

Fluid mechanics is governed by the Navier-Stokes equations. They consist of a nonlinear system of five partial differential equations (PDEs): one continuity equation, three momentum equations and one energy equation. These are for a compressible, Newtonian fluid (constant viscosity):

$$\frac{\partial \rho}{\partial t} + \nabla \cdot (\rho \boldsymbol{V}) = 0 \tag{2.1}$$

$$\frac{\partial \rho u}{\partial t} + u\frac{\partial \rho u}{\partial x} + v\frac{\partial \rho u}{\partial y} + w\frac{\partial \rho u}{\partial z} = -\frac{\partial p}{\partial x} + \frac{\partial}{\partial x}\left(2\mu\frac{\partial u}{\partial x} + \lambda\nabla\cdot\boldsymbol{V}\right) + \frac{\partial}{\partial y}\left(\mu\left(\frac{\partial u}{\partial y} + \frac{\partial v}{\partial x}\right)\right) + \frac{\partial}{\partial z}\left(\mu\left(\frac{\partial u}{\partial z} + \frac{\partial w}{\partial x}\right)\right) + \rho g_x \tag{2.2}$$

$$\frac{\partial \rho v}{\partial t} + u\frac{\partial \rho v}{\partial x} + v\frac{\partial \rho v}{\partial y} + w\frac{\partial \rho v}{\partial z} = -\frac{\partial p}{\partial y} + \frac{\partial}{\partial x}\left(\mu\left(\frac{\partial v}{\partial x} + \frac{\partial u}{\partial y}\right)\right) + \frac{\partial}{\partial y}\left(2\mu\frac{\partial v}{\partial y} + \lambda\nabla\cdot\boldsymbol{V}\right) + \frac{\partial}{\partial z}\left(\mu\left(\frac{\partial v}{\partial z} + \frac{\partial w}{\partial y}\right)\right) + \rho g_y \tag{2.3}$$

$$\frac{\partial \rho w}{\partial t} + u\frac{\partial \rho w}{\partial x} + v\frac{\partial \rho w}{\partial y} + w\frac{\partial \rho w}{\partial z} = -\frac{\partial p}{\partial z} + \frac{\partial}{\partial x}\left(\mu\left(\frac{\partial w}{\partial x} + \frac{\partial u}{\partial z}\right)\right) + \frac{\partial}{\partial y}\left(\mu\left(\frac{\partial w}{\partial y} + \frac{\partial v}{\partial z}\right)\right) + \frac{\partial}{\partial z}\left(2\mu\frac{\partial w}{\partial z} + \lambda\nabla\cdot\boldsymbol{V}\right) + \rho g_z \tag{2.4}$$

$$\frac{\partial}{\partial t}\left(\rho\left(e + \frac{V^2}{2}\right)\right) + \nabla\cdot\left(\rho\left(e + \frac{V^2}{2}\right)\boldsymbol{V}\right) = \rho\frac{dq}{dt} + \frac{\partial}{\partial x}\left(k\frac{\partial T}{\partial x}\right) + \frac{\partial}{\partial y}\left(k\frac{\partial T}{\partial y}\right) + \frac{\partial}{\partial z}\left(k\frac{\partial T}{\partial z}\right) + \boldsymbol{\Phi} \tag{2.5}$$

where $\lambda = \frac{2}{3}\mu$, e is the internal energy of the fluid, q is the heat being added to the flow, T is the temperature, k is the thermal conductivity of the fluid and Φ is a collection of additional dissipative terms that perform work on the fluid due to for example friction.

There are six unknowns in the Navier-Stokes equations: *u, v, w, p, ρ, T.* The sixth equation needed for closure of the system of equations is the ideal gas law:

$$p = \rho RT \tag{2.6}$$

where *R* is the specific gas constant of the fluid.

2.2 Simplifications

Air can be considered incompressible below *M=0.3*, which is the case for standard vehicle aerodynamics. So density is assumed constant throughout the computational domain. It is also assumed that there are no external body forces that affect the solution. Friction in the boundary layer does not generate any noticeable heat that needs to be accounted for in the solution. Finally the ambient temperature is assumed constant.

Consequently, the Navier-Stokes equations can be reduced to:

$$\nabla \cdot \boldsymbol{V} = 0 \tag{2.7}$$

$$\frac{\partial u}{\partial t} + u\frac{\partial u}{\partial x} + v\frac{\partial u}{\partial y} + w\frac{\partial u}{\partial z} = -\frac{1}{\rho}\frac{\partial p}{\partial x} + \frac{\partial}{\partial x}\left(2\nu\frac{\partial u}{\partial x} + \lambda\nabla\cdot\boldsymbol{V}\right) + \frac{\partial}{\partial y}\left(\nu\left(\frac{\partial u}{\partial y} + \frac{\partial v}{\partial x}\right)\right) + \frac{\partial}{\partial z}\left(\nu\left(\frac{\partial u}{\partial z} + \frac{\partial w}{\partial x}\right)\right) \tag{2.8}$$

$$\frac{\partial v}{\partial t} + u\frac{\partial v}{\partial x} + v\frac{\partial v}{\partial y} + w\frac{\partial v}{\partial z} = -\frac{1}{\rho}\frac{\partial p}{\partial y} + \frac{\partial}{\partial x}\left(\nu\left(\frac{\partial v}{\partial x} + \frac{\partial u}{\partial y}\right)\right) + \frac{\partial}{\partial y}\left(2\nu\frac{\partial v}{\partial y} + \lambda\nabla\cdot\boldsymbol{V}\right) + \frac{\partial}{\partial z}\left(\nu\left(\frac{\partial v}{\partial z} + \frac{\partial w}{\partial y}\right)\right) \tag{2.9}$$

$$\frac{\partial w}{\partial t} + u\frac{\partial w}{\partial x} + v\frac{\partial w}{\partial y} + w\frac{\partial w}{\partial z} = -\frac{1}{\rho}\frac{\partial p}{\partial z} + \frac{\partial}{\partial x}\left(\nu\left(\frac{\partial w}{\partial x} + \frac{\partial u}{\partial z}\right)\right) + \frac{\partial}{\partial y}\left(\nu\left(\frac{\partial w}{\partial y} + \frac{\partial v}{\partial z}\right)\right) + \frac{\partial}{\partial z}\left(2\nu\frac{\partial w}{\partial z} + \lambda\nabla\cdot\boldsymbol{V}\right) \tag{2.10}$$

Equations (2.7) - (2.10) are the incompressible Navier-Stokes equations without external forces or heat transfer. The energy equation (2.5) is entirely omitted. The unknown variables are the velocity components *u, v, w* and the pressure *p*. There are a few different ways of solving these equations, all of which involve an iterative procedure. The way this is done by the CFD solver is explained in chapter 3.3.

2.3 Boundary layer

2.3.1 Definitions

The region closest to the wall is defined by the boundary layer. It is characterized by a velocity deficiency compared to the freestream velocity. The boundary layer thickness is defined as the distance from the wall to the point where the local velocity is 99 % of the freestream velocity.

The non-dimensional wall distance y^+ is now introduced, defined as

$$y^+ = \frac{u_* y}{\nu} \tag{2.11}$$

$$u_* = \sqrt{\frac{\tau_w}{\rho}} \tag{2.12}$$

where u_* is called the friction velocity which is dependent on the wall shear stress $\tau_{w,}$ while y is the distance from the wall. The dimensionless velocity u^+ is then defined as

$$u^+ = \frac{u}{u_*} \tag{2.13}$$

A typical average velocity profile close to the wall in a turbulent flow is shown in **Figure 5**. There are two distinct parts of the boundary layer: the viscous sublayer and the log-law region. The buffer layer is the transition layer between the two.

2.3.2 Wall functions

Because the velocity gradient in the viscous sublayer close to the wall is large, there must be many discretized cells in this area to properly capture the dynamics of the flow (i.e. to resolve the boundary layer). This can be very costly, especially at high velocities and Reynolds numbers. An alternative to resolving the boundary layer is to use *wall functions.* These use an empirical formula to describe the velocity profile between the wall and the cell closest to it. This is possible because most turbulent boundary layers behave similarly, so if the y^+-value of the closest cell is known, empirical knowledge can then be employed to estimate the part of the boundary layer that is unresolved.

Of course, since the velocity profile is not calculated when using wall functions, they are approximations that may be poor in some cases, such as boundary layers in an adverse pressure gradient, swirling flows and so on. Another challenge is that many wall functions place strict demands on the first cell being in the log-law region to work properly – which may be difficult to realize in all parts of the domain.

Wall functions that can handle y^+ values in the buffer layer or viscous sublayer are called *continuous* or *adaptive* wall functions. However, it is generally recommended to place the first grid cell in the log-law region when using any wall function, preferably close to $y^+ = 30$.

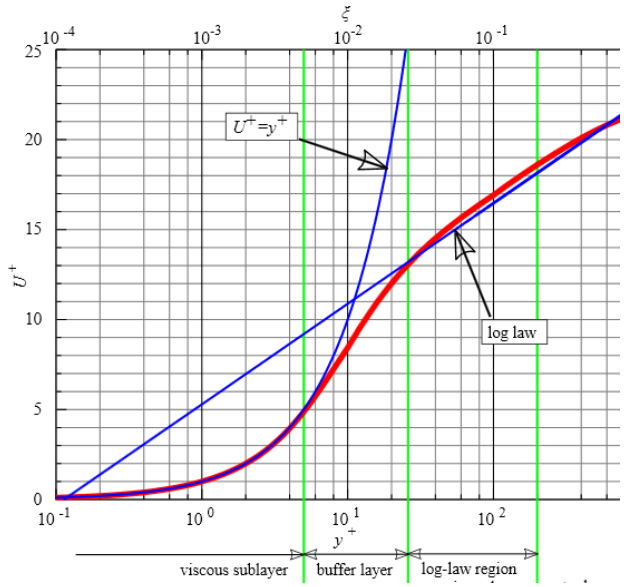

Figure 5. Typical velocity profile (red) close to the wall of an object. The blue curves represent different laws which approximate the velocity in different parts of the boundary layer (13).

2.4 Turbulence modeling

At comparatively high Reynolds numbers (as experienced in full-size vehicle aerodynamics) the flow field is predominantly turbulent. The turbulent structures – *eddies* – are of many different orders of magnitude in size, where the largest ones carry the most energy and influence the solution the most.

All the turbulent structures can be directly solved using the Navier-Stokes equations, but this comes at an extreme computational cost due to the need for sufficient spatial and temporal resolution. As a result, the computational mesh needs to be extremely fine to be able to resolve even the smallest eddies. Therefore, the technique of *Direct Numerical Simulation* (DNS) is rarely used today for practical engineering purposes. Favre estimated that computational resources for use of DNS in real-world problems would be available around the year 2080 (14).

Since it is not feasible to make use of DNS in the foreseeable future, the equations have to be simplified somehow. This is done by approximating the turbulent motions (modeling the turbulence). The main ways of accomplishing this is by using Large-Eddy Simulation, Reynolds-Averaged Navier-Stokes equations, or hybrid methods – all of which will be briefly explained.

2.4.1 Large-Eddy Simulation (LES)

If it is the case that the smaller eddies in turbulent flow contain less energy than the larger ones, one could get away with not calculating these directly, but instead approximate their influence with a model. This is done by applying an LES filter to separate the large, low frequency, eddies from the small, high frequency, ones. A statistical model, called a *subgrid-scale (SGS) model*, is then applied to model the small eddies. The large eddies are resolved, i.e. calculated directly from the Navier-Stokes equations.

The application of LES assumes the following: (15)

- The large scales of the flow contribute to its main physics, such as transition to turbulence and production of the turbulent kinetic energy.
- The large scales are dependent on the boundary conditions and are anisotropic.
- The large scales contain at least 80 – 90 % of the turbulent kinetic energy.
- The small scales are isotropic and only responsible for viscous dissipation of energy.
- The small scales only contain a small amount of the total kinetic energy.

When the LES filter has been applied, the kinematic viscosity ν in equations (2.8) - (2.10) is split into two parts: $\nu = \nu_{resolved} + \nu_{SGS}$, where ν_{sgs} is the subgrid-scale eddy viscosity. Several different LES models have been developed, the most well-known being the *Smagorinsky-Lilly* model, which was also the first to be developed. They all share the purpose of estimating the behavior of the SGS eddies so as to obtain values for ν_{sgs}. When using filtered N-S equations the need to resolve all the scales of the eddies is eliminated, so a speedup is achieved in comparison with DNS.

The ratio of resolved to modeled eddies is determined by the mesh resolution. Only eddies that are larger than the mesh cells are captured. The rest are modeled with the SGS model (**Figure 6**). So a finer mesh will be able to resolve more eddies, thus resulting in a more accurate solution – at the cost of more demanding computational resources.

The boundary layer friction contributes directly to the forces on the body, but also affects the separation point that can have a major influence on the drag. For an LES model to correctly predict the friction the boundary layer must be adequately resolved. To achieve this, the first grid cell above the wall should have a y^+ of about 1. For an accurate LES, the grid cells should also be as close to cubic as possible throughout the entire mesh. This coupled with the resolution requirement in the wall-normal direction forces the mesh to be very fine also in the streamwise direction. This is the main reason for the extremely large meshes and small time steps required for full LES calculations, which make them infeasible for high-Reynolds number problems in the immediate future (15).

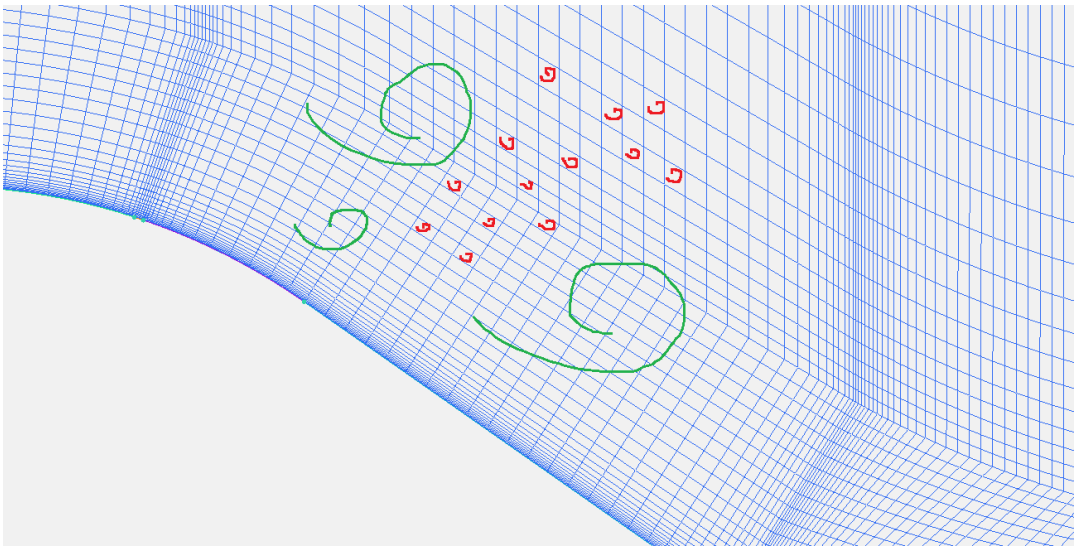

Figure 6. Only eddies that are larger than the cells are resolved (green). The rest are captured in the SGS model (red).

2.4.2 Reynolds-Averaged Navier-Stokes (RANS)

In contrast to LES where the instantaneous movement of the larger turbulent eddies is calculated, RANS models do not give any instantaneous information about the turbulent behavior. Instead they simplify the problem by only considering the time-averaged influence of turbulence on the mean flow. For most engineering purposes, it is sufficient to have information about mean stresses, velocities and pressures to be able to analyze the performance of different geometries for example. So it makes sense to simplify the problem, as the computational costs are much lower than for LES (16).

This is done by modifying the Navier-Stokes momentum equations so that they describe the time-averaged flow instead of the instantaneous one. This gives rise to six extra variables called the *Reynolds stresses*. The increase in cost from introducing extra, unknown variables is easily outweighed by the reduced complexity of solving the time-averaged momentum equations. The job of the different RANS models is to predict these six new unknowns, and consequently also the eddy viscosity. This is done differently depending on which turbulence model is used (16).

The most commonly used and validated turbulence model is the *k-ε* model, which introduces two new PDEs for solving the turbulent kinetic energy *k* and the turbulent energy dissipation rate *ε*. The eddy viscosity is then defined as:

$$\nu_t = \frac{C_\mu k^2}{\epsilon} \tag{2.14}$$

where C_μ is a constant obtained through empirical testing of various flow cases. It is usually set to the value 0.09.

In this thesis however, the preferred turbulence model is the *Spalart-Allmaras (S-A)* model (17), for the following main reasons:

- Simple model with only one introduced equation,
- Proven to work well in many different situations, (18)
- Synergies possible with similar work done by Favre, (14)
- S-A is the standard RANS model to use with DES (to be explained later).

The S-A turbulence model introduces a modified viscosity variable $\tilde{\nu}$. It is solved via the introduced PDE:

$$\frac{\partial \tilde{\nu}}{\partial t} + u_j \frac{\partial \tilde{\nu}}{\partial x_j} = C_{b1}(1 - f_{t2})\tilde{S}\tilde{\nu} + \frac{1}{\sigma}\{\nabla \cdot [(\nu + \tilde{\nu})\Delta\tilde{\nu}] + C_{b2}|\Delta\nu|^2\} - \left(C_{w1}f_w - \frac{C_{b1}}{\kappa^2}f_{t2}\right)\left(\frac{\tilde{\nu}}{d}\right)^2 + f_{t1}\Delta V^2$$

$$\begin{aligned} f_{t2} &= C_{t3}\exp(-C_{t4}\chi^2) \\ \chi &= \frac{\tilde{\nu}}{\nu} \\ \tilde{S} &= S + \frac{\tilde{\nu}}{\kappa^2 d^2} f_{v2} \\ f_{v2} &= 1 - \frac{\chi}{1 + \chi f_{v1}} \\ f_w &= g\left(\frac{1 + C_{w3}^6}{g^6 + C_{w3}^6}\right)^{1/6} \\ g &= r + C_{w2}(r^6 - r) \\ r &= \frac{\tilde{\nu}}{\tilde{S}\kappa^2 d^2} \\ f_{t1} &= C_{t1} g_t \exp\left(-C_{t2}\frac{\omega_t^2}{\Delta V^2}(d^2 + g_t^2 d_t^2)\right) \end{aligned} \qquad (2.15)$$

where d is the distance from the wall to the grid cell. When the modified viscosity $\tilde{\nu}$ has been solved, the eddy viscosity ν_t is calculated as:

$$\begin{aligned} \nu_t &= \tilde{\nu} f_{v1} \\ f_{v1} &= \frac{\chi^3}{\chi^3 + C_{v1}^3} \end{aligned} \qquad (2.16)$$

The constants of the S-A PDE are:

Constant	Value
σ	2/3
κ	0.41
$\mathbf{C_{b1}}$	0.1355
$\mathbf{C_{b2}}$	0.622
$\mathbf{C_{w1}}$	$C_{b1}/\kappa^2 + (1 + C_{b2})/\sigma$
$\mathbf{C_{w2}}$	0.3
$\mathbf{C_{w3}}$	2
$\mathbf{C_{v1}}$	7.1
$\mathbf{C_{t1}}$	1
$\mathbf{C_{t2}}$	2
$\mathbf{C_{t3}}$	1.1
$\mathbf{C_{t4}}$	2

Table 2. Constants of Spalart-Allmaras turbulence model.

As usual with differential equations, there must be some boundary conditions for a solution to exist. These are $\tilde{\nu} = 0$ at walls, while it can initially be set to $\tilde{\nu} = 5\nu$ in the freestream.

2.4.3 Detached-Eddy Simulation (DES)

Detached-Eddy Simulation is a *hybrid method* for turbulence modeling. It is an effort to combine the advantages of RANS and LES while maintaining a reasonable computational load. It was first proposed by Spalart et al. in 1997 (19), and has since become an increasingly important tool in engineering CFD analyses. The purpose of DES is to employ LES in separated regions dominated by large eddies, while treating attached, thin boundary layers with RANS methodology so that the excessively fine streamwise resolution requirement for LES is avoided. This can save orders of magnitude in computational time (20).

A *DES limiter* is used to determine whether to use LES or RANS mode in different areas of the domain. It is defined as:

$$\tilde{d} = \min(d, C_{DES}\Delta) \tag{2.17}$$

where d is the same as for the S-A turbulence model, C_{DES} is a constant empirically set to 0.65 and Δ is defined as:

$$\Delta = \max(\Delta_x, \Delta_y, \Delta_z), \tag{2.18}$$

i.e. the largest dimension of the grid cell. The limiter function $\tilde{d}$ replaces the variable d in the S-A differential equation (2.15). Close to the wall the limiter chooses RANS mode, while LES kicks in further away from the wall.

As the DES limiter is dependent on the grid size Δ, an "inappropriate" grid can confuse the limiter so that it engages the LES model too close to the wall. The DES-optimized mesh is most likely too coarse in this area to accurately capture the eddy viscosity, so the friction is under-predicted. This phenomenon is called *modeled-stress depletion (MSD)*. Under-predicted friction can result in the model predicting a separation point that is too far upstream, therefore being unphysical. Instead, this separation is a result of grid properties and so is called *grid-induced separation (GIS)*. An example is shown in **Figure 7**. MSD and GIS have been proved to be the biggest practical problems arising from the use of DES (20).

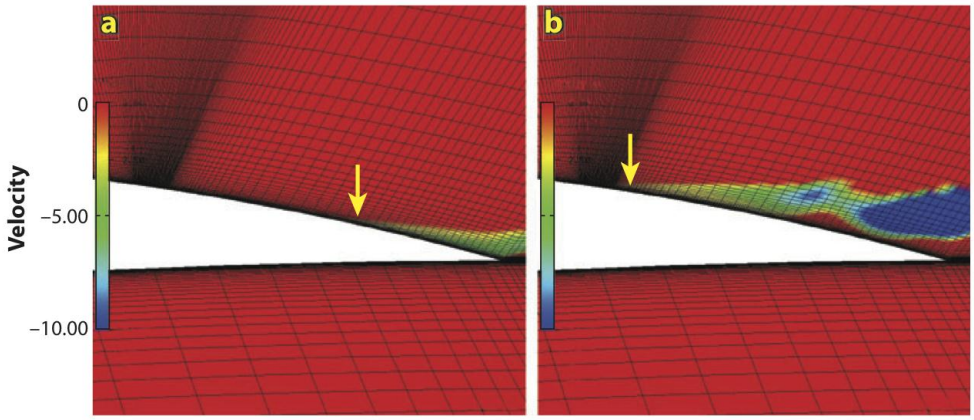

Figure 7. Left: Correct separation point; right: grid-induced separation.

The problem with inappropriate – or "ambiguous" – grids is illustrated by Spalart in **Figure 8** (20). The three different grids differ in the streamwise resolution. In the coarsest grid the boundary layer fits inside one streamwise cell spacing, so the DES model will use RANS for the full boundary layer (as intended). In the finest grid, which is optimized for LES, the DES model will use LES for the full boundary layer except very close to the wall where RANS will be used. Here, the grid is sufficiently fine to accurately capture the eddy viscosity, thus avoiding the problems of MSD and GIS (20).

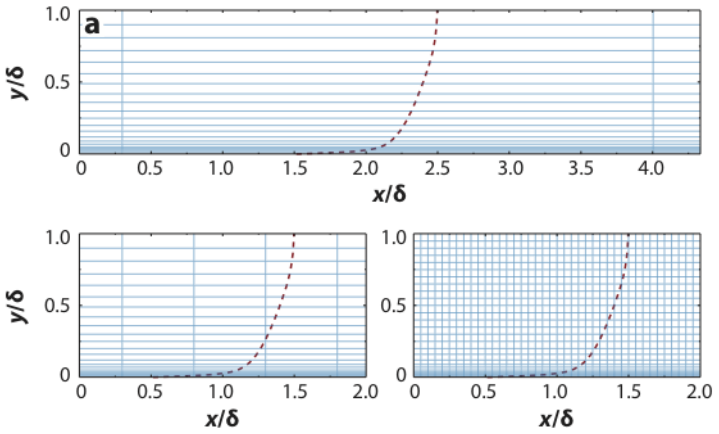

Figure 8. Only bottom left grid risk producing unphysical results in a DES, due to modeled stress depletion.

The medium-refined grid is the problematic one for DES models. The grid is fine enough to allow for LES use in significant parts of the boundary layer, but the grid is too coarse to capture all the significant velocity fluctuations in this region. The RANS model does not cover enough of the boundary layer to make up for this deficit. This is what gives the under-predicted friction, and can lead to grid-induced separation (20).

2.4.4 Delayed Detached-Eddy Simulation (DDES)

The above-mentioned problems were severe enough to force further development of DES. Spalart et al. proposed in 2006 a remedy for this problem, the DDES (21). It uses a modified limiter function that takes into account the calculated eddy viscosity in addition to the grid length. The new definition of the DES limiter is:

$$\tilde{d} = d - f_d \max(0, d - C_{DES}\Delta) \tag{2.19}$$

where:

$$f_d = 1 - \tanh(8r_d)^3$$
$$r_d = \frac{\nu_t + \nu}{\max\left(\sqrt{V_{i,j}V_{i,j}}, 10^{-10}\right) \cdot \kappa^2 d^2} \tag{2.20}$$

where $V_{i,j}$ are the velocity gradients.

The limiter function now detects if a point is inside the boundary layer and prohibits the LES mode to be active in that point, regardless of the grid dimensions. It is quite effective in achieving this and has become an important tool in industry (20). It is preferred to use DDES compared to DES, especially for less experienced users who do not have a lot of experience in designing proper DES meshes. DDES can also produce more reliable results than DES, especially in situations where it is difficult to determine if a separation point is physically correct, or is the result of the MSD phenomenon.

DDES is especially suited for external aerodynamics problems such as around vehicles – which involve high Reynolds numbers, large areas with attached flow and massive separation behind the vehicle. Important unsteady effects such as vortex shedding, wind gusts and periodic excitation from an AFC system can also be captured with DDES in contrast to RANS. These are the main reasons why DDES has been used in this project.

3 CFD IMPLEMENTATION

3.1 OpenFOAM

3.1.1 Background

The open-source software OpenFOAM (Field Operation And Manipulation) was initially developed at Imperial College in London, starting in the late 1980's. It was however first released as an open-source distribution in 2004 (22).

OpenFOAM is built on the C++ programming language and is unique in the sense that it allows users to freely access and alter the source code in order to customize the program for their needs. Because it is open-source it is also completely free to download, making it suitable for smaller companies lacking the financial strength to purchase expensive commercial CFD packages. The downside of using such open-source software is that there is not as extensive documentation and support available, as there is no one company responsible for development and sales of the product. So troubleshooting complex errors may be more demanding than with available commercial software.

3.1.2 Program structure

OpenFOAM is a text-based program optimized for the Linux environment. There are a number of GUIs that have been developed, but these have not been used in this project. Each simulation is set-up as a "case" with all the necessary input files located in sub-directories, as shown in **Figure 9**. Other than the mandatory files, one can easily add more depending on the objective – for example to sample data in selected points. All the interaction with the program is done through a terminal window.

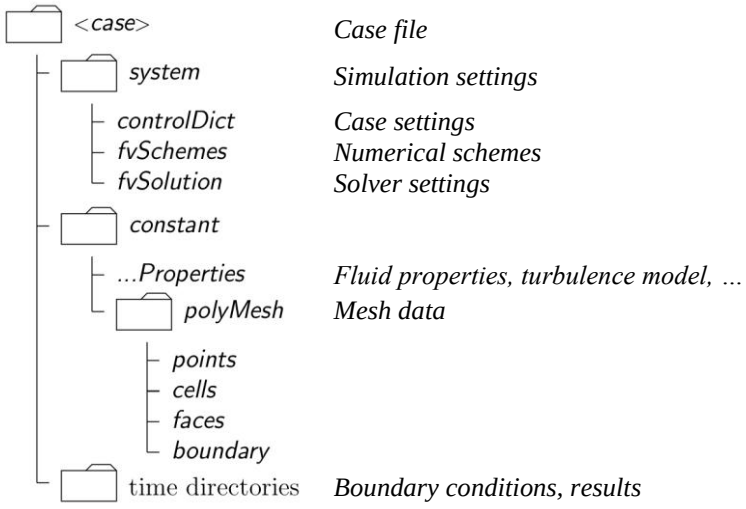

Figure 9. File structure of OpenFOAM.

3.2 Finite volume approach

OpenFOAM uses a finite volume approach for solving the equations. The computational domain is discretized into volumetric cells (**Figure 10**) that are defined by the mesh, called control volumes. The Navier-Stokes equations are then computed in integral form for each control volume in order to obtain the full flow field. The more control volumes, the bigger the numerical problem and the more detailed the solution will be.

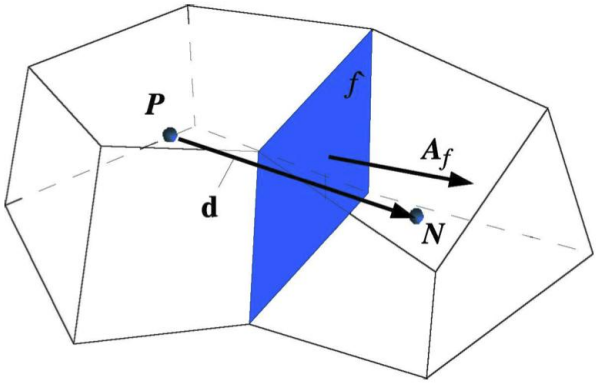

Figure 10. Control volumes in a finite volume mesh (23).

Each control volume has a collocation point – or node – in the middle, in which the properties of the flow field are stored. The flux through the connecting face **f** between two neighboring control volumes is calculated through interpolation between the two nodes **P** and **N**. The most straightforward interpolation method is linear, which is being used here.

If the cells are *non-orthogonal*, i.e. the face normal $\mathbf{A_f}$ is not parallel to the vector **d** connecting the neighboring nodes, the flux will be miscalculated. This will result in less accurate results and more unstable simulations. Thus, it is important to minimize the amount of non-orthogonality in the mesh-building process. However, a mesh will rarely be completely orthogonal, so it may be necessary to have the numerical solver do extra iterations to correct for non-orthogonality. This can improve the results and stability at the cost of a longer solution time.

3.3 Solver procedure

As previously mentioned, the solution of the Navier-Stokes equations involves an iterative procedure that differs depending on the chosen algorithm *(solver)*. The main challenge lies in the coupling between the pressure and velocity in equations (2.7) - (2.10). The pressure must be known in order to solve for the velocity, but to calculate the pressure the full velocity field must be known!

Roughly, one must go about as to first guess both the scalar pressure field and the velocity vector field, then solve the momentum equations using these guesses to get new preliminary velocity components. The momentum equations (2.8) - (2.10) can then be combined with the

continuity equation (2.7) to produce an equation for the pressure. This equation can be solved to obtain *p* when the velocity field is known. The pressure can then be used to correct the first solution for the velocity, to make sure that the flux satisfies the continuity equation. These steps can be repeated an arbitrary number of times until the solution does not change more than a prescribed limit. The details of this iterative procedure vary slightly for different algorithms, with the two most common ones described below.

3.3.1 SIMPLE algorithm

For steady-state problems the most common numerical method for solving the Navier-Stokes equations is the Semi-Implicit Method for Pressure-Linked Equations: SIMPLE. It operates according to the flow chart in **Figure 11**:

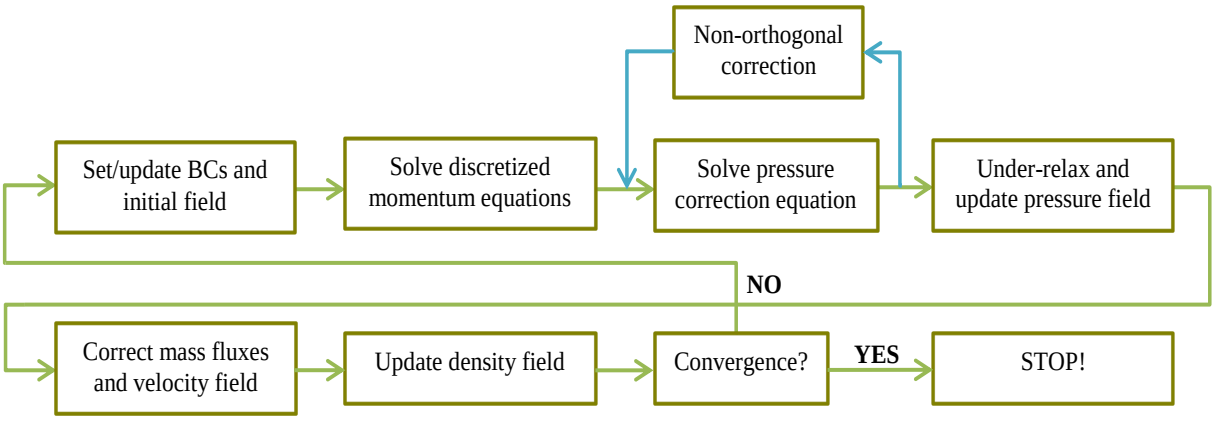

Figure 11. SIMPLE algorithm flow chart.

Under-relaxation is a method of improving stability of the solution, by limiting the delta-value of the variables between two subsequent iterations. Too large changes can easily make the solution diverge. But a large under-relaxation factor will make the solution converge slowly due to the simple fact that its purpose is to decrease the convergence rate. The user can tweak the under-relaxation factor in order to tune how aggressively the algorithm tries to make the solution converge. For simple problems with small gradients and a good mesh one may get away with a low factor, but problems with complex geometries and large gradients will require a larger under-relaxation factor to avoid numerical instability (at the expense of a longer solution time).

3.3.2 PISO algorithm

For unsteady problems the most common algorithm is the Pressure Implicit with Split Operators: PISO. It is detailed in **Figure 12**:

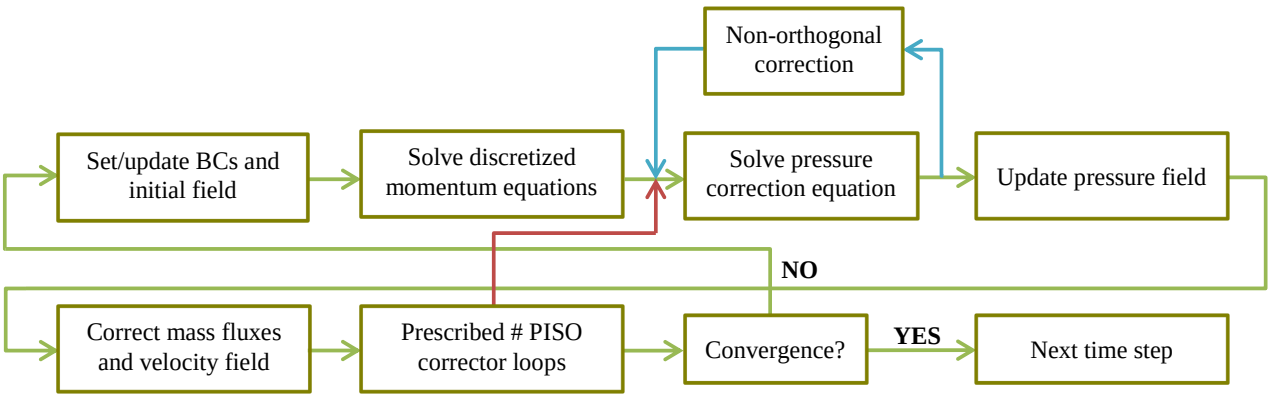

Figure 12. PISO algorithm flow chart.

The PISO algorithm is similar to the SIMPLE one, with the difference that no under-relaxation is applied and that the correction of the pressure and velocity fields generally is performed several times. The stability of the PISO algorithm depends on the Courant-Friedrich-Levy (CFL) number defined as:

$$CFL = \frac{V_{local} \cdot \Delta t}{d} \tag{3.1}$$

where d is the distance between two cell centers, V_{local} is the local velocity magnitude and Δt is the (local) time step. It can be interpreted as the number of cells one fluid particle travels from one time step to the next. The CFL number must be lower than 1 to ensure stability – a fact that limits the maximum possible time step during a simulation.

3.3.3 OpenFOAM solvers

OpenFOAM benefits from a wide variety of solvers, many developed for specific flow problems. Different simplifications can be made depending on the flow regime – for example laminar or turbulent, incompressible or compressible, and single- or multi-phase fluid.

Some commonly used OpenFOAM solvers are:

- *potentialFoam* (potential equation flow solver),
- *icoFoam* (transient, laminar flow solver),
- *simpleFoam* (steady-state, turbulent flow solver using the SIMPLE algorithm),
- *pisoFoam* (transient, turbulent flow solver using the PISO algorithm),
- *pimpleFoam* (merged PISO-SIMPLE algorithm; can support larger time steps than PISO without de-stabilizing the solution).

The merged PISO-SIMPLE algorithm uses an inner PISO loop to get an initial solution, which is then under-relaxed and corrected using an outer SIMPLE loop. This method enables unsteady simulations at CFL numbers larger than 1. In theory, very large CFL numbers could

be maintained if a large number of SIMPLE correction loops were applied along with large under-relaxation factors. But this has implications for the time-accuracy of the solution, because events that are shorter than the time step are missed completely by the solver. A too large time step generally smears the solution, regardless of the grid resolution. When using pimpleFoam one has to keep in mind that too large CFL numbers risk reducing the accuracy of the solution.

3.4 Schemes

Apart from the method of iteratively solving the Navier-Stokes equations, there are different ways of discretizing the different terms, which can be grouped into diffusive, convective and temporal terms. Different numerical discretization methods (*schemes*) can be applied to different groups independently of each other.

3.4.1 Spatial schemes

The goal of the spatial scheme is to efficiently estimate what goes on between nodes in the computational domain, i.e. the relation between the computed values stored at the nodes and the values at the cell faces. For convection, an upwind scheme estimates the face value to be the same as the nearest node upstream of the face in question. It can be seen as a "zero-order hold" of the variable, and is first order accurate, which means that the first truncated term is of second order. Upwind differencing is illustrated in **Figure 13**.

In contrast, a central difference scheme is equivalent to linear interpolation between the nearest node upstream and the nearest node downstream of the cell face. It is second-order accurate, and shown in **Figure 14**. Instinctively, central differencing seems to produce a better approximation of the value in between two neighboring nodes than what upwind differencing does. But central differencing is less stable and can produce oscillations around discontinuities and other regions of strong gradients. There are many different alterations/improvements of these schemes, some of which combine a second-order scheme with some upwind to stabilize it. There are also other types of schemes that are of higher-order accuracy and/or are nonlinear.

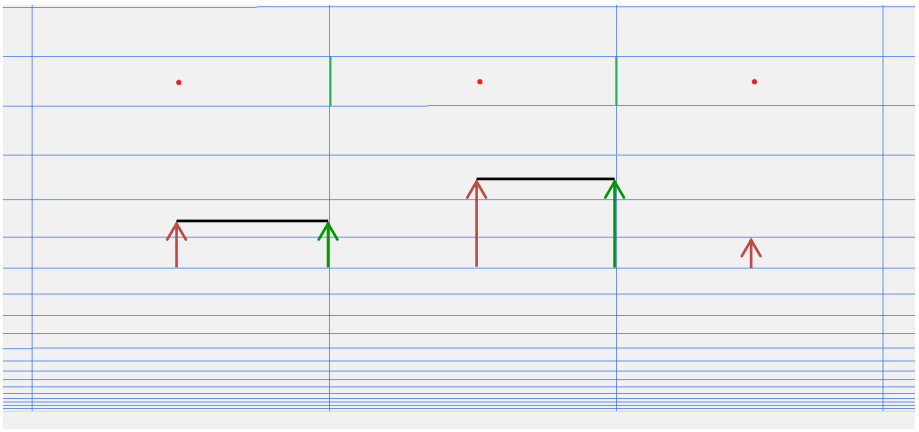

Figure 13. Upwind differencing: the red arrows indicate values calculated at the red nodes; the green arrows are the interpolated values at the green cell faces. The value is identical to the nearest node upstream (upwind).

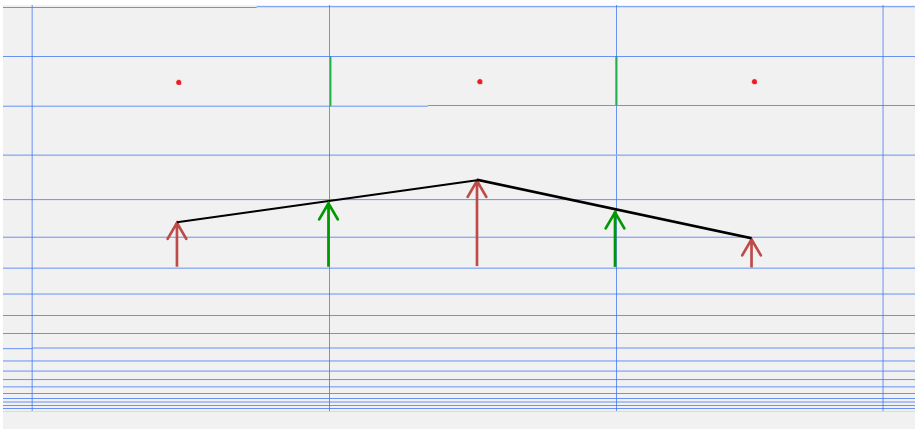

Figure 14. Central differencing: the green interpolated values are linearly interpolated between the node upstream and the one downstream.

3.4.2 Temporal schemes

The temporal scheme handles time derivatives of differential equations. The common explicit *Euler forward* is defined as:

$$\left(\frac{\partial u}{\partial t}\right)_{t=k} = \frac{u_{k+1} - u_k}{\Delta t} \tag{3.2}$$

Differential equations discretized with the Euler forward scheme can be solved directly because it is only a function of previous time steps. An implicit variant is the *Euler backward* scheme:

$$\left(\frac{\partial u}{\partial t}\right)_{t=k} = \frac{u_k - u_{k-1}}{\Delta t} \tag{3.3}$$

which can only be solved as a system of equations as the next time step is also dependent on information at that time. The *Crank-Nicolson* scheme uses information from two time steps to achieve second-order accuracy. It is also an implicit scheme, which must be solved as a system of equations.

$$\left(\frac{\partial u}{\partial t}\right)_{t=k} = \frac{u_{k+1} - u_{k-1}}{2\Delta t} \tag{3.4}$$

3.5 Boundary conditions

There are many different boundary conditions in OpenFOAM, with the most common being:

- *uniform* – sets a non-fixed, uniform value for a surface. Can be used to provide an initial velocity field inside the domain, which then changes as the solution evolves.
- *fixedValue* – sets a fixed, non-changing value for a surface. Is used for example to provide a no-slip condition at walls.
- *zeroGradient* – stipulates that the gradient of a variable is zero across a surface. One example is the pressure at the inlet and outlet patches.
- *slip* – sets the velocity component normal to a wall to a fixed value of zero and the tangential component to zero gradient.
- *inletOutlet* – changes between *fixedValue* and *zeroGradient* depending on the direction of the flow. If a patch is acting as an inlet it is defined as a fixed-value type, and if it is an outlet it gets a zero-gradient condition.
- *symmetry* – specifies that a vector should be "mirrored" across a surface. Can be used to only calculate one half of a symmetric body in order to reduce the mesh size.
- *cyclic* – sets a periodic boundary which is virtually connected to the corresponding cell on the opposite side of the domain. A vector that exits at one side will enter at the other.

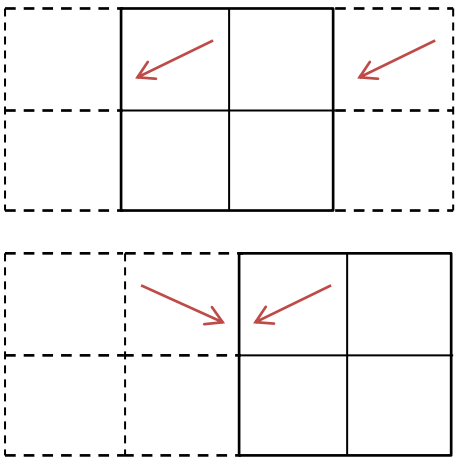

Figure 15. Top: cyclic BC; bottom: symmetry BC.

The dashed cells in **Figure 15** represent the non-modeled, virtual mesh that is defined by the boundary condition. Cyclic meshes are commonly used in circular combustion chambers, where it makes it possible to model only a part of the full chamber. Symmetry meshes will mirror the modeled geometry and its flow field. There can be problems with using symmetry and cyclic BCs in conjunction with LES/DES because of the eddies' inherent 3D structure. This will not be captured correctly if a too small part of the geometry is modeled, since the large eddies (which contain a lot of energy) may not fit inside the domain.

4 TEST SETUP

In order to understand the effects of an active flow control system, a suitable range of cases must be simulated and parameters that influence the result identified. The simulations will be done on a simplified car geometry with properties that trigger flow patterns that can be seen in real-world vehicles.

4.1 Vehicle model

The vehicle geometry is the *Windsor model*, which has been slightly modified from its original version to suit the needs of the thesis. The Windsor model resembles the more commonly used Ahmed body, but sports a more realistic front end, especially in crosswind situations. Such studies have for example been performed by Howell (24). The standard Windsor model has a sharp transition from the roof to the rear slanted edge, which can have different angles (backlight angles).

Here, the backlight angle is set to 35° which should be above the limit for separation. The transition from the roof is changed from a sharp edge to a radius of 200 mm to avoid having a separation point defined by the geometry. Instead, the separation is expected to be determined by the adverse pressure gradient. This should make it possible for a flow control system to delay the separation point by appropriate excitation of the flow, hence reducing drag. The Windsor geometry that has been used is illustrated in **Figure 16**:

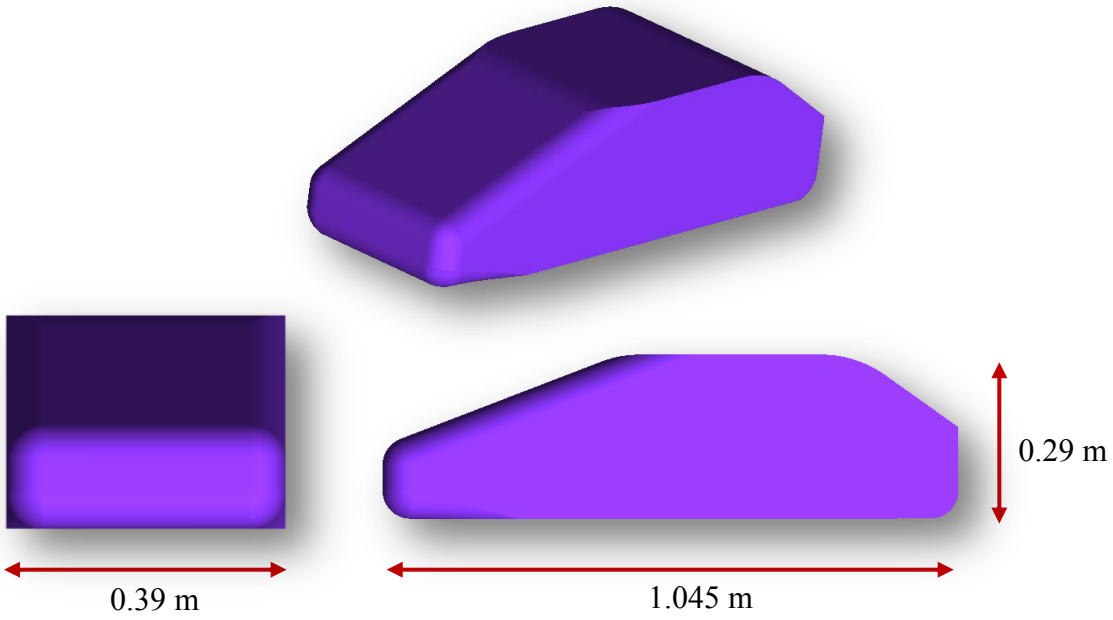

Figure 16. View and dimensions of the modified Windsor model.

Characteristic	Size
Dimensions (LxWxH)	1045 x 390 x 290 [mm]
Frontal area	0.113 m^2
Backlight angle	35°
Roof radii	200 mm
Front & A-pillar radii	50 mm
Diffuser radius	50 mm
Ground clearance	50 mm

Table 3. Properties of modified Windsor model.

4.2 Actuator

4.2.1 Design

The proposed actuator is of zero net mass flux-type, i.e. it generates an oscillatory airflow that interacts with the airflow over the vehicle. One example of actuator design is mentioned in a patent application filed by Creo Dynamics (25), and illustrated in **Figure 17**. It consists of one or several flexible membranes connected to piezo-actuators and placed in a cavity countersunk into the surface of the vehicle. The membranes vibrate in a desired manner to produce pressure fluctuations inside the cavity, much like a loudspeaker. The pressure fluctuations give rise to a fluctuating velocity through a slot in the external surface. Depending on the deflection of the membranes at any given time, the velocity through the slot can be directed both inward and outward – producing an oscillating velocity through the slot. The exit angle of the "synthetic jet" can be controlled via the design of the slot, covering a range from almost parallel to perpendicular to the wall.

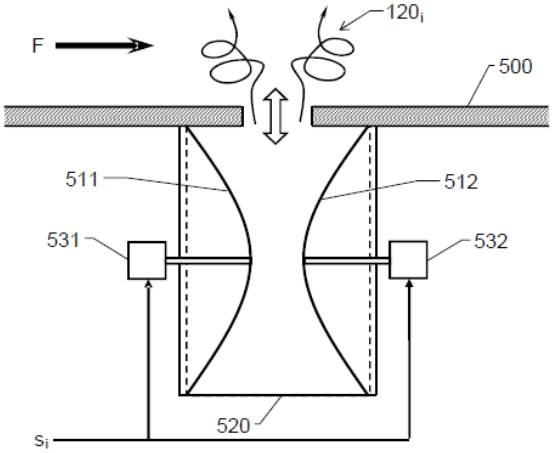

Figure 17. Proposed actuator design for ZNMF actuator.

Another possibility is to vibrate directly the surface of the vehicle which is in contact with the airflow. This will also produce an oscillatory excitation of the flow, similar to when using a cavity. Such a solution may have production advantages in that it takes up less space and may

be less prone to maintenance issues. Different actuator designs must be simulated to be able to make an informed design decision, although this is outside the scope of this thesis.

4.2.2 Actuator research

El-Alti et al. of Chalmers University of Technology have performed experiments on a simple design for a synthetic jet actuator (26). The actuator consisted of a loudspeaker mounted in the bottom of an enclosed box, with a slot in the top side. The main conclusions were that it is possible to achieve an exit velocity of approximately 40 m/s for slots a few millimeters wide, that a momentum coefficient close to 1 % is possible (using the width of a standard truck as reference length in (1.4)), and that the cavity volume does not play a significant role for the results. The importance of this study is that it gives a rough view of the velocities possible, which will be important for the simulations here.

4.2.3 Actuator positioning

To be as effective as possible, it is important that the actuator is positioned as close to – but upstream of – the average separation line of the vehicle as possible. In some cases where the separation is fixed by the geometry this line is fairly simple to determine; in other cases engineering judgment or simulations should determine where to position the actuator(s). The farther away from the separation line the actuators are, the less their effect will be. If an actuator for example was placed in the front of the vehicle, its energy would have been dissipated by the time the fluid particles reach the rear, where the separation occurs.

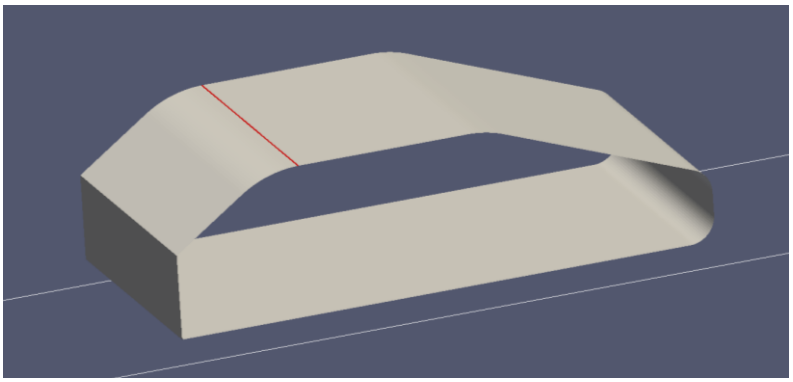

Figure 18. The red line shows the actuator slot on the Windsor model.

When designing the Windsor geometry used here, it has been estimated that the separation will likely occur somewhere over the rounded edge connecting the roof with the slanted back. So the actuator is positioned just before the curvature starts, as illustrated in **Figure 18**. This placement is a compromise between minimizing the distance from the point of separation, but with some margin so as to not end up having the actuator being downstream of the separation line. As can be seen, the actuator slot is continuous, which is an initial design attempt. Also segmented slots that do not cover the whole width of the vehicle will be simulated (**Figure 19**).

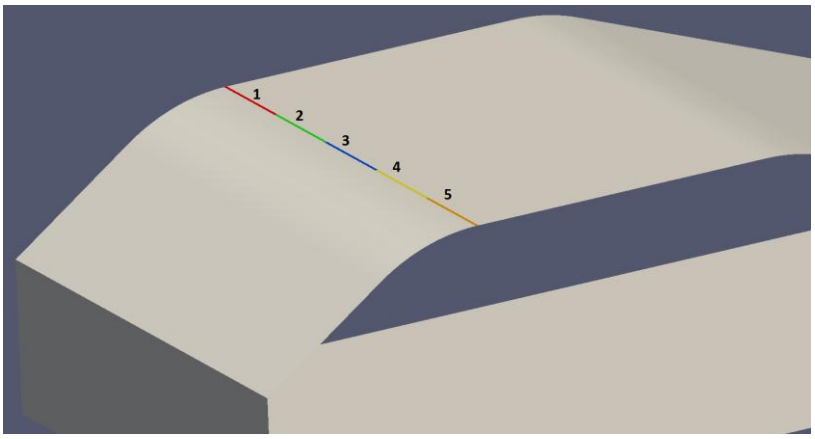

Figure 19. Example of five actuator slot segments. Any combination of these can be active in a simulation.

4.2.4 Actuator boundary condition

The velocity through the slot is set as a time-varying boundary condition. In OpenFOAM, this can be done by using the built-in boundary condition *timeVaryingUniformFixedValue*, which reads values from a text file that can be generated by for example MATLAB (27). The boundary condition is in all cases set to a sinusoidal velocity of different frequencies and amplitudes. An example is shown in **Figure 20**:

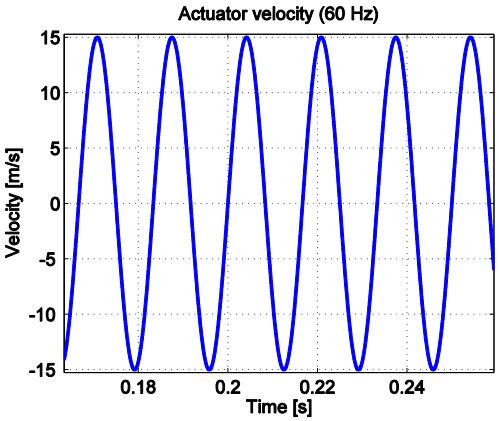

Figure 20. Actuator boundary condition; amplitude: 15 m/s, frequency: 60 Hz.

4.3 Meshing

Meshing is done in Ansys ICEM (28). As the geometry is fairly simple, a hexahedral mesh is used. It provides higher accuracy and can be more robust than a tetrahedral mesh of the same cell count.

4.3.1 Computational domain

A CAD model of the Windsor geometry is first imported into ICEM, and the computational domain set up. It is constructed to be large enough as to avoid any undesired effects of blocking or other influence from the edges of the domain. The downside of having an unnecessarily large domain is increased computational time, so it could be beneficial to spend some time in optimizing the domain size. This is not done here however, so the chosen domain size as shown in **Figure 21** should be more than sufficient in keeping interference to a minimum.

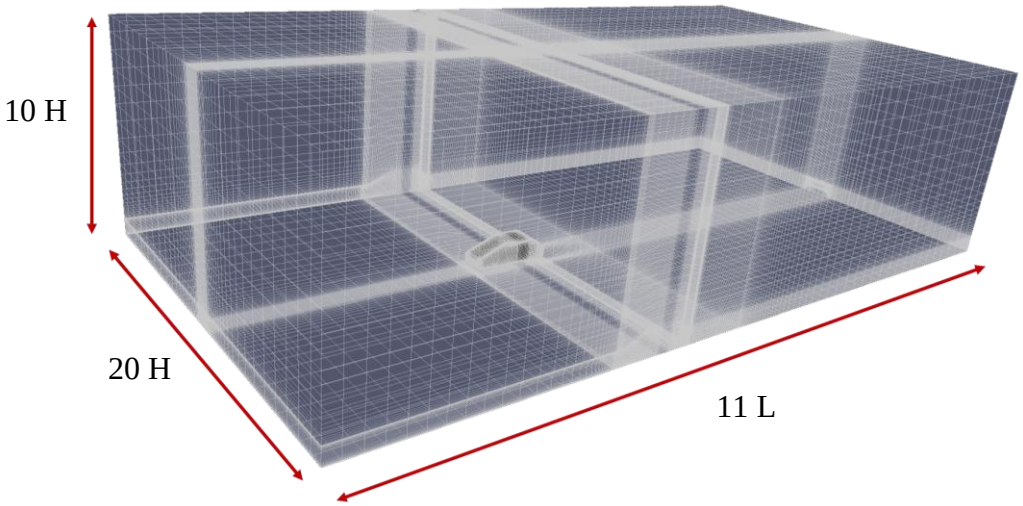

Figure 21. Computational domain used for 3D simulations.

4.3.2 Blocking & cell spacing

With the domain set up, the geometry is blocked in 2D according to:

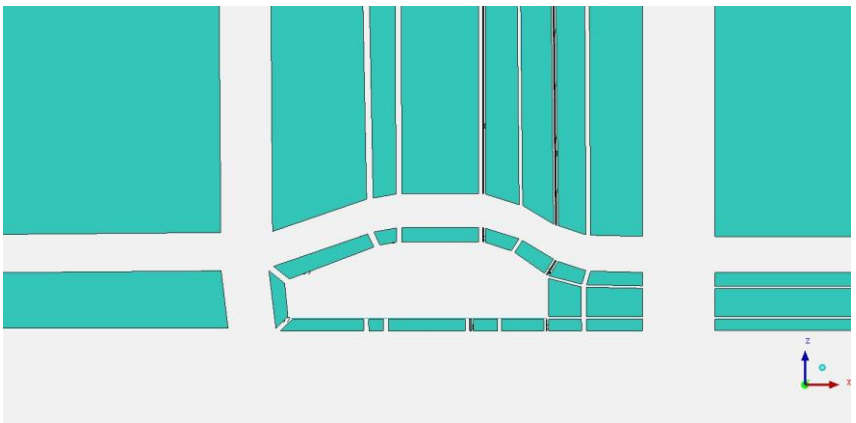

Figure 22. Blocking for 2D Windsor model.

The cell spacing closest to the wall is for all meshes set to around 0.2 mm, which gives an average y^+-value of 25-30. So it is suitable to use wall functions in the RANS regions, which saves considerable resources compared to having a fully resolved boundary layer.

4.4 Computational resources

All computations except 3D simulations are done on a computer with the following specifications:

Processor	Intel Core i7-2720QM @ 2.2 GHz (4 cores)
Memory	4 GB
Graphics card	Nvidia Quadro 1000M
Operating system	Ubuntu emulation in Windows 7 64-bit

Table 4. Specifications: 2D & semi-3D simulations.

Because of significant increased complexity when doing 3D simulations, these are done on a more powerful computer:

Processor	Intel Xeon X5550 @ 2.67 GHz (8 cores)
Memory	24 GB
Graphics card	Nvidia Quadro FX 1800
Operating system	Ubuntu 5.7

Table 5. Specifications: 3D simulations.

4.5 Simplifications

4.5.1 Actuator modeling

One of the more challenging obstacles to overcome is the limited computational resources available, so it is important to always weigh what trade-offs can be made to simplify the problem and still capture the important details. One of the main simplifications done in all AFC simulations is to not model the cavity in which the actuator membrane sits, but instead only model the resulting slot velocity.

The slot is modeled by setting part of the wall as an inlet-outlet patch, which is then fed with a sinusoidal velocity. When AFC is turned off the slot is considered a smooth wall. In reality, the slot would act as a disturbance on the flow passing over it – how severe depending on the width of the slot. This effect is neglected here because it is not expected to have a large influence for a slot a few millimeters wide. The dynamics of the cavity itself is described by a transfer function from the displacement of the actuator membrane to the resulting velocity through the slot. If a desired velocity is to be achieved, this effect must be compensated for when controlling the actuator – something which is not considered here.

4.5.2 Domain

To familiarize oneself with the important parameters without needing weeks of simulation time, a step-by-step increase in complexity is implemented. First, the domain is limited to cover only the model. A domain width of 0.5 m is used, which is 48 % of the car length. In a 2D setting there is only one cell covering the entire domain width. This makes it possible to perform many runs quickly in order to find suitable boundary conditions and see if AFC can be made to work for a simplified flow field, completely without 3D effects.

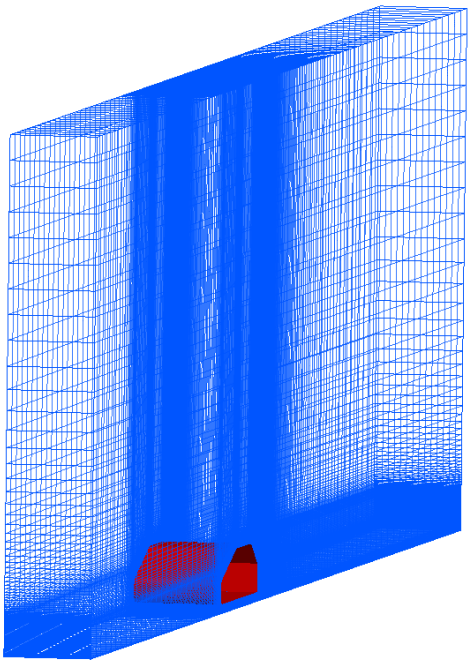

Figure 23. 2D/semi-3D domain

If this is the case, one can then first move on to a more complex "semi-3D" setting, where there are several cells across the width of the car but still no sides, so all fluid particles are forced either above or below the car (this corresponds to an infinitely wide vehicle). Finally, a full, realistic 3D simulation is performed to see the real-world potential of the system. Using this approach, a deeper understanding of how different aspects of the flow affect the efficiency of the AFC system can be achieved. Also, it allows experimentation with different settings within a reasonable time in the 2D domain.

4.5.3 Mesh detail

To make sure the mesh is fine enough to give accurate results, usually a mesh refinement investigation is carried out with gradual refinement of the mesh until convergence. The limited resources will however limit the amount of mesh refinement possible before the computation times become too large. The meshes used in the simulations are therefore rather coarse, and cannot be expected to give very accurate absolute values for the forces and coefficients. What is more interesting however, is the difference when AFC is active vs. the reference cases. As the comparison is done on the same mesh, it is hoped that there will be similar errors and hence that the delta-values will be significantly more accurate. The main conclusions will therefore be drawn from the difference rather from absolute values which should not be read too much into.

4.6 General settings

4.6.1 Introduction

All simulations are performed with DDES since transient effects must be captured when simulating an active flow control system. It has been shown to perform well for this type of flow situation: external aerodynamics subject to massive separations. DDES makes it possible to both look at instantaneous flow fields as well as time-averaged ones. Consequently it is easier to analyze details of what is going on in different areas at any given time, while still being able to see the overall change in flow characteristics over a longer time.

Most DDES runs are preceded by RANS calculations with AFC disabled in order to set up an initial flow field. Both the DDES and RANS calculations use the Spalart-Allmaras turbulence model with default parameters from OpenFOAM. The data sampling frequency is for all cases 1000 Hz.

4.6.2 Cases

The goal with the simulations is to evaluate a potential AFC system in cases that are as realistic as possible, given the simplifications described earlier. The global settings used in all simulations are given in **Table 6**. The only parameter of the flow that is changed is the freestream velocity (only done in 2D).

Characteristic	Case 1	Case 2
Freestream velocity	25 m/s	30 m/s
Air density ρ	1.225 kg/m^3	1.225 kg/m^3
Kinematic viscosity ν	$1.494 \cdot 10^{-5}$ m^2/s	$1.494 \cdot 10^{-5}$ m^2/s
Reynolds number (car length)	$1.75 \cdot 10^6$	$2.10 \cdot 10^6$

Table 6. General case settings

4.6.3 Boundary conditions

Boundary conditions for the detached-eddy simulations are provided by the converged RANS runs. The boundary conditions for the first time step for RANS is summarized in **Table 7**:

Boundary	nut	nuTilda	p	U (x y z)
Inlet	*inletOutlet 0.039*	*inletOutlet 0.039*	*zeroGradient*	*inletOutlet (30 0 0)*
Outlet	*inletOutlet 0.039*	*inletOutlet 0.039*	*zeroGradient*	*inletOutlet (30 0 0)*
Windsor	*nutUSpalding-WallFunction 0*	*fixedValue 0*	*zeroGradient*	*uniform (0 0 0)*
Actuators (off)	*nutUSpalding-WallFunction 0*	*fixedValue 0*	*zeroGradient*	*uniform (0 0 0)*
Actuators (on)	*inletOutlet 0.039*	*inletOutlet 0.039*	*zeroGradient*	*TVUFV**
Sky	*nutUSpalding-WallFunction 0*	*fixedValue 0*	*slip*	*slip*
Ground	*nutUSpalding-WallFunction 0*	*fixedValue 0*	*zeroGradient*	*uniform (30 0 0)*
Sides	*empty (2D)* *cyclic (semi-3D)* *cyclic (3D)*	*empty (2D)* *cyclic (semi-3D)* *cyclic (3D)*	*empty (2D)* *cyclic (semi-3D)* *cyclic (3D)*	*empty (2D)* *cyclic (semi-3D)* *cyclic (3D)*

Table 7. 2D RANS boundary conditions. **TVUFV = timeVaryingUniformFixedValue*

The wall function being used (Spalding) is an adaptive wall function that can compensate for different values of y^+. The value for $\tilde{\nu}$ can be estimated through

$$\tilde{\nu} = \sqrt{\frac{3}{2}} \cdot (U_\infty I l) \tag{4.1}$$

where I is the turbulence intensity and l the turbulent length scale, which is a measure of the size of the largest eddies. A turbulence intensity of 5 % is assumed, and l is assumed to be 7 % of a characteristic length – in this case the height of the model.

The steady-state RANS runs are done without AFC because time-varying events cannot be simulated correctly in steady-state. When performing DES with AFC on, the actuator boundary is changed from being treated as a wall to being treated as an inlet-outlet.

4.6.4 Schemes

The schemes used for all simulations are summarized in **Table 8**:

Type	Scheme
Interpolation	*Linear*
Temporal: RANS	*Steady-state*
Temporal: DES	*Crank-Nicolson + Euler backward*
Gradient	*Gauss linear*
Divergence: U	*Gauss limitedLinearV 1*
Divergence: $\tilde{\nu}$	*Gauss upwind*
Laplacian	*Gauss linear, corrected*

Table 8. Summary of numerical schemes used.

The temporal scheme for the transient DES is a mix of the Crank-Nicolson and Euler schemes. This improves stability by adding some upwind at the cost of accuracy, but it is more accurate than a pure first order scheme. The divergence scheme for the velocity is a second order TVD scheme, but with the use of upwind discretization in the vicinity of large gradients and discontinuities. The extent of the upwind area is determined by the factor succeeding the scheme name, ranging from 0 (least upwind) to 1 (most upwind). The OpenFOAM user manual recommends using factor 1 in order to aid solution stability. The linear Laplacian scheme is corrected for non-orthogonality.

4.6.5 Solution settings

A summary of the settings for the solution procedure is found in **Table 9**. The *pimpleFoam* solver was used for the transient simulations because it enabled a larger time step than *pisoFoam* without diverging. For the heavier semi-3D and 3D simulations a *Geometric-Algebraic Multi-Grid (GAMG)* was used to improve performance. It was found that cases when the solver spends a relatively large portion of the time solving the pressure equation, which is the case for large meshes, a multi-grid method results in significantly faster computations.

It works by first calculating the solution in a much coarser grid and then projecting the results on a finer grid. This can be done in several steps in order to gradually build up the final flow field. The extra work of coarsening and refining the mesh is more than weighed up by the faster calculation times (when using large meshes). For cases with smaller meshes, such as in 2D, *GAMG* is about 50 % slower than the standard *Preconditioned Conjugate Gradient (PCG)* method.

Setting	2D	semi-3D	3D
Solver	*simpleFoam (RANS)* *pimpleFoam (DDES)*	*simpleFoam (RANS)* *pimpleFoam (DDES)*	*simpleFoam (RANS)* *pimpleFoam (DDES)*
Time step	$2.5 \cdot 10^{-5}$ *s*	$5 \cdot 10^{-5}$ *s*	$1 \cdot 10^{-5}$ *s*
Matrix solver	*PCG/PBiCG*	*GAMG/PBiCG*	*GAMG/PBiCG*
Absolute tolerance	10^{-4}	10^{-4}	10^{-4}
Relative tolerance	0	0	0.1
# Non-orthogonal correctors	0	0	0
Relaxation factors	0.5	0.5	0.4 (p), 0.7 (U, $\tilde{\nu}$)

Table 9. Summary of OpenFOAM solution settings.

5 RESULTS – 2D

5.1 Mesh

The 2D mesh for the Windsor model is illustrated in **Figure 24**. As described earlier, there is only one cell covering the entire width of the vehicle, so that no 3D effects at all are present in the results.

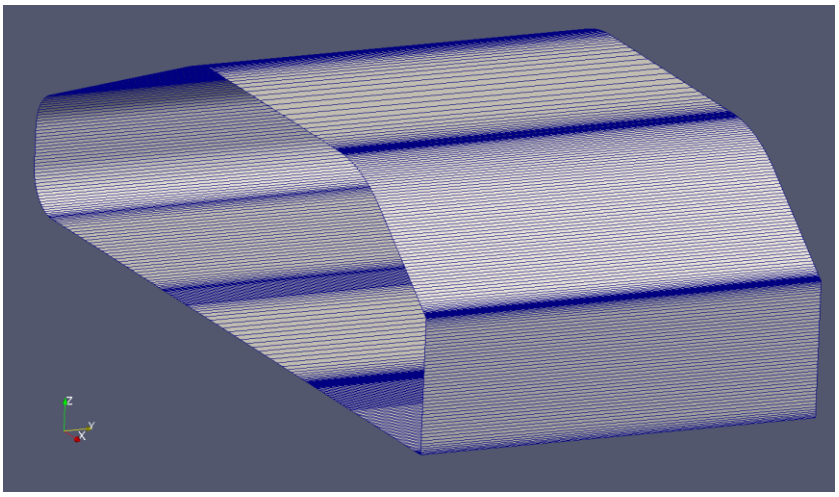

Figure 24. View of the Windsor model 2D mesh – seen from behind.

The most important mesh parameters are collected in **Table 10**:

Cells	52259
Windsor surface faces	452
Max aspect ratio	227
Non-orthogonality, average	11.3°
Distance: wall – first cell	~ 0.2 mm (y^+ *15-25*)
Cell growth ratio	$\leq$ 1.2

Table 10. 2D mesh info

A side view of the 2D mesh is shown in **Figure 25**. The mesh is refined in important areas such as around the AFC slots, at the trailing edges and in the wake. It is a structured, hexahedral mesh that includes a single O-grid around the vehicle.

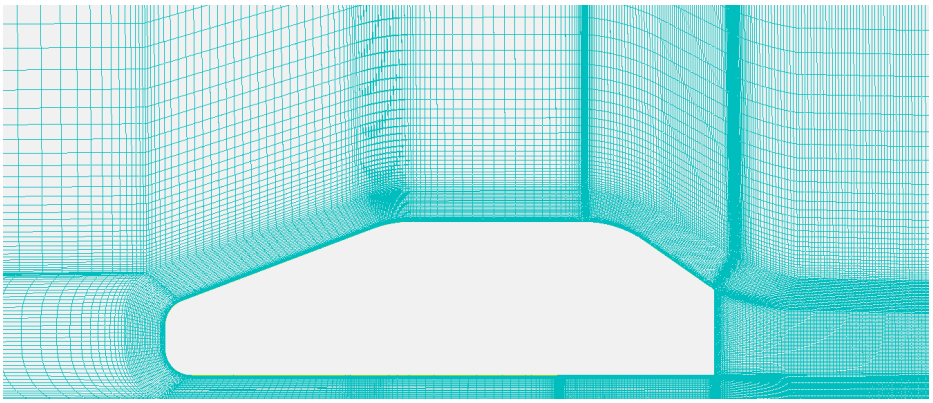

Figure 25. Side view of 2D mesh.

5.2 Reference case (AFC off)

5.2.1 Drag coefficient

First, an investigation of the flow field and the forces of the unforced reference case (AFC off), is carried out. **Figure 26** shows the drag coefficient as a function of time for the two tested velocities: 25 and 30 m/s. Time is normalized with the freestream velocity and the length of the Windsor model. This way it is easier to compare the results with other models. The normalized time t^* gives the number of times a fluid particle would have passed by the entire length of the vehicle.

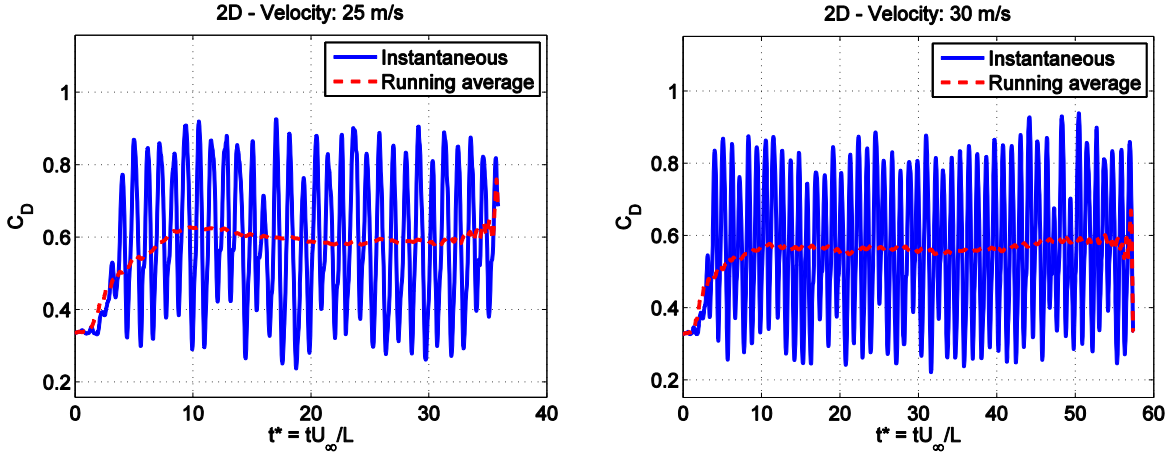

Figure 26. Drag coefficient as a function of non-dimensional time with AFC turned off, for two velocities.

The big difference between the maximum and minimum values of C_D is a result of the 2D domain. When the entire energy of the flow is forced to lie in a single plane, the result is a very strong vortex shedding process. The dashed red curve shows a running average of 0.5 seconds, which corresponds to 12-14 normalized time units depending on velocity. The solution is more or less converged after 10-15 time units, and the average value of C_D is around 0.57-0.58. The converged RANS solution gives a C_D of 0.335 (the initial value in the

transient simulation), which is a much more reasonable value for a car. A 2D LES/DES simulation is therefore not accurate in predicting forces correctly, but it is still being used here to predict *differences* when AFC is activated.

5.2.2 Frequency analysis

The energy spectral density (ESD) of a time signal is defined as the square of the magnitude of the Fourier transform:

$$ESD = \frac{F(\omega) \cdot F^*(\omega)}{2\pi}$$
$$F(\omega) = \int_{-\infty}^{\infty} f(t) e^{-i\omega t} dt \qquad (5.1)$$

The ESD of the drag coefficient time signals in **Figure 26** is calculated after the mean values have been filtered out:

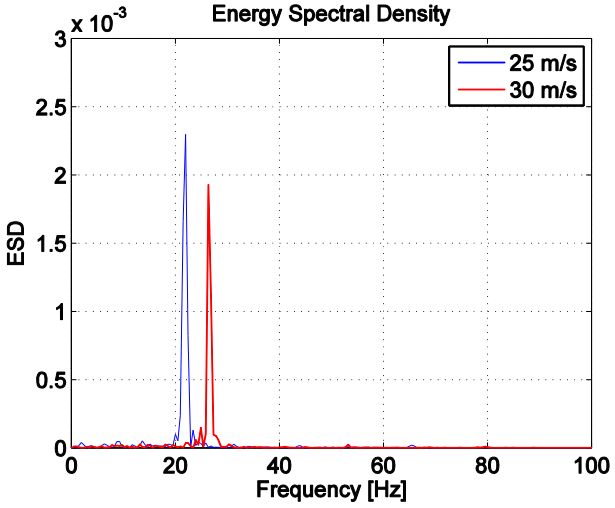

Figure 27. Energy Spectral Density of C_D for the reference cases.

The ESD reveals a very clear peak for each of the velocities corresponding to the shedding frequency. There is very little energy at other frequencies. As expected, the shedding frequency increases with velocity. An interesting number that describes shedding processes is the Strouhal number, which is defined as:

$$St = \frac{f_{shed} h}{U_\infty} \qquad (5.2)$$

using the height h as the reference length. The shedding frequencies and calculated Strouhal numbers of the reference cases are collected in **Table 11**:

Freestream velocity	Shedding frequency (f_{shed})	Strouhal number (St)
25 m/s	22.0 Hz	0.255
30 m/s	26.4 Hz	0.255

Table 11. Features of the vortex shedding process.

The Strouhal numbers of the main shedding frequencies are identical. The number is slightly higher than for a cylinder at similar Reynolds numbers, which has a Strouhal number of around 0.2. One would expect the Strouhal number of the Windsor model in 2D to be in the vicinity of a cylinder as the shapes are somewhat similar. The results are an indication that the shedding frequency is reasonable and that the simulations have produced results that are not obviously incorrect in capturing the flow physics.

5.2.3 Flow physics

The flow field around the Windsor model is characterized by a fairly large wake behind the vehicle caused by separation at around mid-point of the curvature connecting the roof to the rear slanted edge. The point of separation is near the expected location (as described earlier). The air is accelerated over the roof and reaches the highest velocity over the front roof curvature. Underneath the car the air is accelerated to about 40 m/s. There is a large vortex located at the rear of the vehicle, which is being sucked into the wake from underneath the car. This large vortex creates a low pressure, which is the main cause of vehicle drag. The mean flow field is shown in **Figure 28**.

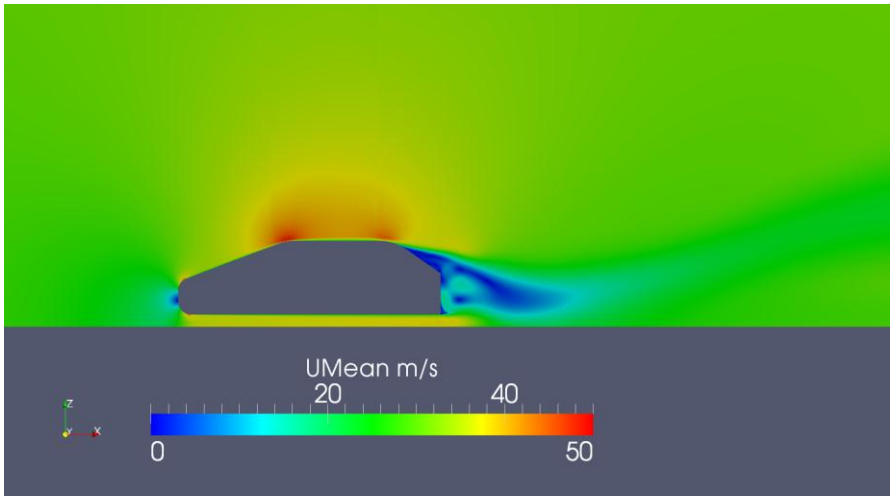

Figure 28. Mean velocity field: $U_\infty = 30$ m/s, AFC off

The build-up of this large vortex is initiated by a low pressure in the wake. It then grows by sucking in air from below the vehicle, and finally lets go and travels downstream in the wake. This process is shown in **Figure 29**, where one large vortex has travelled a few decimeters downstream as the next one is being built-up. Just before they let go, the vortices contain the most energy and create the lowest pressure in the wake. This is the time when the drag coefficient is at its maximum. The whole process is repeated with the vortex shedding

frequency. Hence, it can be concluded that the main drag contribution in 2D is from the large vortices which constitute the shedding process.

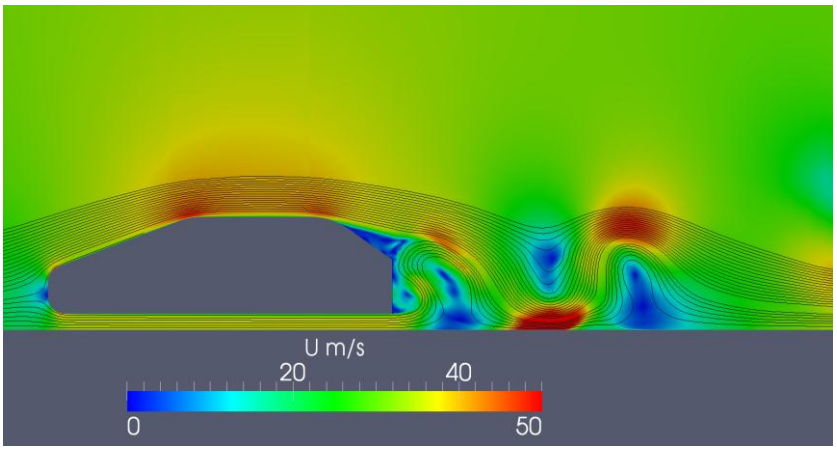

Figure 29. Instantaneous velocity field: $U_\infty = 30$ m/s, AFC off

5.3 Influence of active flow control

As discussed, the objective of an AFC system is to inject energy into the airflow to delay separation or in other ways alter the airflow in a desired manner. This can be seen in the CFD simulations by for example looking at the vorticity ω:

$$\boldsymbol{\omega} = \nabla \times \boldsymbol{V} \tag{5.3}$$

In **Figure 30**, it can easily be seen that an effect of the actuator injecting energy into the flow is that the vorticity in that area is greatly increased. The vorticity helps energizing the boundary layer, which keeps it from separating a little while longer. The vorticity is then gradually diffused in the downstream regions, in the wake.

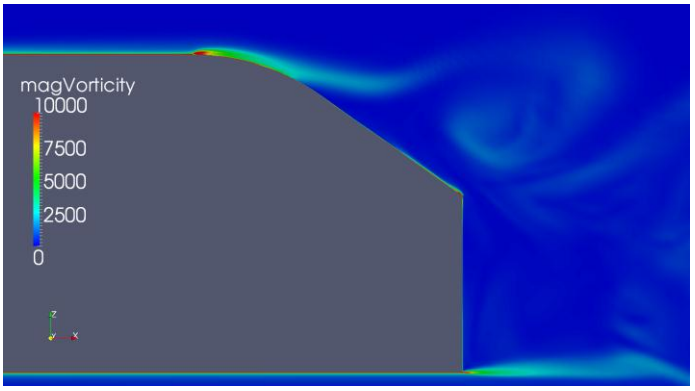

Figure 30. Vorticity magnitude with the AFC system active.

The velocity field around the actuator slot is altered differently depending on which phase the actuator is currently in. **Figure 31** highlights the difference when the actuator is sucking air compared to when it is blowing air into the boundary layer. The separation line is moved slightly downstream when the actuator is sucking air through the slot compared to when it is blowing. A close-up of the actuator in **Figure 32** reveals a small separation bubble forming immediately downstream of the slot during the blowing phase.

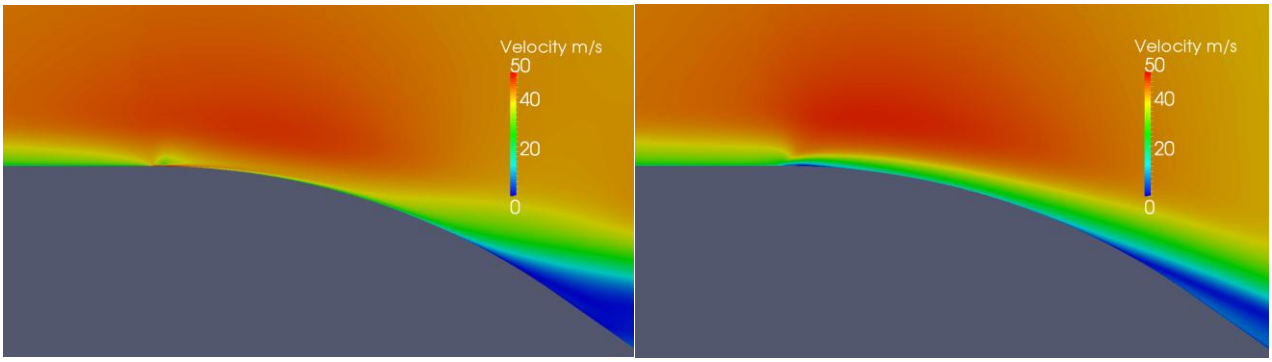

Figure 31. Left: suction phase; Right: blowing phase

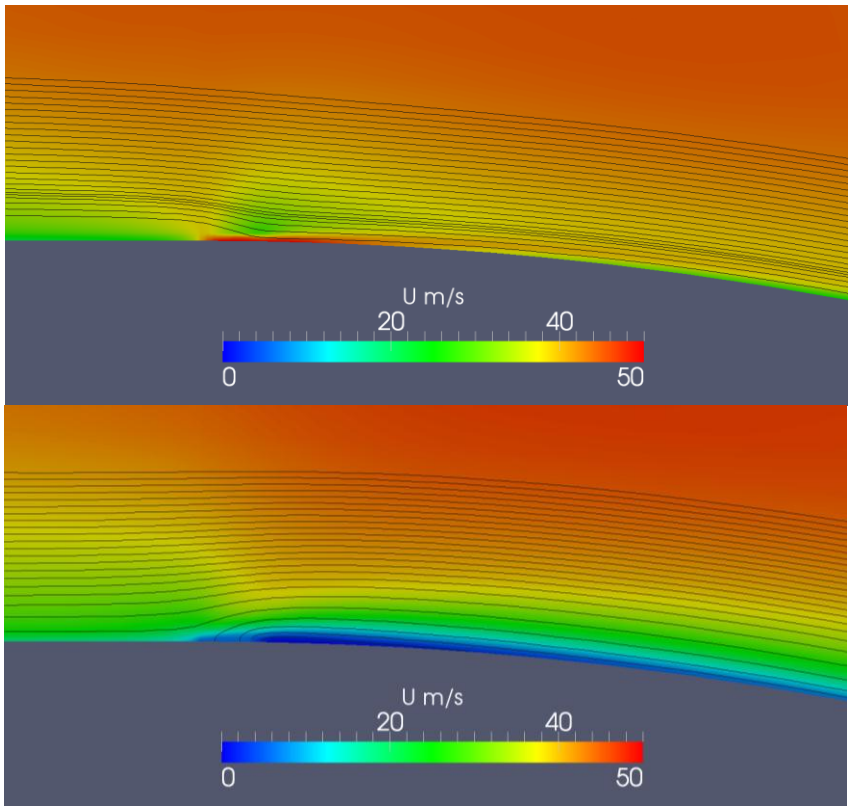

Figure 32. Top: close-up suction phase; Bottom: close-up blowing phase

5.4 Parameter study

The faster 2D simulations are best used to evaluate how varying different parameters of the flow control system affects the flow field. The parameters that are varied are: actuator amplitude (slot velocity), actuator frequency, slot width (mass flow) and freestream velocity.

5.4.1 Selected results

A number of different frequencies were tested at different actuator amplitudes. **Figure 33** shows some distinct differences in the simulated 2D results, for 30 m/s freestream velocity:

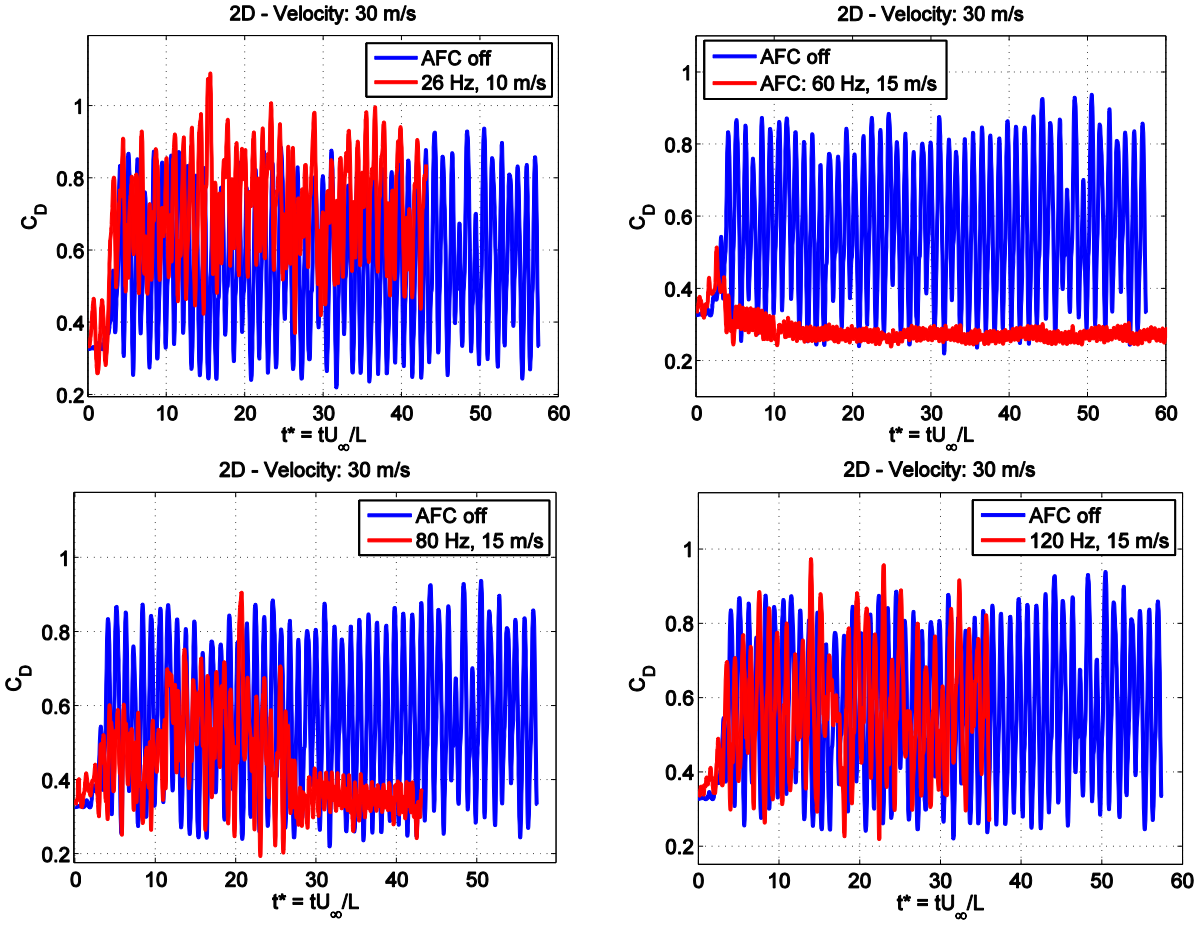

Figure 33. Four actuator frequencies all showing different characteristics.

In the first plot the actuator is run at the same frequency as the vortex shedding process. The result is a drastic increase in average C_D. A phase-shift of 180 degrees for the actuator velocity was also tried, with similar results. The 60 Hz-case shows a massive decrease in drag (over 50 %!), due to effects that will be investigated further in a little while. At 80 Hz forcing frequency a borderline case exists, where it takes a while for the system to fall into a state of very low drag. During the first 25 time units the drag is lower than without AFC, but not near as low as for 60 Hz. Finally, the 120 Hz-case shows that the actuators lose their effectiveness

with a time history that does not differ much from the unforced reference case. The behavior for 25 m/s freestream velocity is very similar to 30 m/s, with the results omitted from this section for the sake of clarity.

5.4.2 Frequency & amplitude

In **Figure 34**, time-averaged drag coefficients relative to the reference cases (AFC off) are collected:

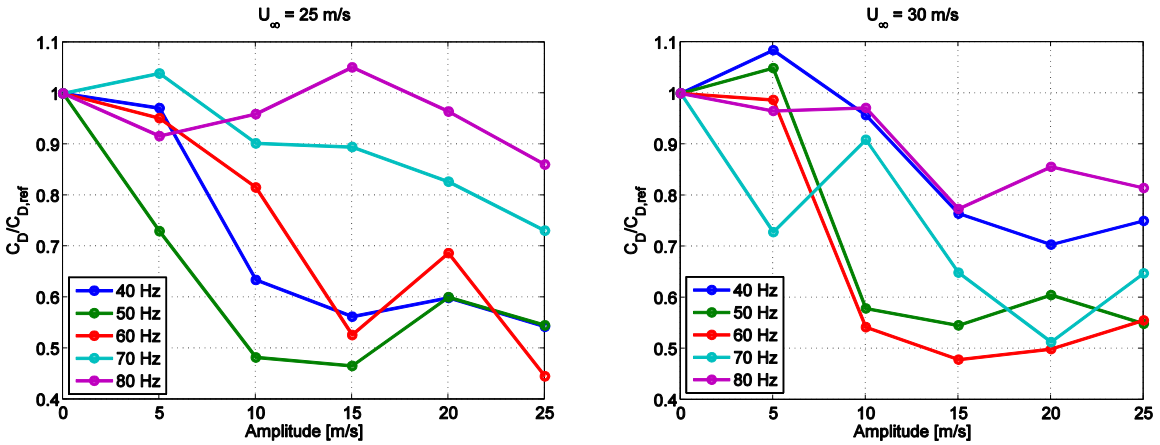

Figure 34. C_D as a function of actuator amplitude for different frequencies.

It is evident that both frequency and amplitude have an impact on the drag coefficient. There is generally a fairly linear decrease in drag when increasing the amplitude from zero to 10-15 m/s, after which the decrease in drag saturates and eventually starts increasing again at high amplitudes. The most effective frequencies vary slightly with different freestream velocities, but are generally in the range 40-70 Hz. This corresponds to approximately twice to three times the natural shedding frequency. This is more clearly illustrated in **Figure 35**, where the general "good regions", in terms of drag reduction, are located.

For a higher velocity, the blue regions are shifted to a higher frequency, but the magnitude of the drag reduction stays virtually the same. The optimum actuator frequency thus seems to scale as a factor of the shedding frequency. For the Windsor model in 2D, the ratio between the optimum actuator frequency and the shedding frequency is for both freestream velocities equal to 2.3.

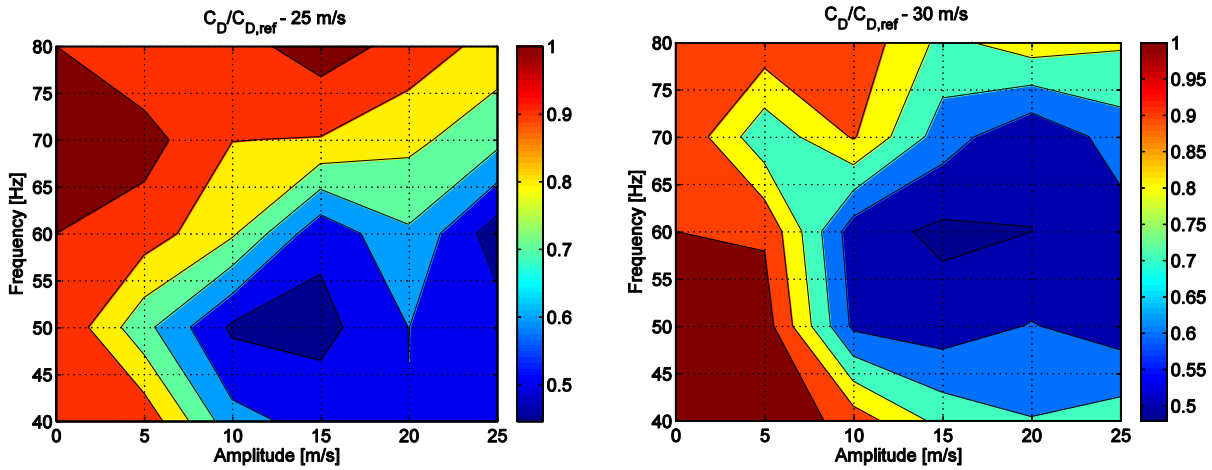

Figure 35. Contour plot for relative decrease in drag coefficient for different frequencies and amplitudes.

5.4.3 Mass flow & slot velocity

To investigate whether it is the velocity through the slot (= actuator amplitude) or the mass flow that matters the most for decreasing drag, two different slot widths were tried to keep the mass flow constant while varying the slot velocity – 1.5 mm and the standard 3.0 mm. **Figure 36** shows the results.

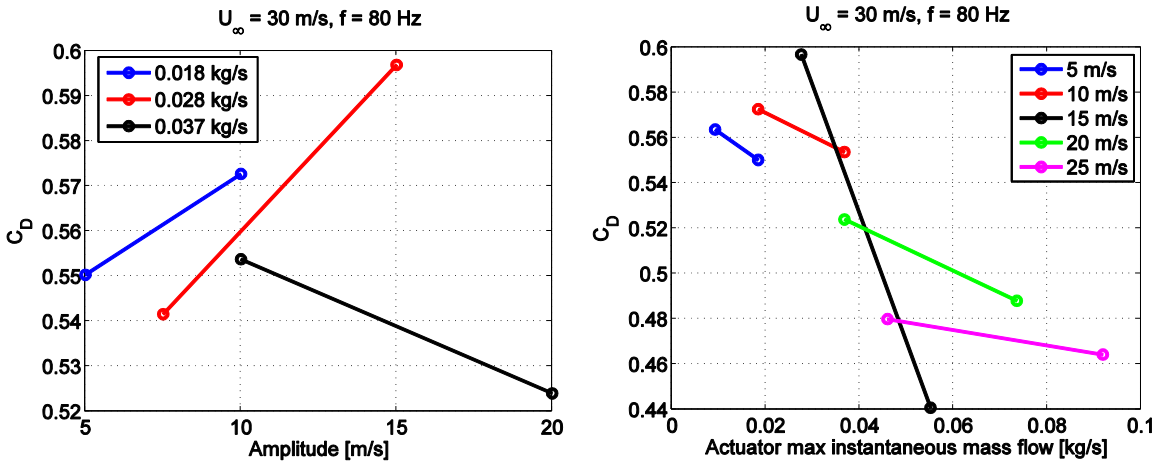

Figure 36. Drag coefficients when varying one variable of velocity and mass flow through the slot.

Three different mass flows were tested for varying amplitudes; two showed an increase in drag when increasing the amplitude and one showed a decrease. In comparison, when keeping the amplitude constant and increasing the mass flow by using a wider slot, the drag coefficients were strictly decreasing with increasing mass flow. It is therefore likely that the improved results that come with increased actuator amplitude is a result of increased mass flow rather than increased slot velocity.

5.5 Analysis of the optimum case

5.5.1 Frequency spectra

The standout case is the forcing at 60 Hz, when something significant changes in the flow field. A frequency analysis shows that the entire shedding frequency spike is eliminated by the flow control system, and the only remaining spectrum is at the forcing frequency along with its corresponding harmonics (**Figure 37**).

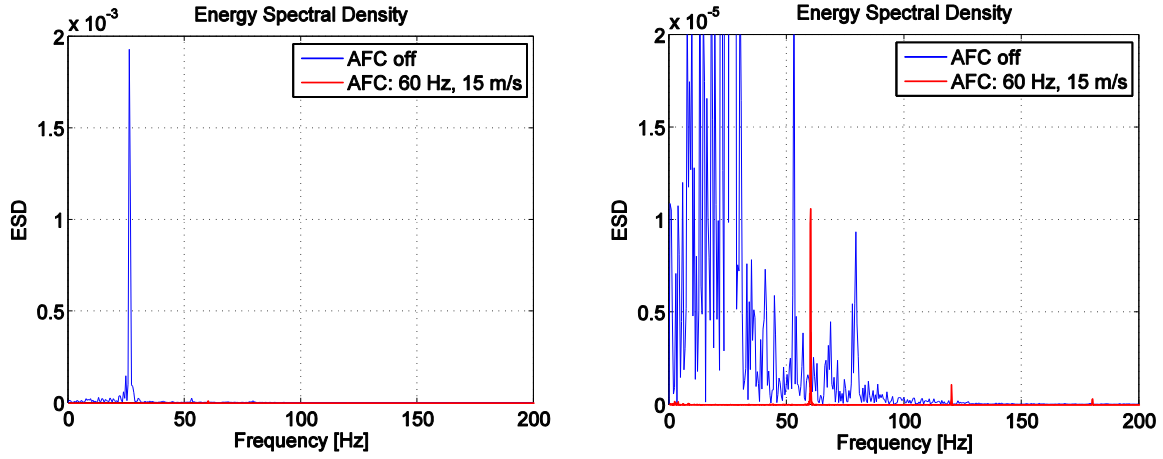

Figure 37. Left: ESD of the 60 Hz time-plot; Right: close-up to be able to see the frequency spectrum with AFC on.

5.5.2 Flow field

A vector plot of the mean flow field without AFC shows the physics of the flow in detail. There are two main counter-rotating vortices developed at the rear; one with air from below the vehicle and one with air from above it. The vortices develop local velocities of 15-20 m/s. Over most of the backlight there is a region of reversed flow at low velocities.

In comparison, there is only one large vortex at the rear of the vehicle when using optimal actuator settings. The oscillatory forcing of the flow completely attenuates the lower vortex, which is the main contributor to the total drag. Instead of a large region of reversed flow over the backlight, there is a smaller separation bubble covering the downstream part. The remaining vortex, which originates from above the vehicle contains much lower velocities, and therefore less energy, than without AFC. Another important difference is that the mean velocity of the air passing between the bottom of the vehicle and the ground is close to the freestream velocity with AFC on, while it is being accelerated considerably without it.

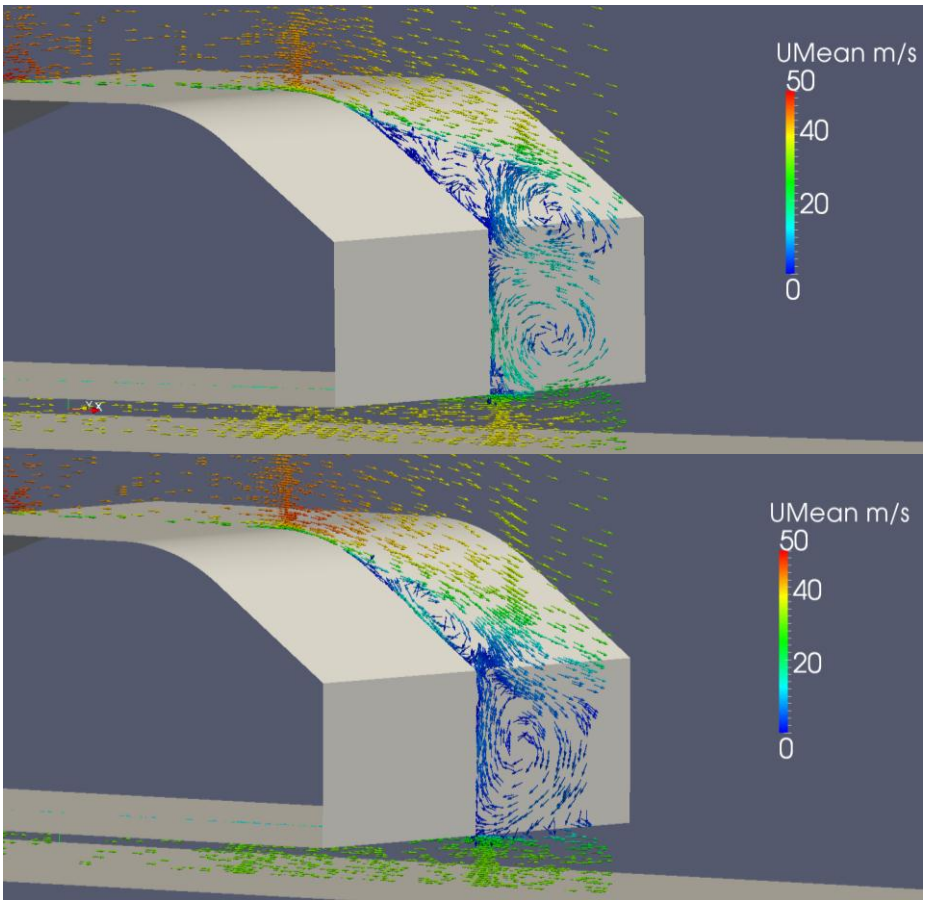

Figure 38. Top: AFC off; Bottom: AFC 60 Hz, 15 m/s

Understanding how the actuator manages to kill the lower vortex is difficult, but may be the key to understanding the physics behind the drag reduction process. What is interesting is that a small slot on the roof manages to alter the entire flow field around the vehicle, all the way to the bottom side in the front of the car. If this process is understood, it could be utilized to measure flow parameters upstream of the actuator in order to enable detailed control of the flow field.

The formation process of the upper and lower vortices is part of a complex interaction between them. Generally, the upper vortex develops first and creates a low pressure behind it when it starts travelling downstream in the wake. This low pressure sucks in air from beneath the vehicle, which is what creates the lower, big vortex. When that vortex in turn is convected downstream, it too leaves a large low pressure-region behind it, triggering further formation of upper vortices. The oscillatory forcing likely alters the top vortex so that there is no low-pressure region that can trigger the formation of the lower vortex. The subject is open for more research, but one has to keep in mind that these effects are considerably amplified by the 2D domain, which has been shown to exaggerate the vortex shedding process.

5.6 Vortex formation process

The following describes the process of how the vortices are built-up and interact with each other when there is no flow control activated:

1) **t = 0.000 s:** The process starts out with an upper vortex which is fairly small, located at the intersection between the backlight and the vertical rear surface.

2) **t = 0.006 s:** The vortex grows by sucking in more air from above the vehicle. As it grows, the vortex core starts moving downwards towards the ground. After a while, the lowest part of the vortex starts interacting with the air from underneath the vehicle, due to viscous effects. This forces the air from underneath the car up between the vortex core and the rear of the vehicle.

3) **t = 0.010 s:** This results in two things. First, the air that enters between the vortex and the car forces the vortex away from the rear wall, so it starts moving downstream in the wake. The second is that a new, small vortex is formed by the upwards moving air coming from underneath.

4) **t = 0.026 s:** As the first vortex travels downstream, the new vortex starts growing by sucking in more air from underneath the car. The new vortex core also moves upwards in a similar way to the first vortex.

5) **t = 0.034 s:** The anti-clockwise spinning vortex launches air into the freestream above the vehicle which deflects it outwards, thus making the size of the wake larger. Eventually, it too starts interacting with the airflow above the car, which starts a similar process to earlier where a new vortex is formed and the old one starts moving downstream.

6) **t = 0.040 s:** After $4/100^{th}$ of a second, the process has completed a cycle and starts all over again.

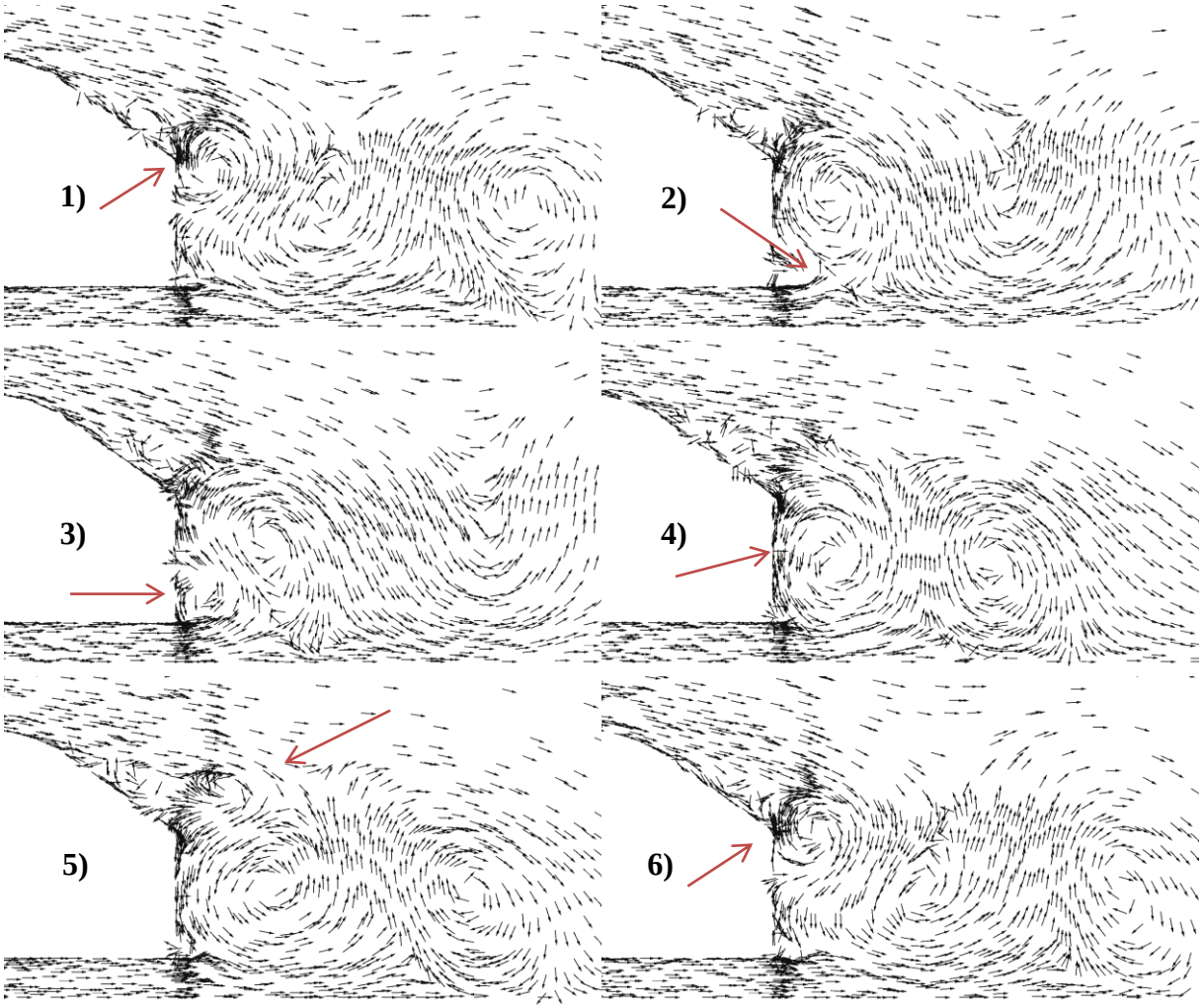

Figure 39. Vortex formation process

Maximum drag occurs at point 5 where the wake is large and there is a lot of energy in the lower, spinning vortex. Minimum drag is at point 2 when the upper vortex moves downwards, which contracts the wake.

6 RESULTS – SEMI-3D

6.1 Mesh

The mesh of the semi-3D cases is almost identical to the 2D mesh, except it has been slightly coarsened and instead of one cell along the width of the car, now 20 cells are being used. This gives a considerably higher computational load, because for each added layer the mesh size is increased by an amount equal to the size of the 2D mesh. Due to the coarsening, the semi-3D mesh is about 13 times bigger than the 2D mesh (instead of 20 times bigger).

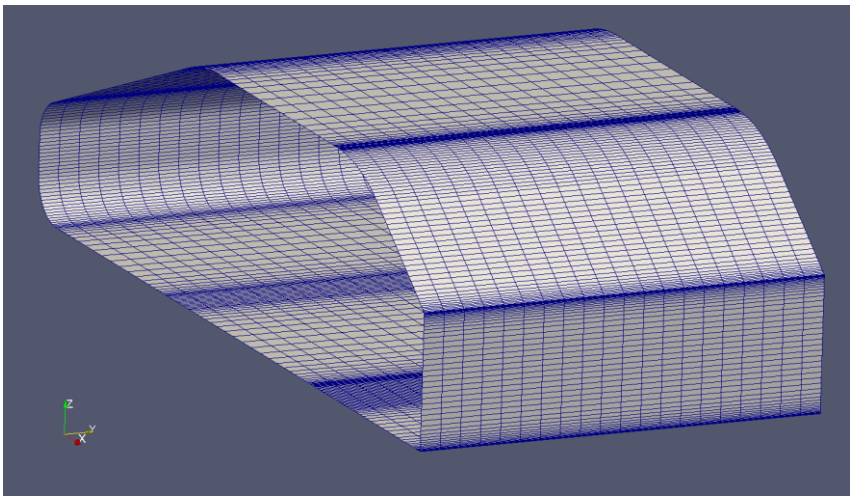

Figure 40. View of the semi-3D mesh of the Windsor model.

The mesh parameters of the semi-3D mesh are shown in **Table 12**:

Cells	668480
Windsor surface faces	6640
Max aspect ratio	563
Non-orthogonality, average	9.4°
Distance: wall – first cell	~ 0.2 mm (y^+ *10-25*)
Cell growth ratio	$\leq$ 1.2

Table 12. Semi-3D mesh info

6.2 Setup

The semi-3D simulations are done with the same settings as for 2D. The difference is that a cyclic boundary condition is imposed on the sides of the computational domain. The effect is that the width of the vehicle is extended to infinity. 3D flow patterns can develop, but there is still no airflow on the sides of the model.

In semi-3D, it is possible to investigate the effect of segmented slots that do not cover the entire width of the vehicle. The slot patterns that have been tested are shown in Figure 41. Each slot is of the same dimensions: 3 mm x 100 mm. Due to cyclic boundary conditions, the slot pattern is repeated to infinity in the simulations.

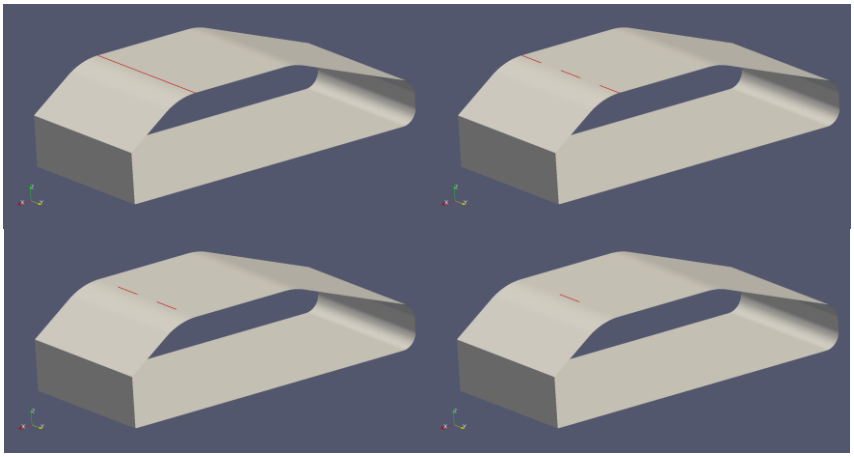

Figure 41. Top left: slots 1,2,3,4,5; Top right: slots 1,3,5; Bottom left: slots 2,4; Bottom right: slot 3

6.3 Reference case

6.3.1 Drag coefficient

The reference case (AFC off) is started from a converged RANS solution. To let the initial transients die out, the actuator is activated after 0.4 seconds (t^*=11.5). The drag coefficients are then averaged and compared from 0.6 seconds (t^*=17.2), so that new transients from the actuator are reduced. The averaging is done to the end of the simulation.

Figure 42 shows C_D as a function of time without the use of flow control. The running average shows a slight drift during the time simulated, which corresponds to 1.54 seconds real time. Spalart highlighted examples of similar phenomena in (20), where he explained it as a possible consequence of residual variations due to finite time samples. The time period is large enough to allow for a fluid particle to travel through the whole domain more than four times. Once again, it is hoped that the errors are similar with AFC activated so that a meaningful comparison can be done. The drag drift phenomenon should be researched further in the future, to pinpoint the exact causes.

The mean drag coefficient is more reasonable than in 2D, with values around 0.4. It is still a bit overestimated, but still much more reasonable than in 2D. This is because, contrary to before, the LES mode can capture realistic, three-dimensional turbulent structures. This reduces the magnitude of the aerodynamic forces. The RANS solution has a C_D of 0.334, which is nearly identical to the 2D case. The difference to the detached-eddy simulation is about 15 %.

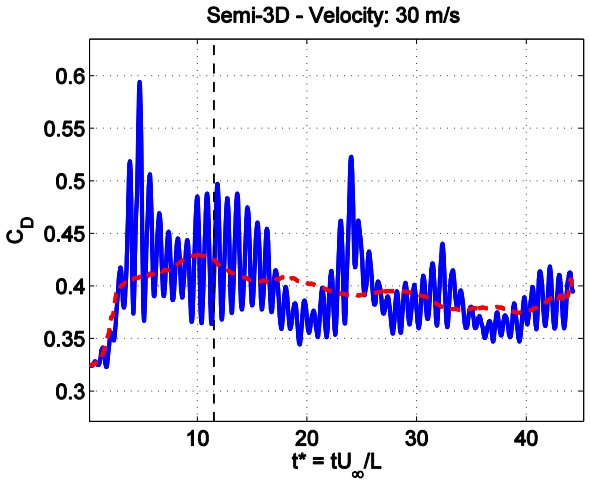

Figure 42. Semi-3D simulation with AFC off. The red curve illustrates a running average of 14.3 time units. The actuators are started at the dashed line.

6.3.2 Frequency analysis

Performing an FFT on the time signal in **Figure 42** yields the frequency spectrum in **Figure 43**. Compared to 2D, it no longer consists of only one peak that contains all the energy. Instead, there are three peaks: one of which is the shedding frequency and two low-frequency ones that capture the longer oscillations seen in the time signal. The vortex shedding frequency is higher than before, at 35 Hz.

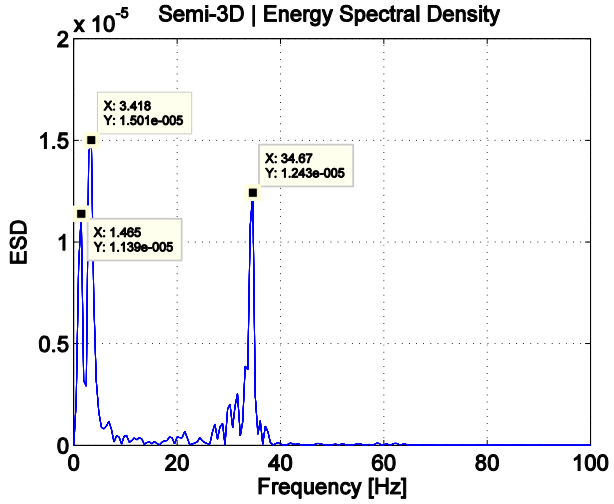

Figure 43. Spectral analysis shows three distinct peaks.

The energy spectral density-plot shows the frequency content accumulated over the whole simulation period. But the drag coefficient undergoes significant changes over time, so it is interesting to see what is happening when the drag coefficient is high and low respectively. After the initial transient, there is a significant peak at 25 time units, and another smaller peak at about 32 units.

A spectrogram of the time signal shows the frequency content at each time instant. It is constructed by applying Hamming windows over the sampled time signal. The windows are 192 samples wide with an overlap of 190 samples (compared to the total amount of 1540 samples). Increasing the window size increases frequency resolution at the cost of only being able to see a shorter time history, while an increase in overlap increases time resolution. The spectrogram of **Figure 42** is seen in **Figure 44**:

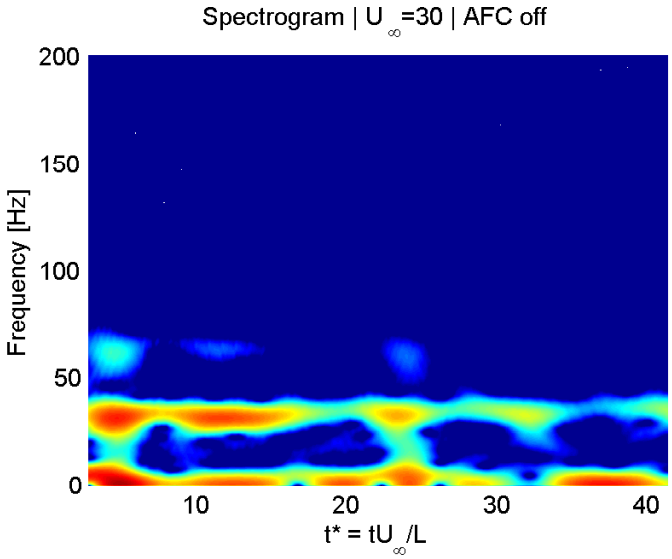

Figure 44. Frequency spectrum over time for reference case.

Two main bands of energy can be seen, corresponding to the peaks found in Figure 43. At some time instants, there is some energy also at around 60 Hz. The energy at low frequencies does not vary much over time while the shedding frequency at 35 Hz does vary fairly significantly. At 25 and 32 time units when there is an increase in the drag, the energy at the shedding frequency is higher than otherwise. At 38 time units there is a noticeable decrease in the shedding energy, which correlates to the lowest drag in the whole simulation. The implication is that the drag (as in 2D) seems to be closely correlated to the strength of the shedding vortices.

6.4 Flow control results

6.4.1 Continuous slot

The first case covers the optimum 2D case: a frequency of 60 Hz and 15 m/s in amplitude. In 2D, this actuation yielded a drag reduction of over 50 %. **Figure 45** shows that there is a major difference in semi-3D, with an almost 40 % increase in drag. The actuator fails to suppress the shedding vortices, instead amplifying frequencies throughout the whole spectrum.

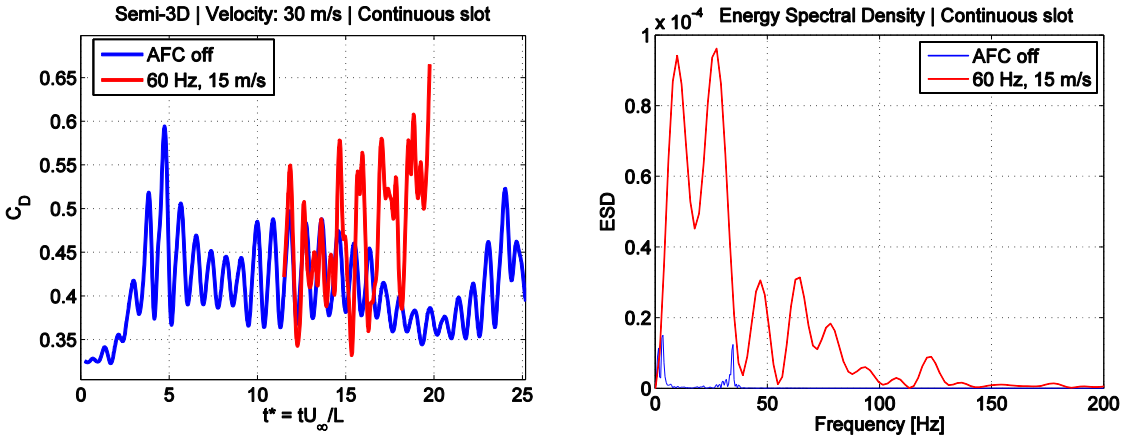

Figure 45. Comparison of C_D between reference case and continuous slot.

The reason for this discrepancy between 2D and semi-3D is likely that once 3D flow structures can develop, it becomes much harder to attenuate the whole vortex by using two-dimensional slot actuation. Other slot patterns need to be investigated to see if the results can be improved.

Slots 1,2,3,4,5	60 Hz	$\Delta\overline{C_D}$
AFC off	0.374	--
15 m/s	0.518	+38.5 %
15 m/s (slots 2,4 phase-shifted)	0.420	+12.3 %

Table 13. Summary of average C_D with continuous slot.

6.4.2 Segmented slots

A few different slot patterns – as shown in **Figure 41** – were tried under different circumstances in order to get a general feel for how it affected results. Keeping in mind that the pattern is duplicated through the cyclic boundaries, the difference between having one, two or three active slots has to do with how large part of the total width of the vehicle that is covered.

Slots 1, 3 and 5 are run at various frequencies in **Figure 46**. A few observations can be made from these results. A segmented slot pattern gives considerably better results than the continuous slot, with a slight reduction in drag. Furthermore, the results seem to be improving with higher frequencies (**Figure 47**). Compared to 2D, no frequency manages to achieve similar drag reductions. Also, in semi-3D, a wider range of frequencies is more or less equally effective, which is in contrast to the 2D case.

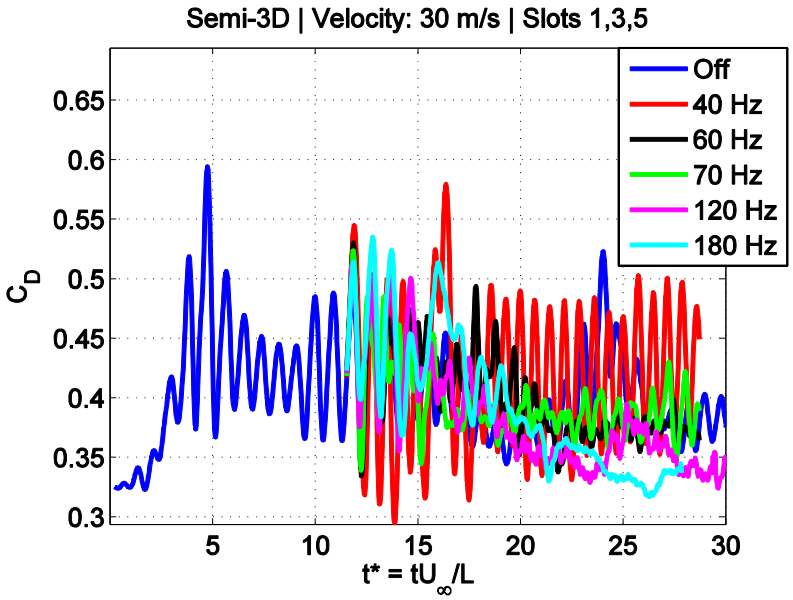

Figure 46. Slots 1,3,5 active at different frequencies.

The most effective frequency is 180 Hz, which manages to get a 7.9 % decrease in drag over the averaging period. This reduction is however still fairly small and the drag too fluctuating to be able to draw any definitive conclusions for such a relatively short simulation time. It is clear however that the magnitudes of drag reduction achieved in 2D cannot be anywhere near replicated in more realistic simulations.

Slots 1,3,5	40 Hz	60 Hz	70 Hz	120 Hz	180 Hz
AFC off	0.392	0.392	0.392	0.392	0.392
15 m/s	0.418	0.386	0.385	0.362	0.361
ΔC_D	+6.6 %	-1.5 %	-1.8 %	-7.7 %	-7.9 %

Table 14. Mean drag coefficients, $t^*_{end} = 29$

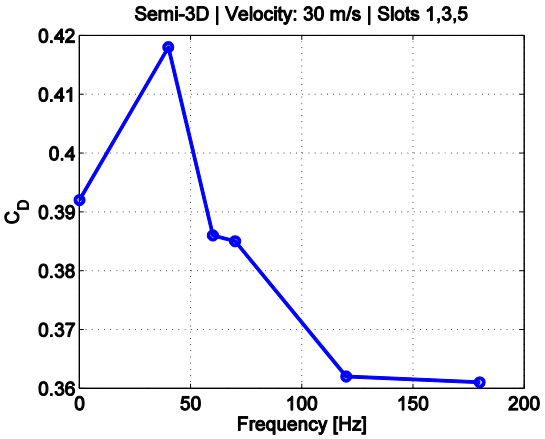

Figure 47. Influence of actuator frequency in semi-3D.

6.4.3 Altered slot position

Since the slots should be located as close as possible to the average separation line, a new slot position closer to the separation was tried in order to test if results can be improved. The new slots are located exactly mid-curvature, as shown in **Figure 48**:

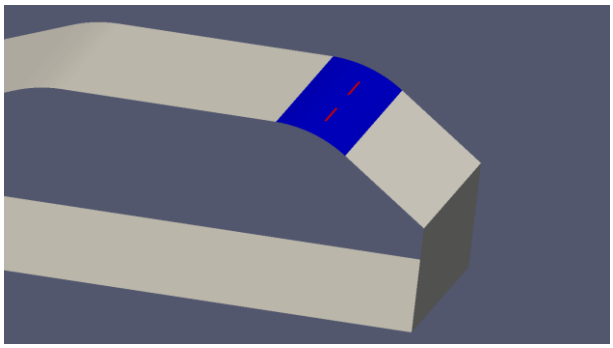

Figure 48. Positioning of curvature slots (red).

As the model is adjusted, the mesh must be modified accordingly to have enough detail in the vicinity of the slots. Therefore, a new reference case must be calculated, using the new mesh. The rest of the parameters are the same as before. Figure 49 shows the difference between the model with the roof slots and the new model with "curvature slots".

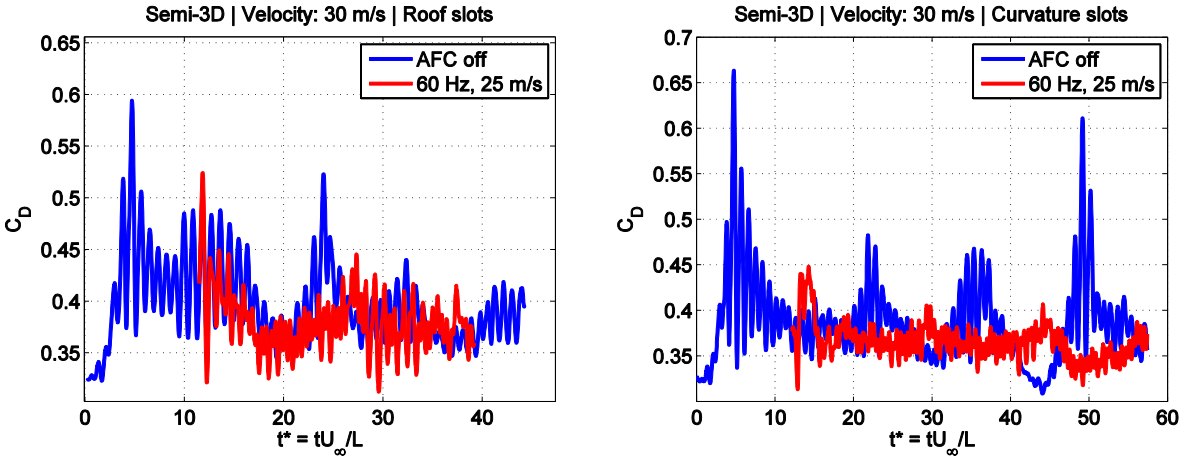

Figure 49. Left: Drag trace with roof-mounted slots; Right: Drag trace with curvature-mounted slots

It can be seen that the solution changes also with AFC off, which gives an indication of the mesh sensitivity; the geometry is identical to before – only the mesh has changed. The new mesh gives a mean drag coefficient that is 1 % lower than the old mesh. For both cases, the drag force is steadier with flow control and the highest peaks of the reference cases are eliminated.

Looking at the frequency spectra in Figure 50, one can see that the curvature slots are more effective by eliminating all the energy at the shedding frequencies. The slots on the trailing edge of the roof dampen the shedding intensity, but some energy still remains. Instead, new peaks are created at the actuator frequency of 60 Hz, which is to be expected. In the end, the AFC system has shifted energy from the natural shedding frequency to the actuator frequency. It is not trivial to predict whether this change will be beneficial or not for reducing total drag.

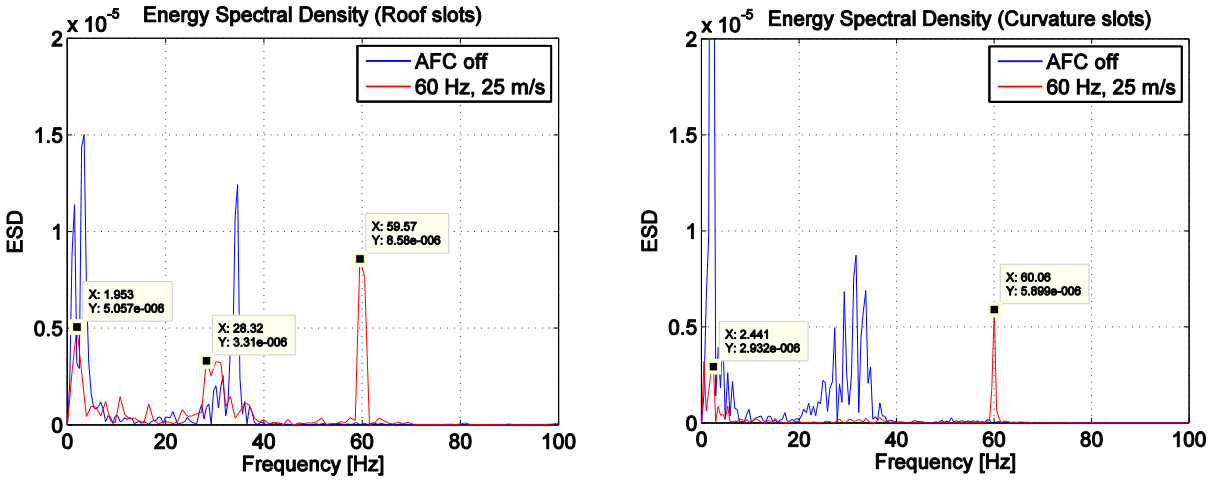

Figure 50. ESD of roof slots (left) and curvature slots (right).

Table 15 gives a summary of the mean drag coefficients for the two cases. The curvature slots perform slightly better than its roof-mounted counterparts, which is in line with what is expected. The difference is however not overwhelming.

Slot position	$\overline{C_D}$ (AFC off)	$\overline{C_D}$ (AFC on)	ΔC_D
Roof	0.385	0.373	-3.1 %
Curvature	0.381	0.362	-5.0 %

Table 15. Comparison of average drag for two slot positions.

6.5 Flow field

6.5.1 Wake

The characteristics of the flow field is perhaps more interesting to study in semi-3D as the results are physically more correct. Without any oscillatory forcing of the flow, the main structures in the wake are the large vortices that are being periodically shed from the upper and lower sides of the Windsor model – as so clearly seen in the 2D analysis. Even though some three-dimensional behavior has appeared, the vortices are still relatively homogenous in the spanwise direction. **Figure 51** shows an instantaneous flow pattern visualized with an iso-surface of the vorticity magnitude: $|\boldsymbol{\omega}| = 10000$. The upper vortex has started moving downstream as the new lower vortex has just started developing.

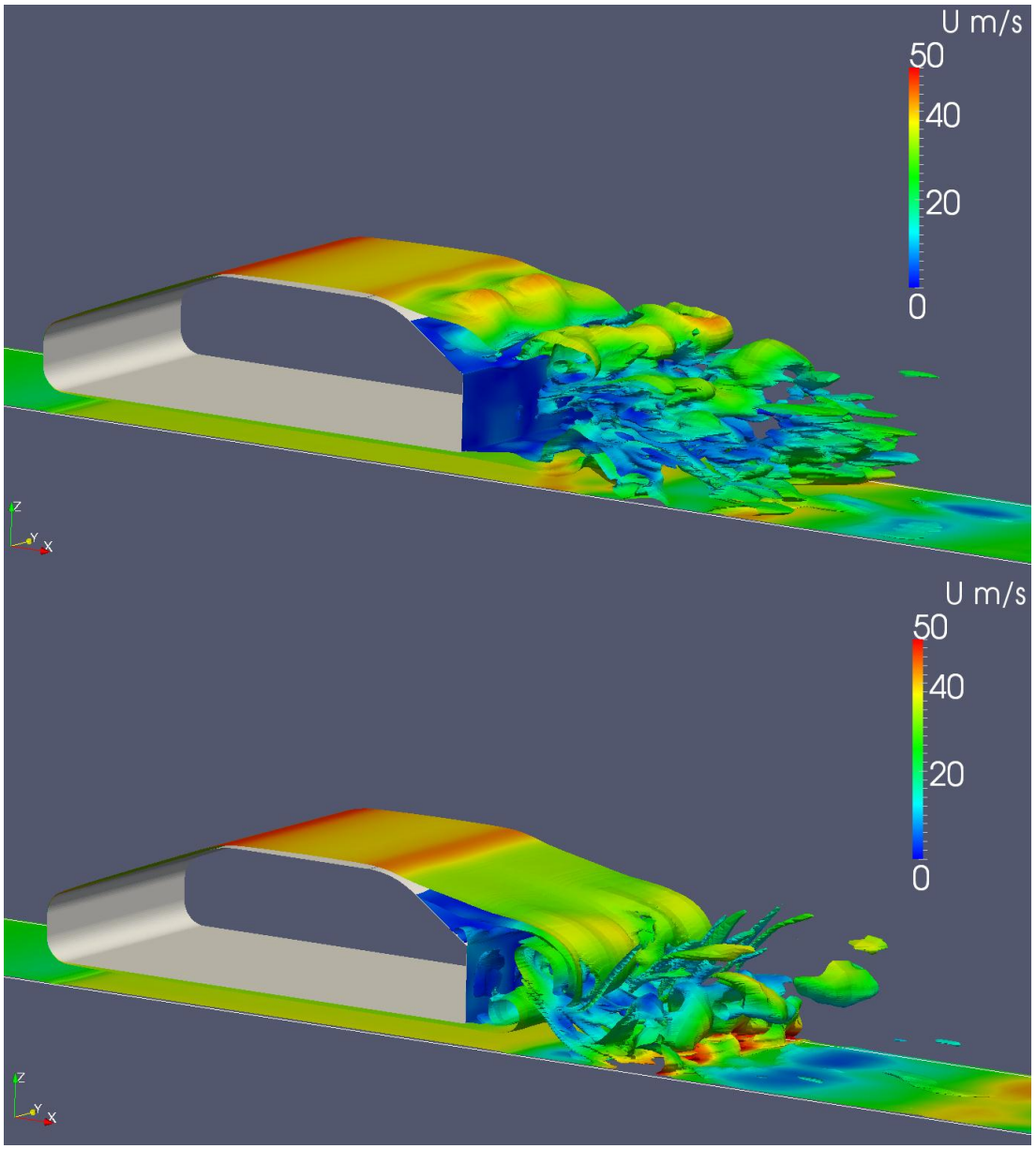

Figure 51. Wake structure visualized with $|\boldsymbol{\omega}| = 10000$. Top: Slots 2 & 4 active; Bottom: AFC off

The wake is with slots 2 and 4 activated very different. The homogenous spanwise behavior is completely broken up by the oscillating airflow from the actuators, which results in a more chaotic wake structure. Two clear "bubbles" of air are seen above the backlight, which are the result of blowing from the slots. The reason why a continuous slot fails to reduce drag while a segmented slot pattern does not is found here. Because a main part of the drag comes from the existence of large vortices, it is reduced when their spanwise homogeneity is broken up. A continuous slot risks increasing the strength of the vortices instead of destroying them, which would increase drag.

6.6 DDES performance

To check whether the DDES model works well together with the mesh, the subgrid-scale viscosity is monitored in **Figure 52**. A large ν_{SGS} shows that there is a lot of energy in eddies with a scale smaller than the grid cells, which may indicate that a mesh refinement in those areas could give improved results.

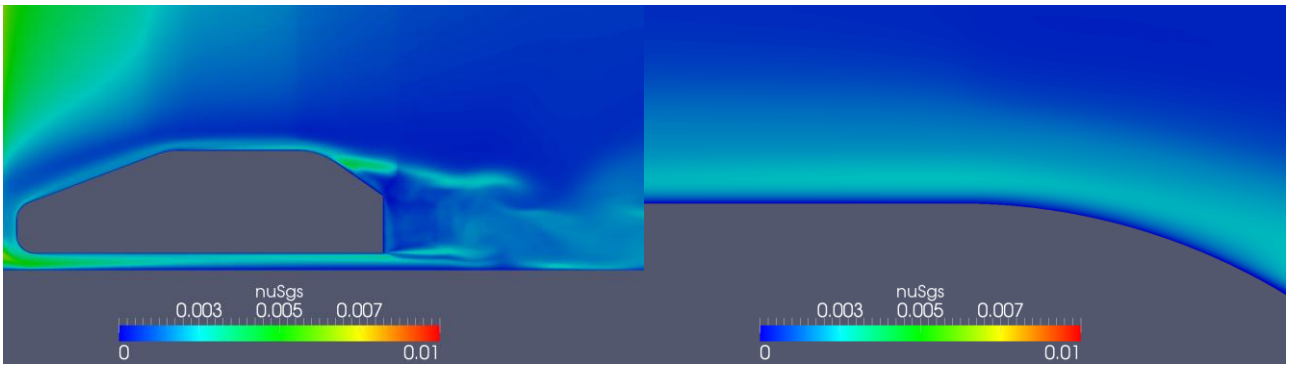

Figure 52. Left: ν_{SGS} around model; Right: ν_{SGS} in the boundary layer

As seen in the figure, there are some areas with higher subgrid-scale viscosity than in other areas, but there are no extremes anywhere around the vehicle. The DES limiter seems to be working properly as there is virtually no LES content close to the wall – an indication that RANS mode is activated in that area. An area of future research could be a mesh refinement study to investigate how much the subgrid-scale viscosity changes for a certain refinement. Unfortunately there was no time for such a study during this thesis project.

7 RESULTS – 3D

7.1 Mesh

The mesh in 3D is more complex than previously due to the full domain being modeled. This increases the computational demands, as well as makes it more challenging to perform a successful blocking of the model. The Windsor model mesh is shown in **Figure 53**, and the mesh parameters in **Table 16**. All mesh parameters are kept as similar as possible to previous cases, in order to minimize the differences in discretization errors for the different meshes.

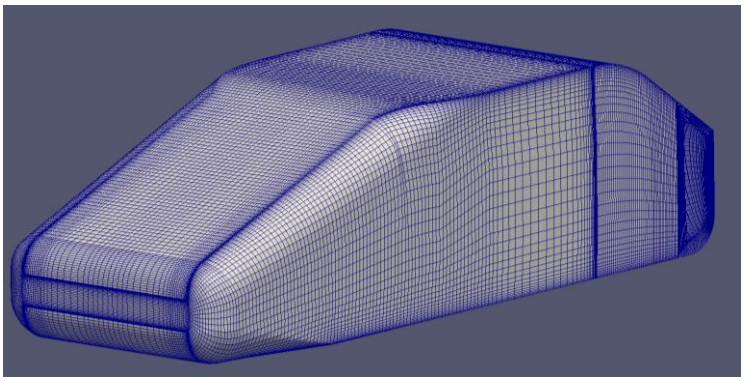

Figure 53. 3D mesh of Windsor model.

Cells	2,967,256
Windsor surface faces	43702
Max aspect ratio	1422
Non-orthogonality, average	20.6°
Distance: wall – first cell	~ 0.2 mm (y^+ *10-20*)
Cell growth ratio	$\leq$ 1.2

Table 16. 3D mesh info

7.2 Test setup

Due to the long computational time in 3D, only two cases are simulated: one without active flow control, and one case with slots 1, 3 and 5 running with a frequency of 60 Hz and amplitude of 25 m/s. Also, contrary to earlier cases, the DDES runs are started from zero instead of from a converged RANS solution.

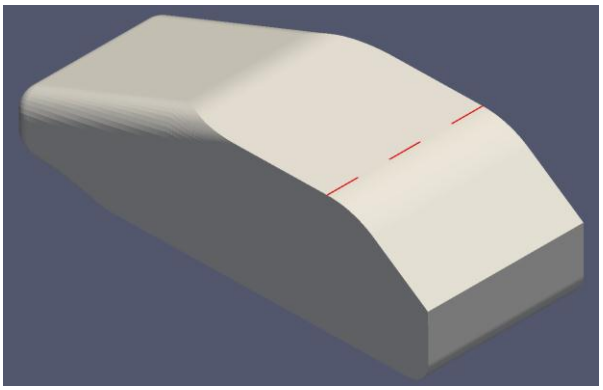

Figure 54. Slots used in 3D simulations.

7.3 Results

7.3.1 Drag and lift history with/without AFC

In full 3D most of the effects that exist in a real flow field around a car is modeled, with the most important addition being the flow along the sides of the model. This airflow will interact with the vortices shed from above and below the car. The air coming from the sides can also have its unique shedding frequency, with alternating vortices coming from the left and right sides. The drag and lift coefficients as a function of time is depicted in **Figure 55**.

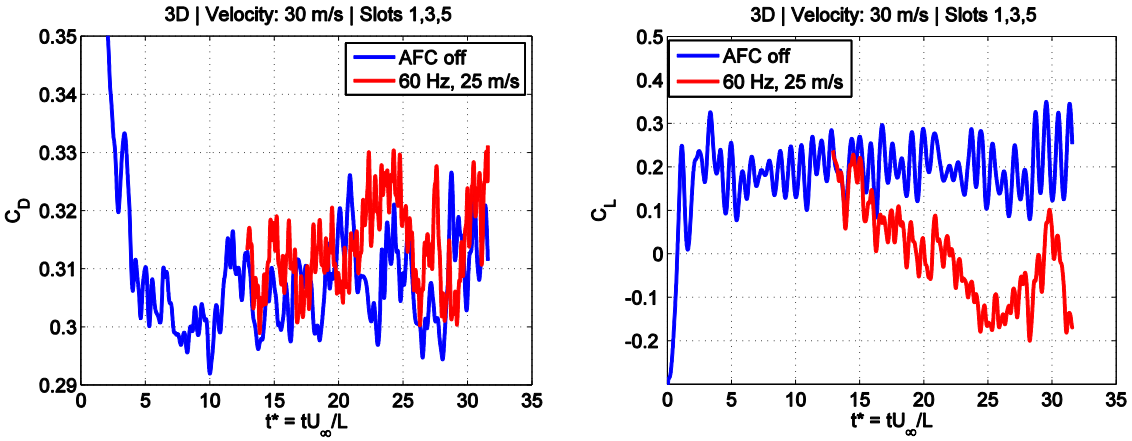

Figure 55. Comparison of AFC on/off – Left: C_D; Right: C_L

The magnitude of the drag coefficient is 20 % lower than in semi-3D. This seems correct because of further reduced intensity of the shedding processes in full 3D. This has the implication that the AFC system, which mainly affects the vortex shedding in its current implementation, will see reduced effectiveness. For the tested case, it increases the total drag by 2 %, which is a too small difference to draw any definitive conclusions.

It is apparent however, that the flow field is somehow affected by the actuators. This is easiest seen in the lift coefficient plot, which is negative when using AFC. This could open up a new

area for investigation: using active flow control to create downforce to improve handling in vehicles, in addition to possibly reducing drag. Table 17 shows the average lift and drag coefficients of the tested case:

Slots 1,3,5	$\overline{C_D}$	$\overline{C_L}$
AFC off	0.309	0.196
60 Hz, 25 m/s	0.315	-0.004
Δ	0.006 (+1.9 %)	-0.200

Table 17. Change in mean lift and drag with active flow control.

7.3.2 Frequency domain

Looking at the frequency domain, it is revealed that AFC dampens the higher frequency peaks that correspond to the shedding frequencies, but fails to take care of the lower frequencies below 10 Hz. Also, as before, new peaks are introduced at the actuation frequency and its harmonics.

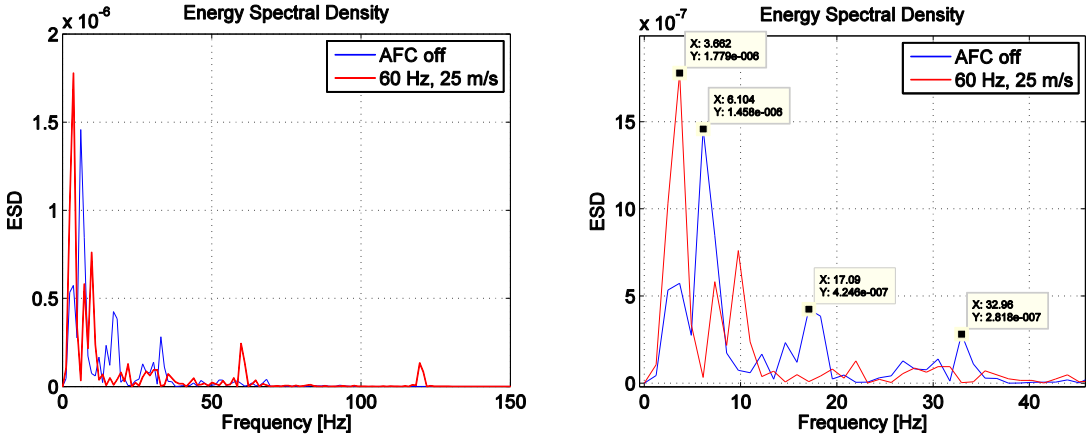

Figure 56. Comparison of ESDs of C_D with AFC off/on. Close-up of the lower frequencies on the right.

7.4 Instantaneous flow field

7.4.1 Pressure

Since the aerodynamic forces on the vehicle are directly dependent on the pressure field, understanding it is key to understanding the fundamental processes. In **Figure 57** the last 0.03 seconds of the simulation is plotted. During the first time instance, the actuator is in its suction phase, during the second it is blowing and in the last time instance the velocity through the slots is low. Without AFC, the pressure field is almost symmetrical, except at the lower, vertical wall. The higher-pressure region is oscillating slightly from side to side, due the shedding vortices from the sides. The pressure with AFC turned on is more chaotic and is also changing more over time.

One main observation from the figure is that one cause for the reduction in lift with flow control is that the low-pressure region over the curvature is almost entirely eliminated. Overall, the base pressure is a little higher in the reference case, which results in the 2 % lower drag coefficient.

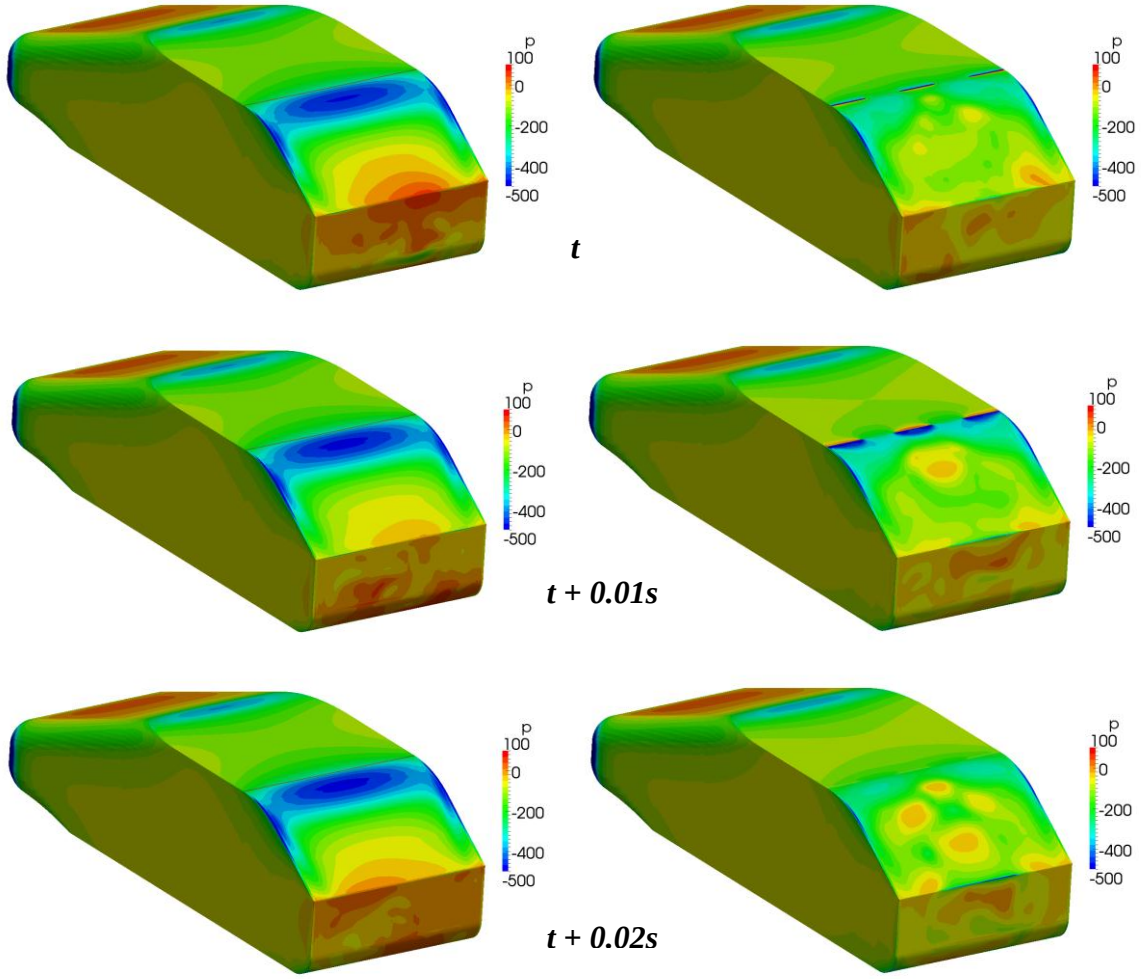

Figure 57. Instantaneous pressure fields for AFC off (left), and AFC on (right).

7.4.2 Wake structure

Figure 58 shows the dominant vortices in the wake of the car, visualized by the ***Q***-criterion, which is the second invariant of the rate-of-strain tensor.

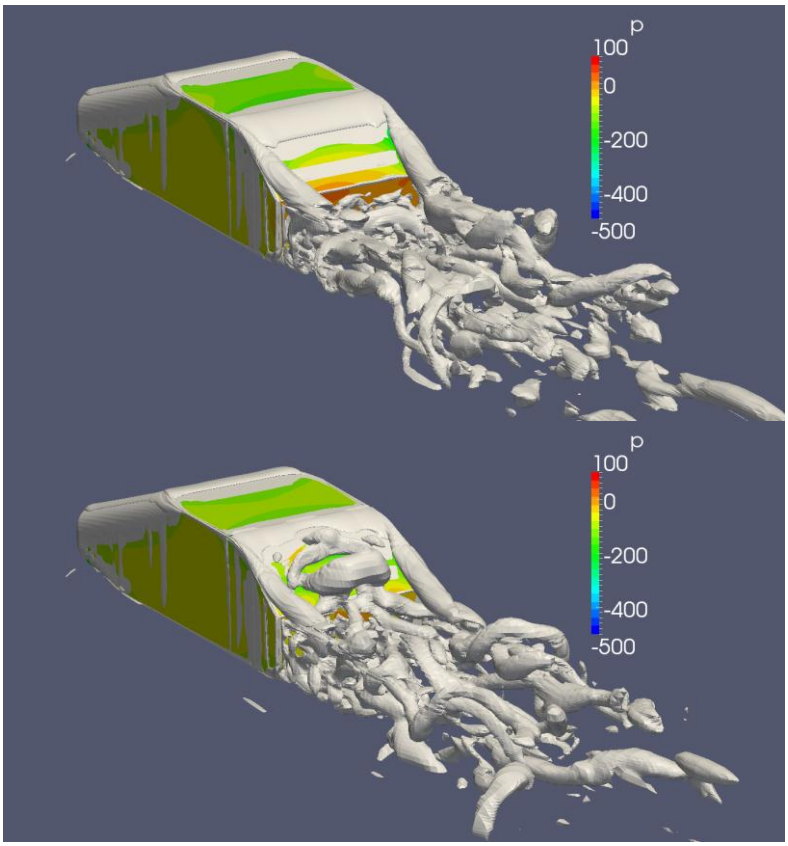

Figure 58. Vortical structures visualized by $\boldsymbol{Q} = 20000$. Top: AFC off; Bottom: Slots 1,3,5 activated

One significant difference to 2D and semi-3D is highlighted here. In 3D, there are two large longitudinal vortices rolling up from the side of the car over the "C-pillar". These contain a lot of energy and can contribute to a significant part of the total drag. The rear-window in this case behaves like a delta wing at high angles of attack, which creates two very similar vortices that create suction (and therefore lift) over the wing. In a car, this suction will mainly contribute to drag instead of lift, why certain angles of the rear window should be avoided when designing a car. Similar to delta wings, when the inclination becomes large enough, the vortices will break down and the rear window "stalls", which can give a substantial decrease in total drag. But an inclined rear of the car also serves to decrease the base area, which is beneficial for reducing drag, so the rear design should be a compromise between these aspects.

One strategy when designing an AFC system could thus be to specifically target these longitudinal vortices with oscillatory forcing from slots in for example the C-pillar. This way it may be possible to use a larger backlight angle without the negative effects of the longitudinal vortices.

Another interesting observation is that there are a lot of vortices created over the middle of the backlight by the AFC system. It is likely that these structures contribute to the lower base pressure seen in **Figure 57**. A detailed picture of this area is shown in **Figure 59**, where a

small bubble is seen around the slots followed by a small region of less vorticity immediately downstream. The large vortices in the middle of the backlight start forming around mid-curvature, possibly triggered by the middle slot somehow. Perhaps it would be better to deactivate slot number 3 to avoid the creation of these vortices. That is however the topic of future studies.

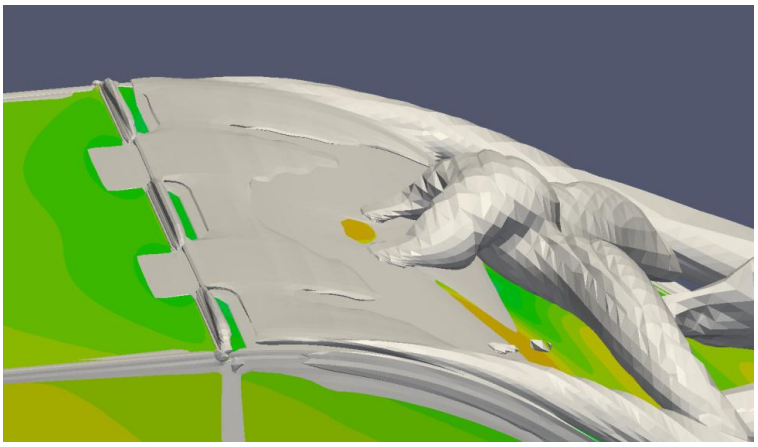

Figure 59. Detailed view of flow structures around the slots. $\boldsymbol{Q} = 10^6$.

7.5 Mean flow field

The mean fields are averaged over the same period as the force coefficients: from $t^* \approx 17$ (= 0.6 s) to the end of the simulations.

7.5.1 Velocity

The velocity fields in two planes are compared in **Figure 60**. The wake is slightly larger with AFC on, as can be seen especially over the backlight. In the top view the wakes look very similar, but with a larger area behind the vehicle with very low local velocities. Overall the differences between the two cases are fairly small, and the local velocities are lower than in semi-3D, which corresponds well with the lower forces.

A look at the streamlines around the vehicle (**Figure 61**) does not reveal anything surprising, but it is noted that the mean pressure field in the front parts of the model is almost identical. The origin of the longitudinal vortices is seen to be air coming from the sides and then being deflected up over the edge towards the lower pressure region at the top of the backlight.

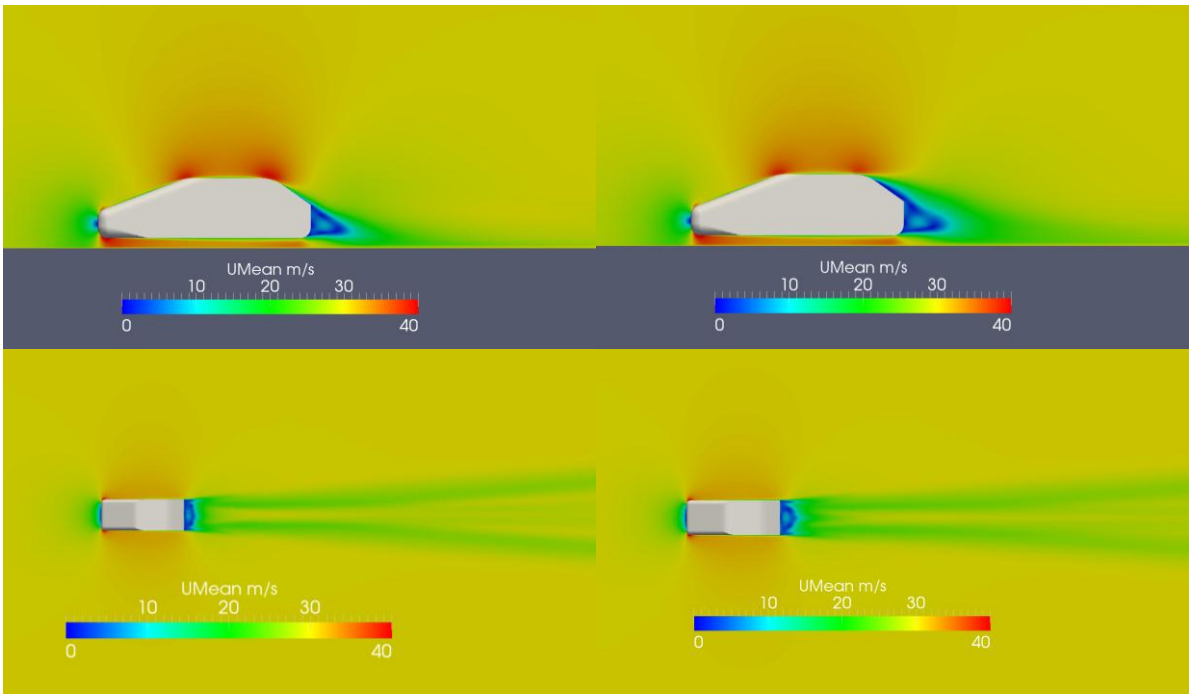

Figure 60. Mean velocity fields. AFC off (left) & AFC on (right)

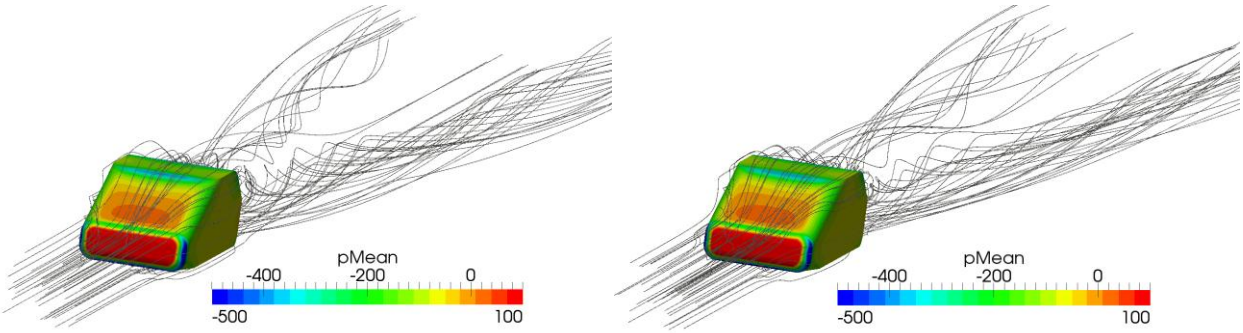

Figure 61. Mean velocity streamlines.

7.5.2 Pressure

Mean pressures give a good indication of the overall behavior of the airflow, and what areas contribute the most to mean drag. The comparison in **Figure 62** confirms what has been shown earlier, that the low-pressure area is significantly reduced with AFC and that the overall base pressure is higher without it. The pressure fluctuations $\overline{p'}^2$ are plotted in **Figure 63**, where it is seen that the pressure fluctuates much more over the backlight with AFC than without it. Naturally, this is an effect of the oscillating forcing of the flow just upstream. The lower rear end shows approximately equal pressure fluctuations.

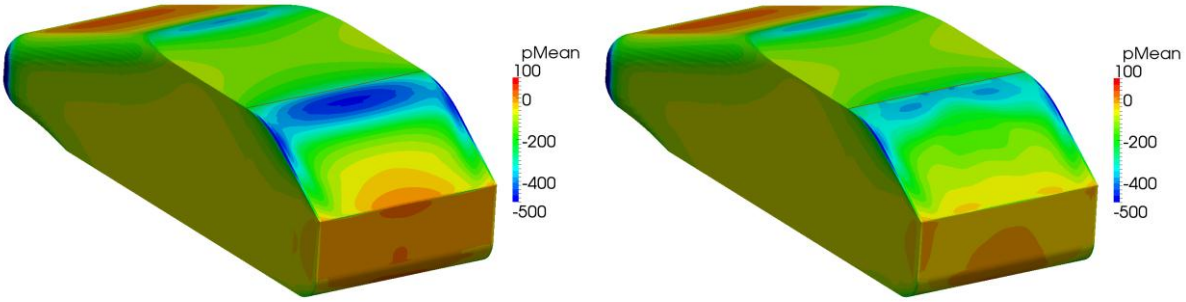

Figure 62. Comparison of mean pressure fields. Left: AFC off; Right: AFC on

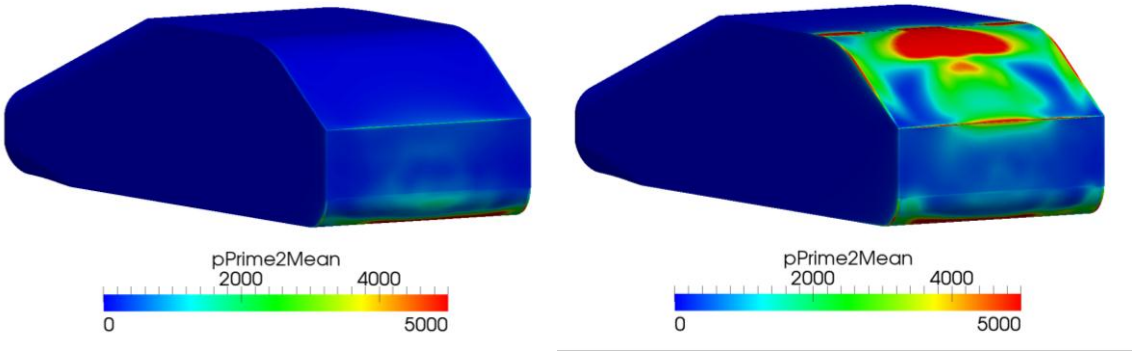

Figure 63. Comparison of fluctuating pressure magnitude. Left: AFC off; Right: AFC on

Finally, a detailed view of the wake pressure in a plane coinciding with the rear end of the vehicle is shown in **Figure 64**. It gives a good view over the main sources of drag in the wake. In the reference case, the two longitudinal vortices seem to be dominating. They are marginally weakened by the actuator (seen as a less intense low pressure in the vortex cores), but this gain is contradicted by the lower pressure over the middle part of the rear structure. The system at least shows some potential, and with further tuning of the slot layout and the input signal there is a real chance that an improvement could be achieved.

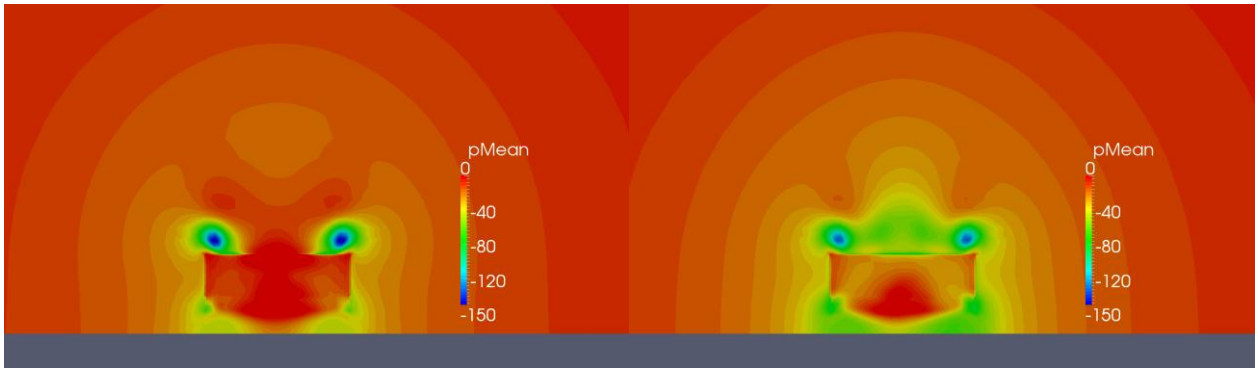

Figure 64. Wake pressures seen from the rear of the vehicle.

8 SOME THOUGHTS ON ADAPTIVE CONTROL

As mentioned in the Introduction, an active flow control system that cannot in some way adjust to the circumstances is of rather limited practical use. As have been seen in the CFD runs, optimal settings differ depending on driving conditions such as freestream velocity. The task of a control system will be to keep the system operating within an optimal range during changing conditions, and/or to control the actuators with impulses which target specific flow structures that have been measured upstream of the actuator slots.

Since the general flow field behaves in a nonlinear way, one must identify significant variables that show linear relationships to each other (at least within some range) to be able to employ standard linear control theory. If this is not possible, the nonlinearities must be compensated for with nonlinear control methods.

8.1 Control approaches

8.1.1 System modeling

The flow control system can be modeled using “black-box”-theory as in the closed-loop system in **Figure 65**:

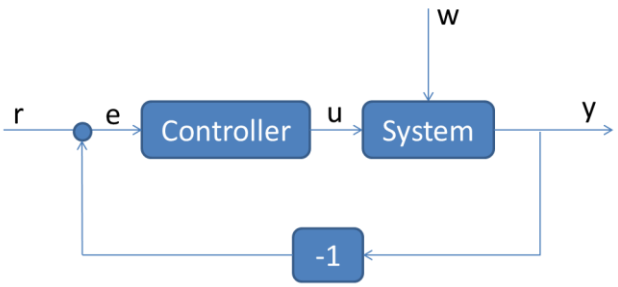

Figure 65. General closed-loop system

The variable *r* is the set point, *e* the error between the output and the set point, *u* the control signal, *w* an external disturbance affecting the system and *y* is the output from the system. The challenge is to determine what properties of the real system should be associated with which of these variables, i.e. what properties of the flow are important for the aerodynamic forces and how are they to be controlled? There are two main paths that can be followed when trying to solve this problem: classic control theory and fuzzy logic control.

8.1.2 Classic control

Since the fluid motion cannot be modeled with analytical functions, standard transfer functions or state-space models cannot be mathematically derived. Instead, one can try to find linear relationships for certain variables and develop transfer functions between them.

The aerodynamic forces on the vehicle are the result of the pressure distribution around it, which in its case depends on other parameters such as fluid velocity, vorticity and so on. So to target a drag reduction, the surface pressure is the end-variable that needs to be affected. To make things easier in the world of simulations, one could first try to control the drag coefficient itself, even though it cannot be directly measured in real life. It can then be noted that there is a fairly linear segment of the C_D-C_μ curve for some of the frequencies in 2D – **Figure 66**:

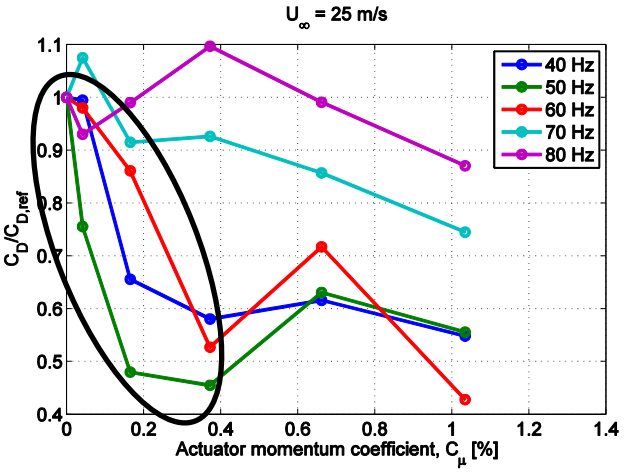

Figure 66. "Linear" area highlighted with black circle.

This local linearity enables the implementation of a standard, linear control system that regulates the momentum coefficient of the actuator to a desired C_D, and that can also compensate for external disturbances such as wind gusts.

8.1.3 Fuzzy logic control (FLC)

There is another main path of control systems that is especially suited to systems that are difficult to model, or which are easier controlled "intuitively". Fuzzy logic introduces a linguistic system description, where statements can have different degrees of truth.

The whole parameter space is first mapped into *fuzzy sets*, which describe the state of the system. If the difference between two variables is regarded as a system state, it can be divided into the fuzzy sets "equal", "small difference" and "big difference" for example. This process is called *fuzzification.* The different sets are defined as, most often, triangular functions ranging between the values 0 and 1. These functions are called *membership functions*. A discrete system parameter value can satisfy several membership functions simultaneously, but to different degrees.

The control of the system is based on a set of linguistic control rules of the type:

IF *statement1* (AND *statement2 ...)* THEN *action.*

A simple rule example could be "IF *big difference* between variables, THEN *increase* motor speed". Actions dictated by the set of rules are then weighed against each other and converted back to a discrete value through a *defuzzification* process.

8.2 Example of FLC algorithm

As the fluid mechanics in external aerodynamics is very complex and hard (or impossible) to model using analytical functions, a fuzzy logic control system could be well suited for such applications.

In the following example it is assumed that an asymmetric flow field – such as crosswind flow – can be compensated for by running different actuators at different amplitudes. This hypothesis is reasonable since the effect of oscillatory forcing has been shown to depend on actuator amplitude, but it has not been confirmed in a CFD simulation. An example of a fuzzy logic algorithm that compensates for crosswinds could then be formulated as follows:

8.2.1 Determining fuzzy sets

Step 1 is to determine the fuzzy sets. A surface of the vehicle can be split longitudinally and the pressure on each half monitored in real-time. The average pressure difference between the two sides, $p_{left} - p_{right}$, could then be calculated and regarded as the state of the system. Fuzzy sets are then constructed according to **Table 18**:

State	Fuzzy set
$\mathbf{20}\ \% < \boldsymbol{p_{left} - p_{right}}$	Big positive (BP)
$\mathbf{0}\ \% < \boldsymbol{p_{left} - p_{right}} < \mathbf{20}\ \%$	Small positive (SP)
$-\mathbf{5}\ \% < \boldsymbol{p_{left} - p_{right}} < \mathbf{5}\ \%$	Essentially zero (EZ)
$-\mathbf{20}\ \% < \boldsymbol{p_{left} - p_{right}} < \mathbf{0}\ \%$	Small negative (SN)
$\boldsymbol{p_{left} - p_{right}} < -\mathbf{20}\ \%$	Big negative (BN)

Table 18. Proposed fuzzy sets for crosswind compensation.

8.2.2 Designing the membership functions

The intervals in **Table 18** overlap slightly to make it possible to build membership functions out of them. These need to sum up to close to 1 for any possible input value. As can be seen in **Figure 67**, an input value (x-axis) can belong to different membership functions simultaneously. For example, an input value of -10 % will be weighted 0.3 "big negative" and 0.7 "small negative" (which sums up to 1). The "big positive" function takes a value of 1 above 20 %, and decreases linearly down to 0 between +20 % and + 5 % (correspondingly for the big negative" function).

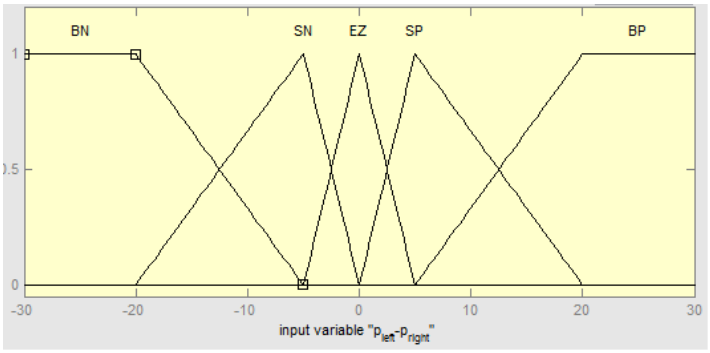

Figure 67. Membership functions for input state.

8.2.3 Constructing control rules

Assuming for example two actuators, one to the left and one to the right of the longitudinal centerline, a suitable set of control rules could be:

	Fuzzy set		Left actuator		Right actuator
IF	Big Positive	**THEN**	-10 m/s	**AND**	+10 m/s
IF	Small Positive	**THEN**	-5 m/s	**AND**	+5 m/s
IF	Essentially Zero	**THEN**	Do nothing	**AND**	Do nothing
IF	Small Negative	**THEN**	+5 m/s	**AND**	-5 m/s
IF	Big Negative	**THEN**	+10 m/s	**AND**	-10 m/s

Table 19. Possible set of control rules for crosswind compensation.

A control signal is then calculated by converting the values of the fuzzy membership functions into a single, unique control output (defuzzification). This can be done in different ways, for example by taking the centroid of the relevant membership functions.

8.3 OpenFOAM implementation

To be able to implement a control system in OpenFOAM, it must be modified so that it can calculate the actuator boundary conditions during run-time. This can be done using the boundary condition *codedFixedValue*, which enables a C++ code-stream to be implemented on-the-go. The code is written in a text file called *codeDict*, which is compiled by the solver ahead of every new time step. The strategy for coding the control system is:

1. Read relevant values from probed locations each time-step.
2. Store the values in a buffer.
3. Implement control algorithm on buffered values.
4. Compute boundary condition for next time step.

During the timeframe of this thesis, a working buffer has been created using this method, but a full control system has not yet been implemented in OpenFOAM.

9 OTHER ASPECTS

9.1 Uncertainties / errors

There are several different potential sources of error in the CFD simulations. These range from spatial and temporal discretization errors due to a limited number of cells in the mesh, and a non-infinitesimal time step respectively. There are also truncation errors arising from the iterative solution of the equations, which can be to some extent controlled by choosing the tolerance levels.

Another major potential uncertainty is the modeling error; in this case the turbulence model and wall functions, which both are designed from empirical knowledge in an effort to make them reasonably accurate for a wide number of conditions. Only a slight error in predicting the correct friction can result in large errors, since a small change in the separation point can give a large change in drag. It is therefore paramount that the chosen turbulence model works well for the considered flow field. A further investigation of different turbulence models is therefore a good topic of further research.

Different runs of identical meshes have given results that are within 1-2 %, a variation resulting from residual errors. A deeper investigation of the discretization errors (mesh size and time step) and modeling errors (trying different turbulence models) has not been performed, but since mainly the delta-values are of interest, this will reduce the sensitivity to systematic errors.

An additional consideration is the feasibility of using RANS to model the boundary layer when modeling active flow control, which is done in DES. RANS per definition uses a time-averaged description of the boundary layer. Since the principle of AFC is to introduce a time-varying velocity component in the boundary layer, a RANS description will no longer be strictly valid. Today, no good alternative methods exist apart from DNS/LES to properly model transient behavior of the boundary layer. Research is currently (2012) ongoing at the Royal Institute of Technology to get an idea of the magnitude of this error, as well as for modifications to the RANS model that can model such transient behavior (29).

9.2 Net reduction of drag

When designing an AFC system one has to always consider the effective, net, reduction in drag. In the results, only the absolute difference in drag has been mentioned, without consideration of the power that is needed to run the actuators. The net difference in drag can be stated as:

$$\Delta C_{D,net} = \Delta C_D \left(1 - \frac{P_{act}}{P_s}\right) \tag{9.1}$$

$$P_s = \Delta C_D \cdot \frac{1}{2} \rho A V^3 \tag{9.2}$$

where P_{act} is the actuator power and P_s is the power saved when using the system. The resulting expression becomes:

$$\Delta C_{D,net} = \Delta C_D - \frac{2P_{act}}{\rho A V^3} \tag{9.3}$$

Of course, the power needed for the actuator is a function of the velocity V since a certain momentum coefficient must be reached. In the actuator experiments in (26) the slot dimensions were 280 x 5 mm, which gives a slot area of 0.0014 m^2. In the experiments, a maximum slot velocity of 39.5 m/s was achieved with a loudspeaker developing a power of 80 W. The resulting peak mass flow through the slot is 0.068 kg/s.

The total slot area with three slots activated in these simulations is 0.0009 m^2. Assuming that an amplitude of 15 m/s is used as in the semi-3D runs, the corresponding mass flow is 0.0135 kg/s. This equals 20 % of the mass flow achieved at the Chalmers experiments. If a linear relationship between actuator power and mass flow through the slot is assumed, the power needed to run the actuators in these simulations would be 16 W.

Taking the results from **Table 14**, where a drag reduction of 0.031 was achieved at a freestream velocity of 30 m/s, equation (9.3) gives a net drag reduction of $\Delta C_{D,net} = 0.0245$. 79 % of the drag reduction remains after subtracting the power needed to run the AFC system. A 21 % loss will likely not be a deal-breaker if such reductions can be realized.

9.3 Implementation in vehicles

When implementing an active flow control system in vehicles, one cannot only consider the potential gains of different solutions, but must also take into account factors such as cost, manufacturing and installation in the vehicle. Modern vehicles are packaged very tightly in order to make optimal use of every space. Finding room for a large package of actuators, cavities and slots without affecting internal space and aesthetics is not a trivial task.

Even if a small reduction in drag could pay off cost-wise, if too many other sacrifices must be made to incorporate the system, it will not be commercially viable. Other important factors such as internal and external noise generated by the actuators must also be taken care off. In (26) it was found that the cavity volume does not affect results much, which is good if the cavity is to fit between the inner ceiling and the roof of the car for example. If a system that vibrates the surface of the vehicle itself can provide equally good results this may be preferable, as room for a cavity then must not be created.

10 CONCLUSIONS

In this report, the implementation of an active flow control system based on a zero-net-mass-flux actuator has been studied in OpenFOAM. The task has been two-fold; making it possible to model such a system in the CFD solver, and investigate the effects on the flow field and the aerodynamic behavior. The conclusions from the project are listed below.

10.1 OpenFOAM implementation

- It is possible to simulate an AFC system by setting a time-varying boundary condition (*timeVaryingUniformFixedValue*) for patches designated as slots/holes. One can also directly model a vibrating surface by using a so-called *pointDisplacement* file, although that has not been done here.
- The *codedFixedValue* boundary condition can be used to create a custom OpenFOAM boundary condition – for example one that models a control system by calculating the boundary conditions as a function of previous results.

10.2 CFD modeling

- It is possible to capture the effects of oscillatory forcing of the boundary layer, also with the use of wall functions, reasonably well. Because the first resolved cell lies in the log-layer, the energy from the actuator is inserted some distance away from the wall. This may attenuate the effect of energizing the boundary layer somewhat, as there would likely be a bigger effect when the particles closest to the walls are affected.
- Wall functions do not capture the effect of blowing air parallel to the wall. This energy is “swallowed” by the empirical function that models the behavior between the first grid cell and the wall.
- RANS works well also in 2D in predicting aerodynamic forces. The difference between 2D and semi-3D is negligible for the Windsor geometry.
- Delayed Detached-Eddy Simulation does not seem to produce any unwanted effects of grid-induced separation or similar for this geometry.
- The GAMG-solver is preferred over the standard PCG when the time for solving the pressure field is the dominating part of total computation time. This is increasingly true for bigger meshes.
- Doing extensive parameter studies in full 3D is extremely costly in computation time and is unfeasible without access to supercomputers. This is instead preferably done in wind tunnel experiments.

10.3 Fluid dynamics

- Aerodynamic forces are greatly over predicted using LES-based methods in 2D. So great care must be taken if LES/DES is used in 2D to conclude anything about the magnitudes of the forces.

- In semi-3D, the forces are fairly realistic considering an infinite width of the model.
- The flow field is fairly different in 3D when the middle part of the vehicle starts interacting with the airflow on the sides. The main new feature (at least for a 35° backlight angle) is longitudinal vortices that are rolled up over the C-pillar, which contribute to a substantial part of total drag.
- The drag in 2D and semi-3D is closely related to the strength of the shedding vortices.

10.4 Active flow control

- The main effect of using a ZNMF actuation through rectangular slots, blowing and sucking air perpendicular to the wall, is that the shedding vortices are affected. New frequency content develops at the actuation frequency and its harmonics. It is not trivial to predict if the effect will be increased or decreased total drag for different cases.
- In a 2D simplification it is possible to completely suppress vortex shedding using AFC, which results in a 50 % drag decrease.
- Actuation strategies that work in 2D (such as a continuous slot covering the full width of the car) can result in a significant drag increase in semi-3D. Hence, one should not design an AFC system based on 2D LES/DES information.
- A wider range of actuator frequencies are similarly effective in semi-3D than in 2D where a narrow band of frequencies give much better results than the rest.
- It is the mass flow/momentum coefficient that matters for the effectiveness of the system, not the exit velocity of the jet per se.
- Even though the single tried case in 3D gives a 2 % drag increase, it still shows the potential of the system by noticeably reducing lift and being able to affect the longitudinal vortices. With some tuning of the strategies and the future use of adaptive input signals, it should be possible to create a net benefit for an active flow control implementation in passenger cars and heavy trucks.
- An actuator position closer to the natural point of separation improves the performance of the system.
- Assuming a linear relationship between actuator power and resulting mass flow, less than a quarter of the drag reduction in the best semi-3D case is lost to the actuators. This can probably be improved further by using a more efficient actuator than a standard loudspeaker – for example piezo-based ones.

11 WAY FORWARD

In such a big project as this one, there are still many aspects that need to be investigated further, or which have been completely skipped in this report. The following main areas are a recommendation of future work:

- **Resolved boundary layer** – the DES methodology performs the best when used with a mesh that resolves the full boundary layer down to $y^+ = 1$. Then it would probably be possible to also investigate jet angles parallel to the wall better, which is an important parameter that has not been investigated much here. The accuracy of the results should also increase with a resolved boundary layer, because it can predict the friction better for more situations than the wall functions do.

- **Mesh refinement study** – for especially the semi-3D and 3D simulations, a refinement of the mesh in steps should be undertaken to see some kind of grid convergence. It is an important task to get more confidence in that the CFD model gives accurate results.

- **Extended parameter study** – an investigation of higher frequencies in semi-3D is needed to see if the results continue to improve as the frequency is increased. This information is needed to be able to design a few more 3D cases, which – based on engineering judgment – can maximize the chance of getting good results.

- **Modeling the actuator cavity** – the simplification that the actuator cavity is not modeled at all is a fairly rough one, which needs to be done eventually. When designing the control system, the dynamics of the cavity must be included in the model. A separate LES simulation of only the slot and actuator membrane could be an option to get a very detailed view of the flow field around this area.

- **Design of control algorithm** – an attempt to design an initial control algorithm and figure out optimal ways of implementing it in OpenFOAM is an essential step towards a possible commercialization of the AFC system.

- **Test system on other geometries** – it is interesting to examine the performance of an AFC system in geometries that have different flow features, such as squareback or notchback vehicles. This is important if the system is to be used in heavy trucks for example, where even a few percent drag reduction can give massive total savings.

12 ACKNOWLEDGEMENTS

I would like to extend my gratitude to Creo Dynamics for giving me the opportunity to do my thesis project in a field that is both interesting and on the cutting-edge of technology. It has been fantastic to get to work with the field I love, in a company with the right mentality. I look forward to great years ahead!

My personal thanks go to Gustav Kristiansson, Johan Hammar and Anders Ljung for all the help and good discussions, and to my examiner Assoc. Prof. Gunilla Efraimsson at KTH. Finally, I would like to thank my fellow thesis co-worker David Bergman for all the fun we have had, and especially for the opportunity to beat him in fuβball.

13 BIBLIOGRAPHY

1. *Regulation No 443/2009.* Strasbourg : European Commission, 2009.
2. European Commission Climate Action. [Online] 11 28, 2011. http://ec.europa.eu/clima/policies/transport/vehicles/cars/faq_en.htm.
3. **Michelin Nordic.** 2010.
4. **Wikipedia.** Gasoline. [Online] 11 20, 2011. http://en.wikipedia.org/wiki/Petrol.
5. ACEA - European Automobile Manufacturers' Association. *Passenger cars registrations.* [Online] 01 17, 2012. http://www.acea.be/news/news_detail/passenger_cars_registrations_drop_6.4_in_december_-1.7_in_2011.
6. *Oscillatory Excitation of Unsteady Compressible Flows over Airfoils at Flight Reynolds Numbers.* **Seifert, Avi and Pack, LaTunia G.** Reno : AIAA, 1999. 99-0925.
7. **El-Alti, M., Kjellgren, P. and Davidson, L.** *On the Download Alleviation for the XV-15 Wing by Active Flow Control Using Large-Eddy Simulation.* s.l. : Springer, ERCOFTAC Series, 2010.
8. **Greenblatt, D. and Wygnanski, IJ.** The control of flow separation by periodic excitation. *Prog Aero Sci.* 2000, Vol. 7, 36.
9. *Some salient features of the time-averaged ground vehicle wake.* **Ahmed, S.R., Ramm, R. and Falting, G.** Detroit : SAE technical paper, 1984. 840300.
10. **El-Alti, M., Kjellgren, P. and Davidson, L.** *Drag Reduction for Trucks by Active Flow Control of the Wake Behind the Trailer.* s.l. : Begell House, Inc., 2009.
11. *Drag reduction by closed-loop control of a separated flow over a bluff body with a blunt trailing edge.* **Henning, Lars and King, Rudibert.** Seville : 44th IEEE Conference on Decison and Control, 2005.
12. *Feedback shear layer control for bluff body drag reduction.* **Pastoor, Mark, et al., et al.** 1017, s.l. : Cambridge University Press, 2008, Vol. 10. S0022112008002073.
13. **Wikipedia.** Law of the wall. [Online] 09 08, 2011. http://en.wikipedia.org/wiki/Law_of_the_wall.
14. **Favre, Tristan.** *Aerodynamics simulations of ground vehicles in unsteady crosswind.* Stockholm : KTH School of Engineering Sciences, 2011. ISBN 978-91-7501-196-7.
15. **Wagner, Claus Albrecht, Hüttl, Thomas and Sagaut, Pierre.** *Large-eddy simulation for acoustics.* New York : Cambridge University Press, 2007. ISBN 978-0-521-87144-0.
16. **Rizzi, Arthur.** *Aerodynamic Design - a Computational Approach.* Stockholm : KTH Department of Aeronautical & Vehicle Engineering, 2009.
17. *A One-Equation Turbulence Model for Aerodynamic Flows.* **Spalart, P.R. and Allmaras, S.R.** s.l. : AIAA, 1992. Paper 92-0439.
18. **Eugene, de Villiers.** *The Potential of Large Eddy Simulation for the Modelling of Wall Bounded Flows.* London : Department of Mechanical Engineering, Imperial College of Science, Technology and Medicine, 2006.
19. *Comments on the Feasibility of LES for Wings and on the Hybrid RANS/LES Approach.* **Spalart, P., et al., et al.** s.l. : Proceedings of the First AFOSR International Conference on DNS/LES, 1997.
20. *Detached-Eddy Simulation.* **Spalart, Philippe R.** 41, s.l. : Annual Reviews, 2009. 10.1146.

21. *A new version of detached-eddy simulation, resistant to ambiguous grid densities.* **Spalart, P. R., et al., et al.** 20, s.l. : Theoretical Computational Fluid Dynamics, 2006.
22. **Wikipedia.** OpenFOAM. [Online] 12 19, 2011. http://en.wikipedia.org/wiki/OpenFOAM.
23. **Verhoeven, Olivier.** *Trailing Edge Noise Simulations Using IDDES in OpenFOAM.* Delft : Faculty of Aerospace Engineering, Delft University of Technology, 2011.
24. *Shape features which influence crosswind sensitivity.* **Howell, J.P.** 1993-9, s.l. : The Institution of Mechanical Engineers, 1993.
25. **Kristiansson, Gustav.** *Active Flow Control for Ground Vehicles. EP11195113.3* Linköping, Sweden, 12 22, 2011.
26. **El-Alti, M., et al., et al.** *Experimental Investigation of a Simple Synthetic Jet for Active Flow Control Purposes.* Göteborg : Division of Fluid Dynamics, Chalmers, 2009.
27. **MathWorks.** *MathWorks Nordic.* [Online] 01 20, 2012. http://www.mathworks.se/products/matlab/index.html.
28. **Ansys.** ICEM. [Online] 01 18, 2012. http://www.ansys.com/products/icemcfd.asp.
29. **Efraimsson, Gunilla.** *Personal communication.* 10 2011.
30. **Anderson, John D.** *Computational Fluid Dynamics: The basics with applications.* s.l. : McGraw-Hill, 1995. ISBN 0-07-001685-2.